NORTHWESTERN UNIVERSITY

Growth Behavior and Kinetics of Hydrothermal Crystal Growth in Potassium Tantalate Niobate Particles

A DISSERTATION

SUBMITTED TO THE GRADUATE SCHOOL

IN PARTIAL FULFILLMENT OF THE REQUIREMENTS

for the degree

DOCTOR OF PHILOSOPHY

Field of Materials Science and Engineering

By

Tiffany Ly

EVANSTON, ILLINOIS

September 2021

ABSTRACT

Growth Behavior and Kinetics of Hydrothermal Crystal Growth in Potassium Tantalate Niobate Particles

Tiffany Ly

Nanoparticle synthesis is capable of producing particles with any combination of structure, chemistry, size, shape, and surface. All of the different combinations of these physical properties can produce nanoparticles with almost countless materials properties suited for many applications. Given this interest in using nanoparticles in so many different fields, including electronics, catalysis, and biomedicine, there is also immense interest in understanding the correlation between the physical property of nanoparticles and their resulting functional properties. If any of these properties are phase-, composition-, size-, shape-, or surface-dependent, then methods to synthesis nanoparticles with these traits need to be developed. Therefore, understanding how thermodynamic and kinetic conditions influence nanoparticle growth behavior is essential for these studies. In this dissertation, this was done primarily through studying the growth behavior of oxide nanoparticles in hydrothermal syntheses.

A kinetic regime model was proposed based upon the observation of two different growth morphologies on hydrothermally synthesized $KTaO_3$ nanoparticles. Secondary electron imaging demonstrated that there were two dominant growth mechanisms: terrace nucleation, where surfaces are rough, and terrace growth, where surfaces are smooth. In the proposed model based upon standard step-flow growth, the rates of both mechanisms were established to be dependent on the chemical potential, or driving force, of the synthesis environment—terrace nucleation dominates under a higher driving force, and terrace growth dominates with a smaller driving force. This analysis illustrated the mechanism behind the formation of irregular rough particles as well as a method to achieve smooth well-faceted particles by enhancing the smoothing regime with terrace growth.

The composition and chemical behavior of nanoparticle surfaces have significant effects on their growth behavior as well. Hydrothermally grown $KNbO_3$, $KTaO_3$, and $KTa_{1-x}Nb_xO_3$ particles were studied to examine the complex relationship between surface composition, phase, chemistry, and energetics. These may all be used as parameters to model the rates nanoparticle growth mechanisms and identify what conditions favor certain growth regimes. Two different composition-dependent growth modes were identified, where one type formed smooth surface facets, while the other resulted in roughened surfaces. Electron microscopy characterization, density functional theory calculations, and mathematical growth models were used to illuminate the role of surface properties and chemisorption on nanoparticle morphology. Surface energy reduction by chemisorption can increase the rate of terrace nucleation, driving the roughening of the lower surface energy nanoparticle surfaces.

Properties of the synthesis environment can have considerable influence on the properties of the products grown. Potassium fluoride was added to the hydrothermal syntheses of $KTa_{1-x}Nb_xO_3$ and $KTaO_3$ to investigate the effects of an additional mineralizer. One result demonstrated that potassium fluoride increased the solution stability of the tantalum precursor and therefore decreased its reaction rate, resulting in a change in the composition heterogeneity of tantalum, and niobium in the solid solution particles. When added in sufficient quantities to the solution, potassium fluoride also promoted the formation of particles with defect enhanced kinetic Wulff shapes in contrast to the typical nanocuboids produced. The increase in chemical potential of the solution because of fluoride enabled the formation of planar defects in the bulk, which accelerated growth in-plane to form particles with characteristic flat rectangular flake geometries. Thermodynamic modeling with density functional theory calculations suggested that potassium fluoride caused the formation of a defect phase $K_{n+1}Ta_nO_{3n}F$.

A two-step heat sequence in a hydro-sauna environment was used to grow well-faceted $LnScO_3$ particles. The dominant growth mechanisms and primary phases produced under different processing temperatures were identified to optimize the heating sequence temperatures. First, a high temperature was used to provide the appropriate thermodynamic conditions to nucleate the perovskite phase and increase size monodispersity. The second step lowers the temperature to enter the smoothing regime, where terrace growth encourages the formation of smooth, flat facets on the particle surfaces. The successful synthesis of $LnScO_3$ particles with improved size and shape control was a demonstration of how crystal growth concepts can be used to design nanoparticle synthesis methods.

Acknowledgements

First, I would like to thank my advisor, Professor Laurie Marks, for his guidance and support over the course of my Ph.D. I will always appreciate his curiosity and the level of scientific rigor with which he encourages all of his students to approach their research. With his mentorship, I gained the freedom to explore several different problems and acquire whatever skills were necessary for the question at hand. Thank you for your patience with my questions and your encouragement through all of the silly and hard problems I encountered. Whenever I am lost in the future, I will remember to "follow the science, not the electrons."

Next, I want to thank Professor Ken Poeppelmeier for his kindness and generosity in allowing me to use his laboratory to perform all of my synthesis experiments and for serving on my dissertation committee. His expertise and intellectual input on my research has been invaluable throughout the years, and our conversations are always enjoyable. I would also like to thank the other members of my thesis committee: Professor Peter Voorhees and Professor Jian-Min Zuo. I am also grateful to Professor Michael Bedzyk for serving on my qualifying exam committee.

The work presented in this dissertation would not have been possible without the contributions of my collaborators, and I am very grateful for their help over the years. Thank you, Ryan, for our seemingly countless number of conversations about nanoparticle growth and for working with me to develop the lanthanide scandate synthesis method, as

well as for your experimental assistance with TGA-GC-MS of some of my samples. Thanks to Zach for also working with us to acquire TEM images on the scandates projects. I am especially grateful to J.G. Wen at Argonne National Laboratory for training me on and his assistance with operating the ACAT to obtain beautiful TEM images. Thanks to Ahmet for helping me obtain some EDS line scans on my KTO samples early on in my career. Thank you, Chris, for performing X-ray photoelectron spectroscopy on my samples as well.

Thank you to all of the facility managers for all of their help, especially Jinsong Wu and Jerry Carsello. I would also like the opportunity to acknowledge my funding. The work presented in this thesis was supported by the National Science Foundation (NSF) under grant number DMR-1507101. Use of the Center for Nanoscale Materials and the Office of Science user facility was supported by the U.S. Department of Energy, Office of Science, Office of Basic Energy Sciences, under Contract no. DE-AC02-06CH11357. I also received financial support from the Ryan Fellowship.

I am endlessly grateful to all of the past and present members of the LDM group for their company over the years. Thank you, Chris, for being my lab partner at Cornell during our undergraduate studies almost a decade ago and for being a wonderful groupmate during our Ph.D. Special thanks to Pratik for teaching me electron microscopy and for getting me started with density functional theory. Thanks to Ryan for all of our conversations and keeping me company in the Poeppelmeier lab and office. To both Lawrence and Zach: thank you for the long drives and great company en route to ANL. Thanks to Betty for her sage knowledge about nanoparticle shapes, thermodynamics, and kinetics. Thanks to Tassie for picking me up during visit weekend as a prospective student, and

for helping me with my job search as I approached graduation. For their camaraderie, commiseration, and too much all-you-can-eat sushi, all the thanks to Alex, Say, Emily H., Emily G., Lizzie, Evan, Karl, Ahmet, Xiao-Xiang, Bruce, and Hans. I would also like to thank the Poeppelmeier group for their advice and company whenever I worked in their lab. I wish all of the current students the best of luck in their studies.

I would have been unable to complete this journey without all of the support from my friends. During the tough times of the past year, I am especially grateful to Chris, Rohit, Shane, Michaela, Max D., Max W., and Shreya for their company during our weekly video chats. Thanks to my other Northwestern classmates for their company over the years. Thank you, Melissa and Claire, for our triumvirate of commiseration in pursuit of our doctorate degrees and the decades of friendship.

Lastly, I need to thank my family. There are no words for how thankful I am to my parents for providing me with this life and opportunity and for their support in my pursuit of more years of education than both of them have experienced combined. Their lifetimes of hard work and dedication served as motivation and inspiration to succeed. To my brother Kevin for braving all of the challenges of being the older sibling in an immigrant family before me and for sparking my curiosity for science: thank you so much. This would not have been possible without you all.

List of Abbreviations

A_R: Annihilation rate

E_{H_2O}: Energy of water molecule

E_{ads}: Adsorption energy

E_{bulk}: Energy of bulk unit cell

E_{dry}: Energy of surface slab without adsorbed water

E_{slab}: Energy of surface slab

E_{surf}: Surface energy

E_{wet}: Energy of surface slab with adsorbed water

G_R: Growth rate

K_{max}: Magnitude of k-vector

N_R: Terrace nucleation rate

R: Gas constant

R_{mt}: Atomic muffin-tin radius

$R_{mt}K_{max}$: Product of smallest R_{mt} and magnitude of largest k-vector

T: Temperature

ΔE: Nucleation energy

ΔG_{KF}: Gibbs free energy of KF

ΔG_{KTO}: Gibbs free energy of $KTaO_3$

$\Delta G_{\mathrm{K_{n+1}Ta_nO_{3n}F}}$: Gibbs free energy of $K_{n+1}Ta_nO_{3n}F$

$\Delta G_{\text{reaction}}$**:** Gibbs free energy change of reaction

ΔG_{total}**:** Total free energy change

$\Delta\mu$**:** Chemical potential difference

$\Delta\mu_{\text{critical}}$**:** Critical chemical potential difference

$\Delta\mu_{\text{KF}}$**:** Chemical potential of KF in solution

$\gamma(m)$**:** Mean ionic activity

m**:** Molality

n_{H_2O}**:** Number of water molecules

n_{bulk}**:** Number of bulk unit cells

ACAT: Argonne chromatic aberration-corrected TEM

ADF: Annular dark field

BF: Bright field

DF: Dark field

DFT: Density functional theory

DP: Diffraction pattern

EDS: Energy dispersive X-ray spectroscopy

FFT: Fast fourier transform

GGA: Generalized gradient approximation

HAADF: High angle annular dark field

HRTEM: High resolution transmission electron microscopy

$K_{n+1}Ta_nO_{3n}F$: Ruddlesden-Popper-like phase

KNO: Potassium niobate ($KNbO_3$)

KTN: Potassium tantalate niobate ($KTa_{1-x}Nb_xO_3$)

KTO: Potassium tantalate ($KTaO_3$)

$Nb_6O_{19}^{8-}$: Lindqvist ion

NP: Nanoparticle

RP: Ruddlesden-Popper

SE: Secondary electron

SEM: Scanning electron microscopy

STEM: Scanning transmission electron microscopy

TEM: Transmission electron microscopy

TGA-GC-MS: Thermogravimetric analysis coupled with gas chromatography-mass spectrometry

XPS: X-ray photoelectron spectroscopy

XRD: X-ray diffraction

Table of Contents

List of Tables

List of Figures

CHAPTER 1

Introduction

1.1. Motivation

Every year thousands of scientific articles are published on the topic of nanoparticles (NPs). Compared to bulk materials, the characteristic length scale of NPs, typically 1–100 nm, gives them unique properties that make them well-suited for a diverse range of optical, electronic, catalytic, and biomedical applications. [**14**, **28**, **29**] A large portion of the attention on NPs has been focused on metal oxides in particular because the variety of crystal structures and compositions available for selecting and tuning certain functional material properties. [**30**–**32**] Beyond crystallography and chemistry, other physical characteristics of NPs, including their size, shape, and surface properties, are also largely responsible for dictating their material properties. If the size, shape, and surface can be selected through synthetic methods, then the study of size, shape, or surface-dependent NP properties can be simplified and accelerated. However, NP synthesis is complex, and minor changes in the components or thermodynamic conditions of a synthesis system can drastically influence the growth behavior of the NPs produced. The goal of this dissertation is to understand some of these relationships between synthesis environment and growth mechanisms.

Nanoparticles take on different categories of shapes depending on the synthesis environment. In a system at thermodynamic equilibrium, the particles will take on the lowest

energy shape, which has been calculated as the thermodynamic Wulff construction. [**33**] When a system deviates from thermodynamic equilibrium, a wide-range of kinetic shapes can take form. This is especially the case in solution-based systems, such as the hydrothermal method primarily studied in this thesis, which depend on supersaturation of the solution to precipitate nuclei to grow. In some instances, the kinetic Wulff shape of a grown particle may resemble its thermodynamic Wulff shape, but these occurrences are only coincidental and do not indicate that equilibrium conditions were met. Kinetic shapes are determined by the rates of growth of different crystallographic surfaces and by the rates of growth of different growth processes. While thermodynamic quantities such as surface energies can be used to calculate the equilibrium shapes of particles, growth velocities are more variable, making it a challenge to predict kinetic shapes. In order to understand growth velocities and other important kinetic processes during crystal growth, models that provide insight into molecular, chemical, and physical processes that manifest into different crystal growth processes and modes need to be developed. The development of these models requires the effects of different aspects in a synthesis system need to be analyzed.

In this work, these regions are divided into four regions as shown in Figure 1.1. Region I is the aqueous solution, which contains all of the precursors, solvents, and other components of the synthesis. Region II encompasses the interaction region between the solution and surface, where interactions such as adsorption or chemisorption can occur. Growth processes such as terrace nucleation and terrace growth are contained in Region III at the crystal surface. Region IV is the bulk, which is where composition, structure,

and microstructure is taken into account. The effects of each region will be addressed throughout this dissertation.

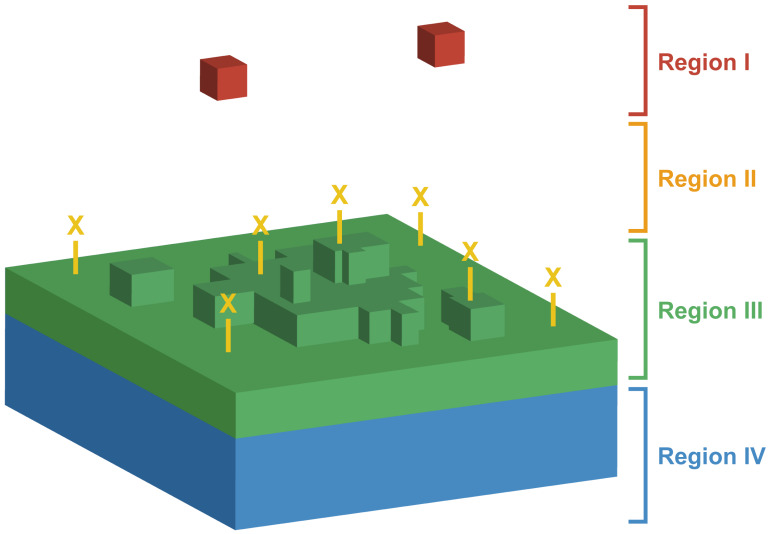

Figure 1.1. Schematic of four key regions in a solution-based nanoparticle synthesis system. Region I is the solution; Region II is the near surface, where adsorption can happen; Region III is the surface where terraces nucleate and grow; Region IV is the bulk. [**3**]

1.2. Organization

This dissertation aims to unite crystal growth theory with experimental NP growth behavior. This is done by first presenting important background information about crystal growth theory, thermodynamic and kinetic growth conditions, and growth processes, including terrace nucleation and terrace growth in Chapter 2. Chapter 2 additionally includes information about all of the techniques used to synthesize, characterize, and calculate properties of the materials studied in this work. In Chapter 3, the consequences of the competition between the rates of terrace nucleation and terrace growth are explored through a time-resolved study of the hydrothermal synthesis of $KTaO_3$ NPs. More

significantly, the terracing and smoothing regimes are defined based upon the physical characteristics NPs adopt when grown under each regime, and these regimes are linked to certain thermodynamic quantities and kinetic conditions of the synthesis environment. The model was expanded to include the effects of surface energy in Chapter 3, where the material system was also expanded to include $KNbO_3$ and the solid solution $KTa_{1-x}Nb_xO_3$. The surface composition, chemistry, and behavior were studied and linked through observations and calculations on tantalum-rich and niobium-rich surfaces of the three materials, and the energetic effect of chemisorption was identified as a consequential factor in controlling the growth morphology of the materials. Chapter 5 introduces a new mineralizer, potassium fluoride, to the synthesis to these materials to great effect. The new mineralizer was able to change the precursor reaction kinetics when added at low concentrations, and it was able to introduce shape-altering planar defects when added at high concentrations. The structure and formation criteria of these defects were studied with density functional theory calculations. After establishing relationships between growth environment and behavior through those three case studies, the concepts understood about growth regime kinetics are applied to a new material and synthesis method in Chapter 6, where well-faceted $LnScO_3$ NPs were grown by using a two-step hydro-sauna heat treatment to optimize the terracing and smoothing regimes during synthesis. With the broader goal in mind to connect crystal growth theory with experiment, Chapter 7 reviews the products of hydrothermal synthesis in literature in the context of broader categories of thermodynamic and kinetic growth modes, including thermodynamic growth, step-flow growth, roughened growth, and diffusion-controlled growth. Finally, several paths of future directions for this work are outlined and discussed in Chapter 8.

CHAPTER 2

Background and Methods

2.1. Background

A major challenge in any NP synthesis is predicting or controlling the shapes of the particles produced. The shapes are largely dictated by the growth condition, and it can be another challenge to distinguish between thermodynamic and different types of kinetic control over growth. Fortunately, crystal growth theory can be used as a foundation for understanding how nanoparticles may grow under certain conditions, or alternatively used to identify which growth behaviors are dominant in a certain reaction. In this section, we provide some relevant background about particle shapes and growth processes that may be encountered in this thesis.

2.1.1. Kinetic Wulff Shape

The thermodynamic Wulff construction is a very useful tool for understanding crystal shapes, but it is only applicable to certain conditions, ie. thermodynamic equilibrium for free-standing, single crystalline particles. [**33**] Nanoparticle synthesis conditions typically deviate from these assumptions, which is why the kinetic Wulff construction and the kinetics of growth processes are the focus of this thesis. Nanoparticles are usually synthesized in a supersaturated system that deviates from thermodynamic equilibrium. In a solution-based system, which is the focus of most of this work, this supersaturation

is defined as:

$$\Delta\mu = \mu_{sat} - \mu_{eq} \tag{2.1}$$

where $\Delta\mu$ is the chemical potential difference between the chemical potential of the supersaturated solution (μ_{sat}) and the chemical potential of the equilibrium solution (μ_{eq}). This supersaturation is responsible as the chemical potential driving force behind the nucleation and growth processes discussed throughout this thesis. We will describe many alternative ways it can be defined for specific material synthesis systems.

The kinetic Wulff shape is the broad category of crystal shapes that form under kinetically-controlled growth conditions. It is mathematically constructed by taking the envelope of the slowest growing facets:

$$S = x : x \cdot \hat{n} \leq \lambda(t)v(\hat{n}) \tag{2.2}$$

where v is the growth velocity dependent on time t for each facet defined by $\hat{n}$. This is analogous to the thermodynamic Wulff construction, except growth velocities are used instead of surface energies. [**33**] The term kinetic Wulff shape is usually only reserved for crystals with smooth, well-defined facets and polyhedron shapes. Under many circumstances of NP synthesis, the products that are produced are irregularly shaped or possess rough surface morphologies. A goal of this dissertation is to understand the driving forces and kinetics behind this type of behavior, and how they can be controlled. This begins by considering how crystals grow on a surface level by examining growth terraces.

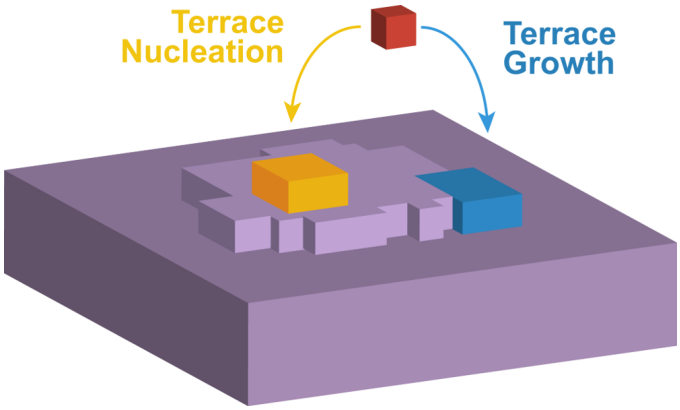

Figure 2.1. Schematic illustrating the terrace nucleation (yellow) and growth processes (blue). The purple block represents the surface of a growing crystal with an existing growth terrace. The red block is a precursor species in solution that will participate in either nucleating a new terrace atop the existing one, or it will deposit onto the surface and contribute to the growth of an existing terrace.

2.1.2. Step-Flow Growth Processes

A schematic of the terrace nucleation and growth processes is provided in Figure 2.1. Terrace nucleation is the process where the reaction results in the formation of a new growth terrace atop an existing surface of a crystal, and terrace growth happens when the reaction adds to an existing terrace across a surface. A growth terrace can be modeled as a 3D hemisphere to describe the rate of formation mathematically. For a 3D hemisphere terrace nucleating on a crystal surface, the total work or free energy change for nucleation can be defined as:

$$\Delta E = \frac{2}{3}\pi R^3 \Delta\mu + 2\pi R^2 \gamma \tag{2.3}$$

where R is the radius of the terrace nucleus, $\Delta\mu$ is the chemical potential change of forming the nucleated material, and γ is the surface energy. There is a critical radius (R^*) for terraces nucleated at the surfaces of particles. The critical nucleation energy at

this radius can be evaluated as:

$$\Delta E(R = R^*) = \frac{8\pi\gamma^3}{3\Delta\mu^2} \tag{2.4}$$

The terrace nucleation rate can be written as an Arrhenius function:

$$N_R = f_0 \exp \frac{\Delta E}{k_B T} \tag{2.5}$$

where f_0 is a pre-exponential factor that is dependent on the diffusion of molecules and solutes in solution and other factors.

In contrast to terrace nucleation, terrace growth is not dependent on a nucleation type process, and therefore its rate does not have a statistical thermodynamic exponential dependence. However, terrace growth is still driven by the supersaturation, or chemical potential, of the solution environment. Terrace growth occurs when species diffuse to an existing growth terrace on a crystal surface and reacts, thereby contributing to the lateral growth of the terrace across the facet. The rate of terrace growth (G_R) can be defined as:

$$G_R = C\Delta\mu \tag{2.6}$$

where C is a coefficient that includes diffusivity and other environmental terms.

2.2. Methods

2.2.1. Hydrothermal Synthesis

Among the many nanoparticle synthesis methods, hydrothermal synthesis is a popular solution-based method for many reasons. The term hydrothermal synthesis traditionally

refers to a reaction that occurs in water ("hydro") in a sealed vessel or autoclave at a temperature greater than the boiling point of water ("thermal"). It is often chosen for its many practical advantages over other synthesis methods, including the capability of producing highly crystalline products in relatively mild conditions (∼100-300 °C) with decent control over the size and shape of the nanoparticles in a single step. Because size and/or shape dependent properties can significantly affect the functional properties of nanoparticles, synthesis methods with reasonable size and shape control are attractive choices in nanoparticle research regarding applications for nanoparticles, such as biomedical applications, catalysis, or energy technologies. [**14**, **28**–**30**] Therefore, hydrothermal synthesis has been successfully used to produce a wide range of materials, including many different simple and complex oxides, semiconductors, and other classes of materials in a variety of shapes and sizes. [**31**, **32**, **34**]

A typical hydrothermal synthesis "recipe" is composed of three main parts: water, reactants, and mineralizer(s). Water acts as both a solvent and transportation medium in the reaction. As a solvent, water hydrates or complexes precursors to form more reactive compounds for the chemical reaction. Mineralizers aid in the dissolution of precursors, and the choice of mineralizer, often basic or acidic compounds that alter the pH of the solution, can significantly impact the phase, size, and morphology of the nanoparticles produced. Pourbaix diagrams, or Eh-pH diagrams, which map the thermodynamic equilibrium phases relative to its redox potential and pH are useful guides for choosing the type and quantities of mineralizers used in a synthesis. [**10**, **35**, **36**] When these components are heated in a sealed autoclave, the system reaches an autogenous pressure, which

is the pressure reached without an externally applied force and is dependent on the composition of the reactants, filling factor, and temperature. High pressures can effect the density, dielectric properties, and solvent properties of water in the hydrothermal system. However, for most of the syntheses used in this work, the fill factors are low enough such that the pressure changes and effects are relatively minimal in comparison to those of temperature. More information about the relationships between temperature, pressure, and fill factors can be found in references. [**35**, **37**]

The hydrothermal syntheses used in this work to produce $KTa_{1-x}Nb_xO_3$ (x = 0–1) nanoparticles were modified from syntheses developed by Goh et al. [**38**,**39**] and Kumada. [**40**] In these syntheses, solid Ta_2O_5 and/or Nb_2O_5 were added to 15 M KOH and heated to 150–200 °C in an autoclave. KOH acts as both the mineralizer and reactant in the reaction, and therefore its concentration is an important parameter in the thermodynamic factors and kinetics of nanoparticle growth. Specific precursor quantities and heating times are detailed in later sections. In all cases, the temperature of the oven was ramped to the target temperature as quickly as possible without a specified heating rate. After hydrothermal treatment, the product was washed several times with deionized water until the supernatant liquid was measured as neutral using pH strips. Then, the product was dried overnight in an oven set at 80 °C.

Some additional modifications of the syntheses were also performed in order to study the effects of different concentrations and mineralizers on the properties of the products. If there were additional compounds added to the solution, the solids and KOH solution were stirred for at least 30 min to ensure uniform mixing.

2.2.2. Electron Microscopy

Electron microscopy was the primary analytical tool used to study the nanoparticles synthesized in this work. It is a powerful characterization tool for studying the crystallography, morphology, chemistry, and other properties of materials. The small wavelength of high energy electrons (∼80–300 keV) enables high resolution imaging to study even the atomic structure of materials. As shown in Figure 2.2, many different signals can also be generated by and collected from the interaction of an electron beam with sample material. Electron microscopes are categorized into two different electron beam illumination modes that can generate and collect these signals: parallel beam and convergent beam. The first describes transmission electron microscopy (TEM), where a parallel beam of electrons is transmitted through a sample. The second is scanning transmission electron microscopy (STEM), where a converged beam of electrons forms a probe that rasters across a sample instead. Both types were utilized to characterize different properties of the oxide nanoparticles. Because electron microscopy encompasses so many different techniques, a brief overview of the particularly relevant techniques will be discussed here.

In TEM, when high energy electrons interact with a sample material, they are transmitted or scattered in different ways depending on the energy of the electrons and properties of the material. The transmitted electrons form a projected image of the sample that can be used to characterize the sample. An objective aperture can be inserted at the back focal plane to select between the direct or diffracted electron beams to produce bright field (BF) and dark field (DF) images, respectively. In addition to an image, the scattered electrons form a diffraction pattern (DP) at or near the back focal plane of the

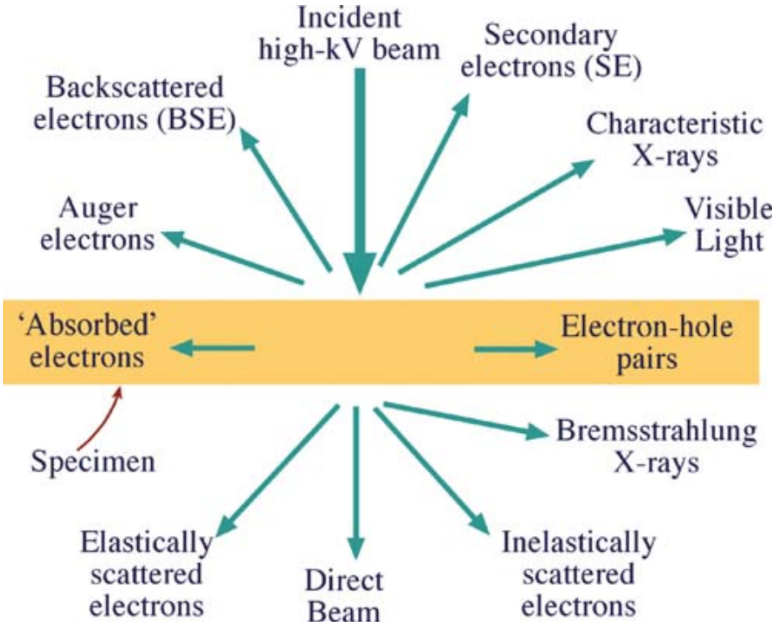

Figure 2.2. Signals generated from the interaction of high energy electrons and a sample. The arrows show only general directions of strongest detection for each type of signal. Schematic adapted from [**4**].

objective lens. TEM BF/DF imaging and electron diffraction characterization of materials can yield crystallographic information about the sample, especially when used in combination, such as its crystallinity, crystallite orientation(s), and microstructure.

When multiple electron beams are used to form an image (e.g. when no objective aperture is used), the interference between phase differences of the electron beams causes phase contrast in the image. Although phase contrast is often present during TEM imaging, it is the dominant form of contrast present in and most commonly associated with high resolution transmission electron microscopy (HRTEM) images. HRTEM is a very effective method for characterizing the atomic structures of materials. Furthermore, using HRTEM to analyze the atomic surface structures of nanoparticles through "profile imaging" has been a successful method for determining the surface terminations of many

different nanoparticle materials. [**41**–**45**] Although high resolution imaging is one of electron microscopy's major advantages and the development of aberration correctors have significantly improved the spatial resolution of modern TEMs, interpreting phase contrast in HRTEM images is not trivial. A TEM has many sources of different aberrations, such as spherical aberration caused by imperfect lenses and chromatic aberration caused by energy spread of the electron beam, that can be treated as a reciprocal space phase shift of electron waves. This phase shift term affects the contrast transfer in the image plane of a microscope. HRTEM image simulation methods, such as multislice simulation (Section 2.2.3) have been developed to aid in the accurate interpretation of contrast and information in HRTEM images.

In contrast to a TEM, a STEM forms a digital image pixel-by-pixel by rastering a probe back-and-forth across an area of the sample. The transmitted electrons can be collected simultaneously by different detectors in the microscope. A variety of detectors can be used in a STEM for imaging, including secondary electron (SE), annular dark field (ADF), and on-axis bright field detectors. SE imaging was the primary imaging technique used for studying the nanoparticles synthesized in this work. Although secondary electron microscopy is more commonly associated with scanning electron microscopes, it can also be performed in a STEM with the advantage of higher resolution granted by the higher operating voltages of a typical STEM. Secondary electrons are generated when the high energy electron beam ejects electrons from the conduction or valence bands of a material. The ejected electrons have small mean escape paths ($\lambda \approx 1$ nm) because of their low energies (≤ 50 eV), hence SE imaging is a surface sensitive technique well-suited for characterizing the surface topography and morphology of a sample. BF imaging in a

STEM is similar to BF imaging in a TEM: an on-axis detector is used to capture the signal from the direct beam of transmitted electrons similar to how the objective aperture is used to select instead of using an aperture to select the direct electrons. In contrast, ADF imaging is rather different than TEM DF imaging because the annulus shaped detector detects electrons scattered in multiple directions and angles. The collection angle can be varied to enhance different types of contrast. For example, heavy elements cause electrons to scatter at higher angles via Rutherford scattering, so using a high angle annular dark field (HAADF) detector maximizes Z-contrast over diffraction contrast in the resulting image.

In addition to imaging and diffraction techniques, analytical electron microscopy techniques were also performed to characterize the composition of nanoparticles. Energy dispersive X-ray spectroscopy (EDS) uses the characteristic X-rays generated during electron microscopy to identify the elements present in a sample. Characteristic X-rays are produced as a result of the interaction between high energy beam electrons and atoms in the sample material. A transfer of energy from a high energy electron to a core shell electron causes the core electron to be excited and ejected from the inner shell, leaving a hole. When this hole is filled by an electron from the outer shell of the atom, the excited atom is returned to the ground state. This process is accompanied with the emission of a corresponding characteristic X-ray or Auger electron. Characteristic X-rays correspond to the energy difference between the location where the hole is filled and the outer shell from where the electron came. In a STEM, the collection of these characteristic X-rays can be spatially resolved to form EDS maps of the sample.

Microscopes at both Northwestern University and Argonne National Laboratory were used to conduct electron microscopy experiments. SE imaging and EDS were primarily performed on the Hitachi HD-2300 STEM. HRTEM was performed on the Argonne chromatic aberration-corrected TEM (ACAT), an FEI Titan with a CEOS C_c/C_s image corrector. The FEI Talos F200X TEM/STEM was used for additional TEM BF and DF imaging, as well as electron diffraction. All microscopes were operated at 200 kV. TEM samples were prepared by either drop casting powder suspended in a solvent (e.g. ethanol or isopropyl alcochol) onto a TEM grid or dipping a grid into the dry powder.

2.2.2.1. Extracting length measurements from TEM images. In order to more accurately measure their sizes and quantify the surface area for statistical distributions presented in later chapters, a method of obtaining 3-dimensional information from 2-dimensional images was needed. The majority of the particles synthesized in this thesis were shaped as nanocuboids, which provides a convenient set of orthogonal axes to use in this calculations. Figure 2.3 shows a schematic of the measurements taken on a nanocuboid (grey cube). In order of construction: the black lines (L_{black}) represent the edge lengths of the nanocuboid; the red lines (L_{red}) are drawn along the orthogonal axes of the cuboid; the yellow lines are drawn as a triangle where each corner meets the end of a red line; the purple semicircles are drawn across the yellow lines; the green lines are drawn from the center of the red axes and perpendicular to the yellow lines; the blue lines (L_{blue}) connect the intersections of the red-yellow lines and green-purple lines. The ratio between the blue line and the red line adjacent to it are used to calculate the 3D length

(L) of the black line from the 2D projection:

$$L = L_{black}\frac{L_{blue}}{L_{red}} \tag{2.7}$$

This geometric construction uses the relationships between a series of right triangles to determine a 3D length scale from a 2D image of a projection.

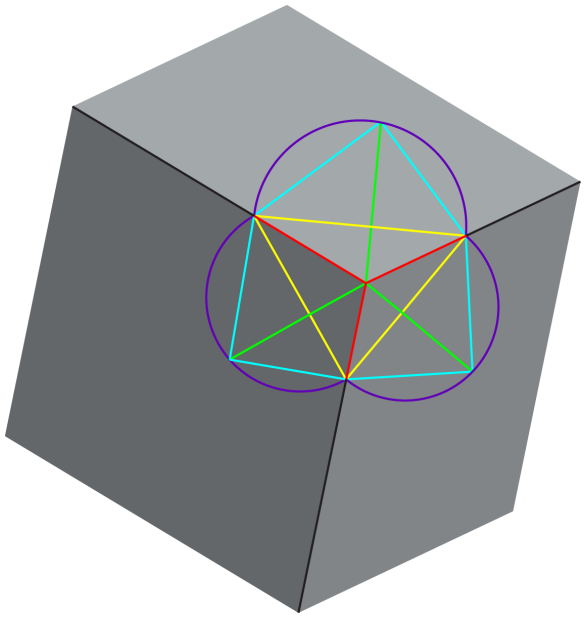

Figure 2.3. Schematic of geometric construction used to calculate 3D lengths from 2D projections of nanocuboids in images.

2.2.3. Multislice Simulation

HRTEM image simulation methods were developed in order to address the problem of accurately determining crystal structure information from experimental images. Because experimental HRTEM images are 2D intensity maps of a sample, they do not contain phase information that is necessary for 3D structure solution. Moreover, sample properties and aberrations in the microscope affect the intensity and phase of electron waves that form

images, contributing to the complexity of interpreting phase contrast HRTEM images. Two of the most commonly used image simulation approaches are the multislice and Bloch wave methods. The multislice method described by Cowley and Moodie was employed in this work to study nanoparticle surfaces and microstructure. [**46**]

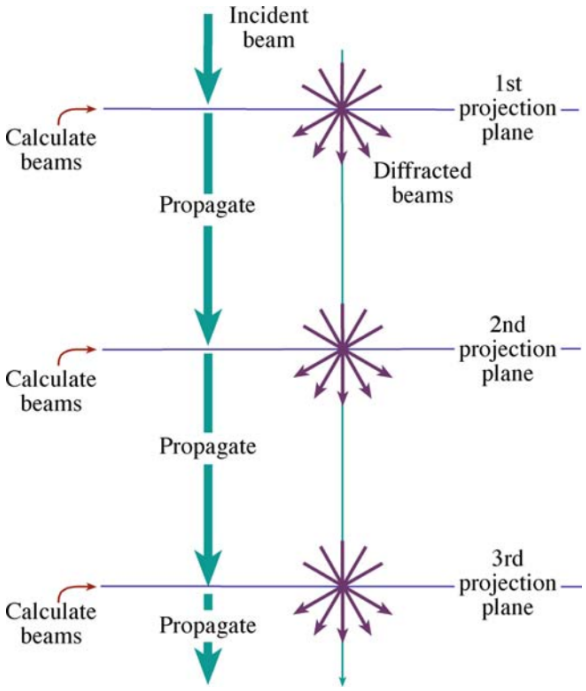

Figure 2.4. Diagram of the multislice method process. At each slice, the phase grating is applied to calculate the amplitudes and phases of the electrons. Then, the beams are propagated through vacuum to the next slice to repeat the process. Image adapted from [**4**].

The multislice method was derived as a way of solving the Schrödinger wave equation for electrons traveling through a solid, enabling the calculation of analytical expressions for the amplitudes of diffracted beams and consideration of dynamical diffraction effects. It applies the phase grating approximation, which assumes the crystal affects only the phase of the electron wave traveling through it and not the amplitude. Therefore, in the multislice algorithm, a crystal can be modeled as a sequence of x-y diffraction planes, or

slices, separated by vacuum with incident electron waves from the z-direction. At each slice, the amplitude and phases of electron beams generated by an incident beam are calculated using the phase grating solution, then these beams are propagated to the next slice. The propagation function accounts for the lateral spread of electron waves across the x-y plane between each slice. An advantage of the multislice method is that computationally fast Fourier transforms can be used in place of computationally expensive convolutions. The iterative multislice method is summarized by the schematic in Figure 2.4.

The MacTempasX software package developed by Roar Kilaas was used to perform all simulations in this work. [**47**] For structure solution, a crystal structure is assumed and simulated for the experimental conditions, such as sample thickness, defocus, and microscope operating parameters. In most of the image simulations shown in this dissertation, the parameters were set as follows: the voltage was 200 kV; Cs was 0.008 mm; convergence angle was 0.60 mrad; defocus spread was 60 Å; astigmatism was at least 20 Å; mechanical vibration was at least 0.5 Å. The relative match, or goodness-of-fit, between the simulated image and experimental image are compared. If the simulated image does not match, simulation parameters or the guess structure are changed, and the process is repeated.

2.2.4. X-Ray Diffraction

Powder X-ray diffraction (XRD) was used to characterize the crystal structures of the nanoparticles studied. During XRD, X-rays are scattered by the crystalline lattice of a material. The locations of the peaks will depend on the angle of incidence, angle of the detector, wavelength of the X-rays, and structural properties of the material. The

relationship between these variables is summarized by Braggs' law:

$$2d_{hkl}\sin\theta = n\lambda \tag{2.8}$$

where d_{hkl} is the interplanar spacing between (hkl) planes, θ is the angle of incidence relative to the sample for maximum constructive interference, n is a positive integer, and λ is the wavelength of the X-rays. During a powder XRD acquisition, the angle θ is varied by the simultaneous movement of both the X-ray source and detector. The angles where maximum intensity, or diffraction peaks, are observed in the DP correspond to specific d_{hkl} of specific phases. Using this method, a DP can be fingerprinted to identify the phases present in a sample. In addition to fingerprinting the phases of material present in a sample, powder XRD patterns can also be refined to determine information such as unit cell dimensions, phase fractions, and crystallite size and shape via Rietveld refinement.

XRD was performed using several different instruments, all equipped with Cu K_α X-ray sources. These include a Rigaku DMAX diffractometer operated at 40 kV and 20 mA, Rigaku Ultima diffractometer operated at 40 kV and 44 mA, and Smartlab 3 kW Gen2 operated at 40 kV and 44 mA. Diffraction patterns were matched to phases using the MDI JADE data analysis program. [**48**] Rietveld refinement was performed with GSAS-II. [**49**]

2.2.5. Density Functional Theory

Density functional theory (DFT) calculations were used to calculate the formation and surface energies of many different materials in this work. It is a quantum mechanical model that uses the Hohenberg-Kohn theorems and Kohn-Sham equations to determine the behavior of electrons in a solid. However, solid materials are composed of many

electrons that influence the behavior of each other, and the impracticality of solving so many equations manifests as the many-body problem for a solid crystal. The foundations of DFT were developed by Hohenberg, Kohn, and Sham as a method of approaching the many-electron problem. [**50**, **51**] They theorized that electron density can be used as the fundamental variable instead of the electron wave functions to calculate material properties, and that the electron density that minimizes the total energy of a system defines its ground state.

One of the Hohenberg-Kohn theorems relating the total energy of an interacting inhomogeneous electron gas (E) in the presence of an external potential (V_{ext}) to a functional of the electron density (ρ) can be represented mathematically as:

$$E = \int V_{ext}(\vec{r})\rho(\vec{r})d\vec{r} + F[\rho] \tag{2.9}$$

where $F[\rho]$ is a universal functional of the density. The Kohn-Sham equations reduce the many-body problem into many single-body problems. The total energy of a system can be calculated then as:

$$E = T_o[\rho] + \int V_{ext}\rho(\vec{r})d\vec{r} + \frac{1}{2}\int \frac{\rho(\vec{r})\rho(\vec{r'})}{|\vec{r'} - \vec{r}|}d\vec{r}d\vec{r'} + E_{xc}[\rho] \tag{2.10}$$

where T_o is the non-interacting kinetic energy and E_{ext} is the exchange-correlation energy. The exact exchange-correlation functional cannot be calculated exactly, so many different approximations have been developed for DFT. The generalized gradient approximation (GGA) is one of them and considers the electron density and its gradient. One of the most popular forms of the GGA used in DFT is the Perdew-Burke-Ernzerhof (PBE) functional. [**52**, **53**] All of the calculations performed in this work used the PBEsol functional, which

is a revised version of the PBE functional for solids and surfaces. [**54**] The improvements of this functional for calculating the equilibrium properties of solids and their surface energies is why it was selected for this body of work.

All of the DFT calculations in this work were done using the WIEN2k package, an all-electron augmented plane wave plus local orbitals code. [**55**, **56**] In this approach, a unit cell is partitioned into two types of regions: atomic spheres, which are defined by specified muffin-tin radii, and interstitial regions. The regions inside the muffin-tin radii are defined by local orbitals, or linear combinations of radial functions times spherical harmonics. The interstitial regions are defined using a plane wave expansion. The accuracy of the calculations performed using the WIEN2k code are defined by the parameter $R_{mt}K_{max}$, where R_{mt} is the smallest muffin-tin radius in the unit cell and K_{max} is the magnitude of the largest K-vector in the basis set of plane waves. Increased accuracy of DFT calculations is correlated with increasing computational time, so $R_{mt}K_{max}$ is selected to balance the numerical accuracy needed within reasonable computational times.

CHAPTER 3

Kinetics of Growth Regimes of Hydrothermally Synthesized Potassium Tantalate ($KTaO_3$) Nanoparticles

3.1. Introduction

Nanoparticle synthesis can be approached with many goals in mind to produce materials with the right combination of composition, structure, and size for a specific application. This flexibility is why nanoparticles and their nanoscale properties have been studied to enhance their performance in fields like catalysis, energy, and drug delivery. [**14**, **28**–**31**] Therefore, shifting the focus of nanoparticle synthesis design beyond size control to obtain control over the shape NPs—in both broad features, such as Wulff shape or aspect ratio, as well as fine details, such as surface morphology, atomic arrangements, or growth terrace densities—is highly worthwhile to explore shape and surface dependent properties. The goal of this chapter is to study the kinetics of growth processes on NP surfaces produce particles with either rough or smooth morphologies. This understanding of why certain features are formed under specific conditions can lead to future studies on how to design the conditions to favor the growth of desired shapes and surfaces.

In Chapter 2 we described the crystal growth of NPs in terms of two simultaneous processes: (1) nucleation of terraces on particle surfaces, and (2) lateral growth of terraces. In combination with particle nucleation, the rates of these three processes can affect the size distribution, shape, and surface morphology of the NPs, but controlling them rates poses

a complex problem. Each process depends on many variables, including thermodynamic quantities (e.g. temperature, pressure, and chemical potential) associated with both the synthesis environment and materials used, which often have confounding effects, further complicating the study of NP growth processes.

The hydrothermal synthesis of KTO NPs was selected as the topic of this study. KTO is an incipient ferroelectric, a material that remains cubic until very low temperatures, making it structurally simpler to study with crystallographic characterization methods. [**57**] It has been synthesized using several techniques, including solvothermal, [**58**,**59**] hydrothermal, [**38**, **60**–**62**] supercritical, [**63**] and solid-state methods. [**64**, **65**] The relatively simple hydrothermal synthesis, which is composed of only two reagents and lacks the addition of surfactants, is an ideal candidate for studying the kinetics of NP growth processes and the relationship between the solution (Region I) and surface (Region III) in this context as described in Chapter 1.

In this chapter, a general mathematical model for growth kinetics is proposed based upon observed growth regimes of hydrothermally synthesized KTO NPs from XRD studies of the reaction rates and electron microscopy studies of their surface chemistry and morphology. Characterization of the evolving surface morphology over time with secondary electron imaging revealed two kinetically distinct growth regimes. The kinetic distinction is a result of the different rates of two growth mechanisms, terrace nucleation and terrace growth, which have different effects on the observed NP morphology. In the first regime, the rate of terrace nucleation dominates over that of terrace growth, resulting in rough, stepped surfaces. In the second regime, where the rate of terrace growth is instead higher, the surfaces become smooth. The proposed model uses classical step-flow growth

concepts to establish relationships between the two growth mechanisms and the chemical potential change throughout the reaction. HRTEM provided further insight into the role of different chemical species on the terrace nucleation and growth rates by characterizing the surface chemistry and structure.

The work presented in this chapter was done with some assistance provided by Jianguo Wen for the HRTEM imaging and Ahmet Gulec for the EDS analysis.

3.2. Methods

The hydrothermal synthesis of KTO NPs used was based on that described by Goh et al. 0.0025 mol of Ta_2O_5 powder (1.1 g) and 25 mL of 15 M KOH solution were added to a 125 mL Teflon-lined autoclave. [**38**] The autoclave was heated to 150 °C for 1–4 hr. For additional general hydrothermal synthesis procedure, please reference Chapter 2.

Powder XRD was performed on a Rigaku DMAX diffractometer equipped with a Cu K_α source operated at 40 kV and 20 mA. Phase fractions of each compound present were quantified from diffraction patterns by Rietveld refinement. [**49**]

SE imaging was performed on a Hitachi HD-2300 STEM operated at 200 kV. The practice of stereology was applied to extract random and statistical measurements of areal growth terrace densities from SE images. Figure 3.1 visually shows the terrace counting procedure. A linear probe (red line) was drawn and guided across a nanoparticle face (red arrows) in an image. At every instance where the line intersected with a terrace for the first time, it was counted and annotated to prevent miscounting (yellow lines). A "terrace" was considered to be a feature of high contrast on the nanoparticle facet. The

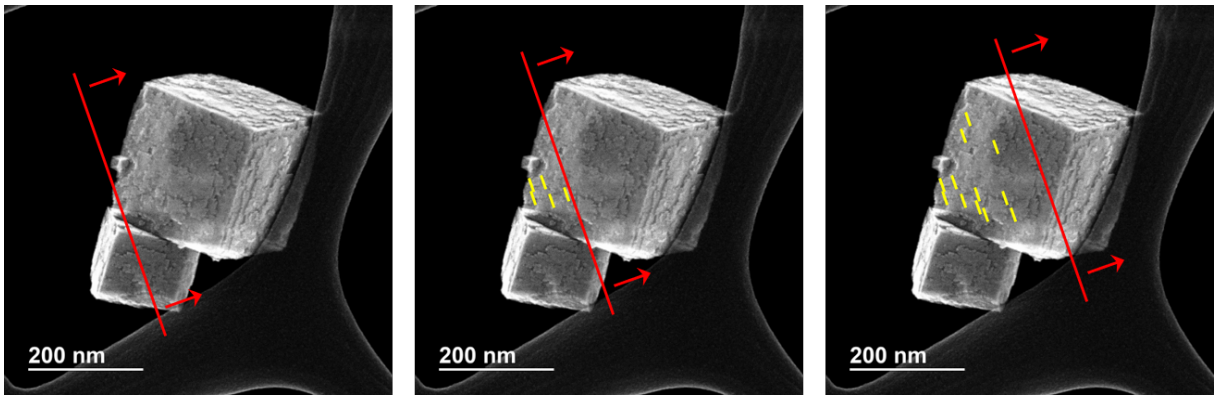

Figure 3.1. Schematic demonstrating the areal terrace density counting process. The red line is the linear probe, the red arrows define the direction in which the probe is moved across an image to count terraces, and the yellow lines identify tallied terraces. [**1**]

opposite edge of a counted terrace was not tallied. Using this approach, the linear probe prevented bias in the measurements by aiding the eye in counting intersections only.

HRTEM was performed on the ACAT to characterize the NP surfaces with profile imaging. [**41**–**45**] The electron beam dose was kept below 100 e^-/nm^2s to minimize beam damage of the sample. HRTEM images were simulated using the MacTempasX software package, [**47**] which uses the multislice method [**46**] and nonlinear imaging theory, [**66**] to interpret image contrast. EDS was performed on a JEOL ARM200CF STEM operated at 200 kV.

3.3. Results

In this section, we will begin by describing the general crystallography and reaction kinetics determined from XRD before examining the morphology and surface features. After this, characterization results of the surface chemistry and structure will be presented.

3.3.1. Growth Kinetics and Surface Morphology

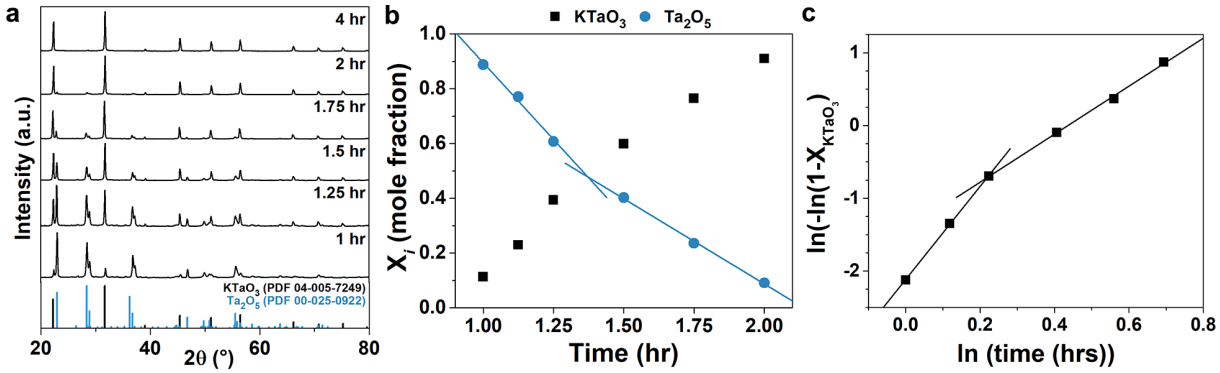

Figure 3.2. (a) XRD patterns of the hydrothermal synthesis products at time steps between 1 and 4 hr of synthesis. Between 1 and 2 hr, the patterns show signals from both the reagent L-Ta_2O_5 (blue bars, PDF 00-025-0922) and the product KTO (black bars, PDF 04-005-7249). At 2 hr, the conversion to KTO is almost complete, and by 4 hr, the pattern matches only KTO. (b) Mole fractions of yielded KTO (black squares) and remaining reactant Ta_2O_5 in product after different lengths of synthesis times. Blue lines indicate different rates of consumption of Ta_2O_5. Phase fractions were calculated with Rietveld refinement. (c) Logarithmic plot of the yield showing two different growth rates. [**1**]

Table 3.1. Rietveld refinement R-factors and goodness-of-fit for XRD patterns shown in Figure 3.2. [**1**]

Time (hr)	R_{wp} (%)	R_{exp} (%)	Goodness-of-fit (χ^2)	KTO (wt%)
1	9.19	3.22	8.13	10.1
1.125	11.06	6.16	3.22	17.2
1.25	9.42	3.25	8.41	33.7
1.5	7.24	3.37	4.61	56.6
1.75	6.52	3.36	3.77	75.8
2	7.00	3.33	4.41	91.5

Powder XRD patterns of the products after 1–4 hr of reaction time were acquired to identify and quantify the phases present at different times during the synthesis. These are shown in Figure 3.2a and were indexed to match L-Ta_2O_5 (PDF 00-025-0922) and cubic perovskite $KTaO_3$ (PDF 04-005-7249); no secondary phases were observed. The yield of KTO (black squares) and consumption of Ta_2O_5 (blue circles) over time were quantified from the XRD patterns using Rietveld refinement, as shown in Figure 3.2b, and Rietveld refinement details can be found in Table 3.1. Based on the quantification of the diffraction patterns, the reactant Ta_2O_5 is almost completely (∼94 mol%) converted to KTO after 2 hr. Furthermore, there is a change in the rate of reaction between 1.25 and 1.5 hr, as indicated by the change in rate of consumption of Ta_2O_5 (blue lines). Although the assumptions of the Johnson-Mehl-Avrami-Kolmogorov (JMAK) equation were not satisfied by this synthesis, [**67**–**70**] the reaction yield can still be fit to the functional form of the equation to analyze changes in the growth kinetics, i.e.:

$$X_{\mathrm{KTO}} = 1 - e^{-kt^m} \tag{3.1}$$

where X_{kto} is the fraction of product yielded at time t, k is a rate constant, and m is a constant that provides information about the growth process based upon JMAK theory. If this is plotted in the form $\ln(-\ln(1 - X_{\mathrm{KTO}}))$ as a function of $\ln t$, the data may be fit to linear functions with slope m, as shown in Figure 3.2c. The time period between 1–2 hr was chosen for this analysis because the system underwent a nucleation incubation period before 1 hr, and the reaction was almost complete after 2 hr. This data is well described by two linear fits—one for 1–1.25 hr and one for 1.25–2 hr—each with a different slope (~ 6 and ~ 3, respectively) suggesting two kinetically different growth regimes.

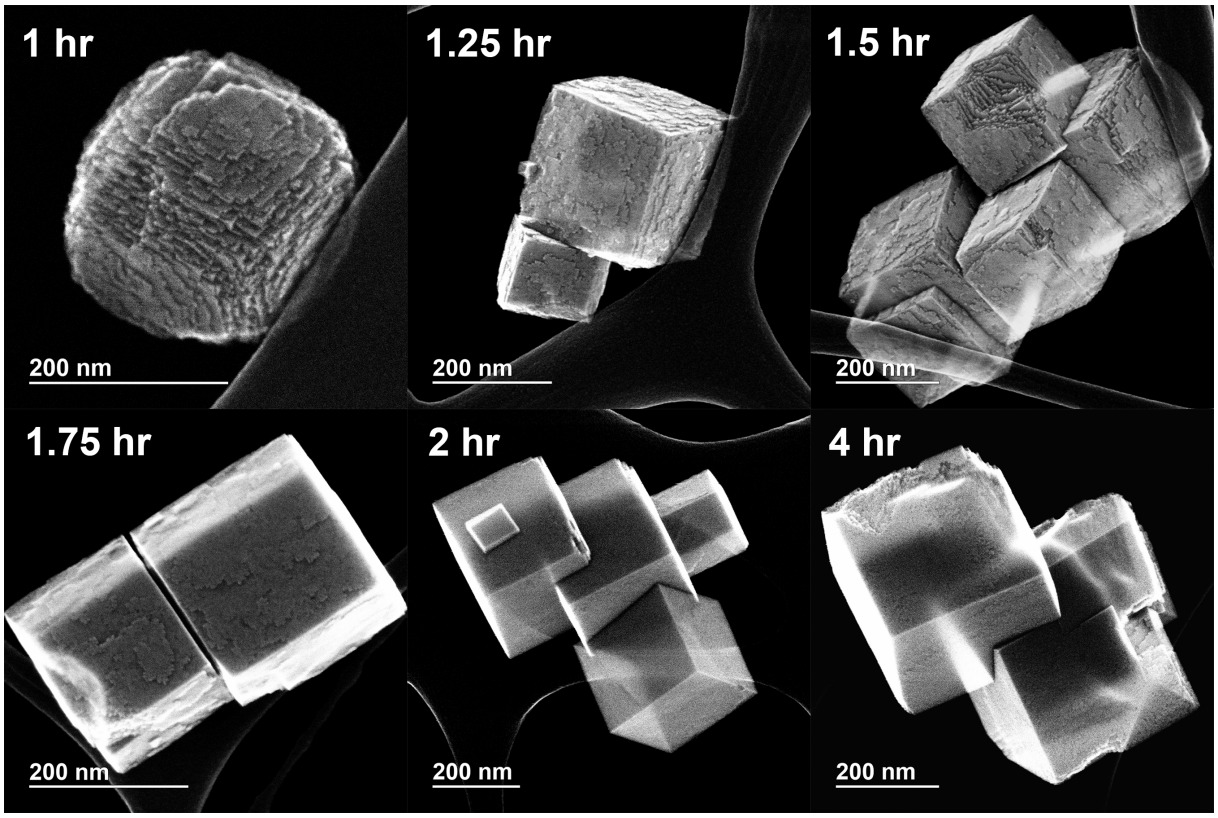

Figure 3.3. SE images of the KTO NPs after 1–4 hr of hydrothermal synthesis. Images show nanocuboids ∼200 nm in size with sharp corners and edges and evolving surface morphology with time. [**1**]

Similar to the reaction rate, the nanoparticle morphology also evolved over time. Figure 3.3 shows SE images of the samples, which were ∼200 nm sized cuboids. Between 1 and 1.75 hr, the nanoparticle facets were populated with many growth terraces, giving a relatively rough appearance. After 2 hr, the facets appeared smooth and resembled the final product imaged after 4 hr. The heights of the terraces were on the order of 1—3 unit cells of bulk KTO.

The areal terrace density distribution on the nanoparticles was measured for each time step between 1 and 1.75 hr (Figure 3.4a). The 2 hr time step was excluded here because

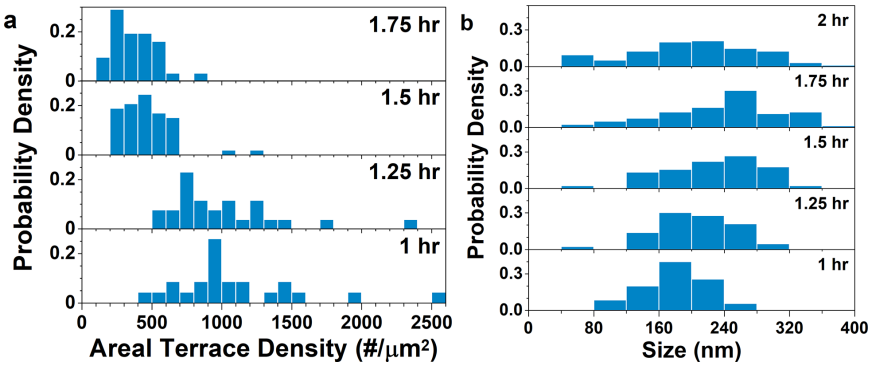

Figure 3.4. (a) Histograms of the areal terrace density measured on nanoparticle facets for 1, 1.25, 1.5, and 1.75 hr products. Histograms show narrowing distribution ranges and decreasing densities with time. (b) NP size distributions for synthesis times between 1 and 2 hr. Distributions broaden with increasing time, and the average size increases with increasing time until 2 hr, where the average size decreased from that of 1.75 hr. [**1**].

the surfaces appeared completely smooth. These plots demonstrate that the areal density of terraces (i.e. roughness) decreased and distribution range narrowed with time. The NP size distribution at each time step was also measured between 1 and 2 hr, and these are provided in Figure 3.4b as histograms. In contrast to the terrace density, the size distribution broadened and the average size increased as the synthesis progressed until 2 hr, where the average size decreased from 1.75 hr.

3.3.2. Surface Chemistry

The evolving surface morphology suggested that the NP surface structure and chemistry may play an important role in establishing a general growth model. A high resolution profile image of a NP oriented along the [110] zone axis from the 4 hr sample is shown in Figure 3.6a. The surface 1–2 nm of the NPs showed an approximately uniformly distributed phase with a differing lattice spacing and symmetry than bulk KTO. There was

also some structural disorder in the region between this surface phase and the bulk, which may be attributed to overlapping terraces of the NP and mismatch between the surface and bulk phases. Similar features were also observed on the 1 hr NP sample. Images of areas with well-ordered structure and little evidence of beam damage (i.e. dose rate less than 100 e^-/nm^2s) were used to determine the surface chemistry and structure. To interpret the contrast of the images and investigate possible structure matches for the surface, multislice HRTEM image simulations were performed mimicking the microscope and sample conditions using several potential structures to match the contrast and periodicity of these regions.

A range of possible structures were considered; taking into account that because both precursors and KTO contain Ta^{5+} and no reductants were used, only phases containing Ta^{5+} were chemically reasonable, i.e. potassium tantalate, tantalum(V) oxide, and tantalum(V) hydroxide. The structures were further narrowed based upon EDS data that

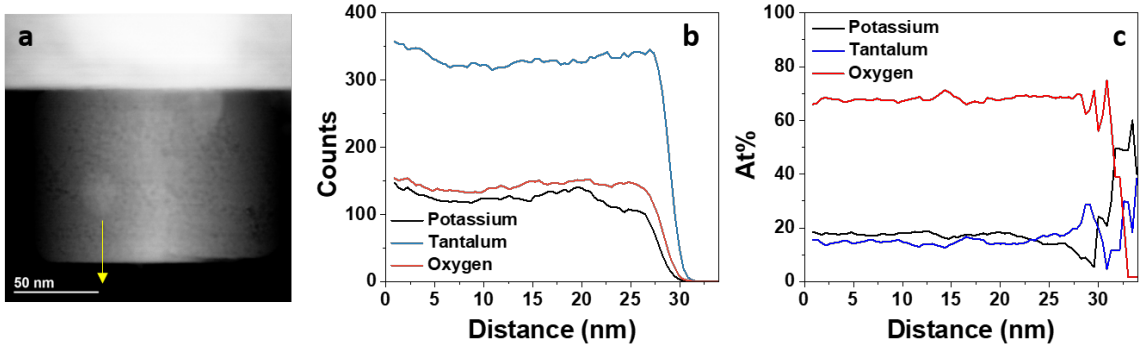

Figure 3.5. (a) Annular dark field image of KTO NP oriented on the [110] zone axis. Yellow line indicates [100] direction of EDS line scan. (b) Raw counts of EDS line scan where potassium signal is black, tantalum is blue, and oxygen is red. (c) Quantified EDS line scan from raw data in (b). Line scans show increasing tantalum signal at the edge of the particle. Line scan data was smoothed using a moving average filter. [**1**]

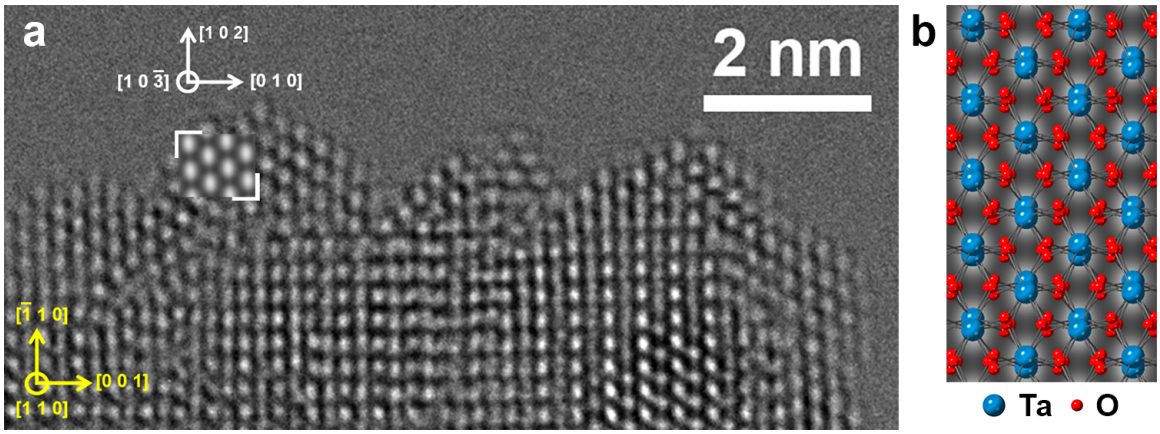

Figure 3.6. (a) Profile-view HRTEM image (with a dose rate of 30 e^-/nm^2s) of a 4 hr KTO NP oriented along the [110] zone with a multislice image simulation of B-Ta_2O_5 inset (white brackets). (b) Image simulation of B-Ta_2O_5 with the atomic structure superimposed, where the large blue atoms are Ta and small red atoms are O. [**1**]

suggested the surfaces were potassium deficient and tantalum-rich (Figure 3.5). Of all the possibilities, B-Ta_2O_5, a high-pressure polymorph of tantalum(V) oxide belonging to space group 15 ($C2/c$), [**71**] was the best match. A multislice simulation of B-Ta_2O_5 oriented along the $[10\bar{3}]$ zone axis is shown as an inset in Figure 3.6a (white brackets). Figure 3.6b shows the B-Ta_2O_5 atomic structure superimposed on the image simulation, where bright spots correspond to Ta atoms (blue) and dark spots correspond to O atoms (red). There is a lattice mismatch between the simulated B-Ta_2O_5 and bulk KTO of approximately 7% and -9% along the $[10\bar{3}]$ and [010] directions, respectively. While this mismatch is relatively large, such values for a thin surface region are not unreasonable.

This misfit strain may partially explain why the high-pressure B-Ta_2O_5 phase terminates the surface as opposed to the low temperature stable phase, L-Ta_2O_5. [**72**] Epitaxial strain stabilization of nonequilibrium stable phases has been demonstrated in many different cases including oxide thin films. [**73**,**74**] We note that the published L-Ta_2O_5 structural

information has longer bond lengths and did not match the experimental images. The literature reports the B-Ta_2O_5 phase to be only stable at high temperatures and pressures; [**71**] it has also been hydrothermally synthesized under pressure and temperature conditions of 20 MPa and 570 K. [**75**] Both reports demonstrated that the B-Ta_2O_5 phase is metastable at room temperature. Even though the reported syntheses of B-Ta_2O_5 were performed at higher temperatures and pressures than used in the syntheses used here, we can show that our hydrothermal conditions are still reasonable for forming this phase. By considering the mechanical properties of tantalum(V) oxide, the volume change under 20 MPa compared to the KTO hydrothermal synthesis conditions can be determined. The bulk modulus of L-Ta_2O_5 has been calculated to be between 140–144 GPa, [**76**] so the average value (142 GPa) is used in the following calculation. The volume change under a uniform pressure may be calculated according to the formula:

$$\frac{\Delta V}{V} = \frac{\Delta P}{B} \tag{3.2}$$

where ΔV is the volume change, V is the original volume, ΔP is the change in pressure, and B is the bulk modulus. Using this formula, the aforementioned literature values, and considering the extreme case of atmospheric pressure during KTO synthesis, $\frac{\Delta V}{V}$ was calculated to be 0.014%. Because this is such a small change, the lower pressure conditions were considered reasonable enough to feasibly form B-Ta_2O_5.

The experimental results and slope change in Figure 3.2b and 3.2c indicated that there were two growth regimes, an overall evolution over time of the surface morphology from rough surfaces with high areal terrace density to smooth surfaces with low terrace density, as well as an excess of Ta_2O_5 at the surface in the form of a high temperature and pressure

stable phase, which has a good epitaxial and tantalum coordination match to the KTO substrate. We will now show how these results can be understood in terms of a general growth model based upon conventional step-flow growth.

3.3.3. Growth Mechanisms and Model

The appearance of terraces on the NP surfaces and their subsequent smoothing is indicative of changing kinetics of growth processes. As described in Section 3.1, the growth of NPs can be described by two stages: (1) nucleation of terraces on NP surfaces and (2) lateral growth of terraces. Before proceeding to model the rates of these two processes, it is important to define several thermodynamic terms for this specific synthesis. In this case, the change in chemical potential ($\Delta\mu$) per molecule added to the NP is dependent on the chemical potential difference between the inital reactants (Ta_2O_5 and KOH) and the final product (KTO). $\Delta\mu$ can vary with many factors, including reagent concentration, temperature, pressure, and volume.

In this synthesis, since the molar ratio of the reagents KOH:Ta_2O_5 is 150:1, the concentration of KOH is essentially constant over the course of the synthesis reaction. Given the incubation period of 1 hr, it was also assumed that the species were sufficiently mixed so that the overall $\Delta\mu$ was not affected by dissolution rates and concentration distributions. Furthermore, because the hydrothermal synthesis was performed at a constant temperature and pressure inside a closed vessel of fixed volume, these variables may also be considered constant. Thus, $\Delta\mu$ primarily varied with the concentration—i.e. supersaturation—of Ta_2O_5 in solution, which decreased over time as the reaction yield increases, meaning that $\Delta\mu$ became less negative over time. A direct relationship between

$\Delta\mu$ and the Ta_2O_5 concentration was difficult to calculate under the circumstances because the reaction took place in a sealed autoclave under relatively high temperature and pressure. This prevented the direct study of the solute species present, the free energies of those species during the reaction, the exact chemical reaction mechanisms occuring, and the specific thermodynamic conditions of the system. As also mentioned earlier, and will become clearer below, there are other specific quantities for which only reasonable estimates are possible at present, e.g. step energies in solution at elevated temperature and pressure. However, in this case, the specific solutes present and any intermediate reactions occurring are of little consequence compared to the overall reaction from the initial reactants to the final product, which is the key reaction that results in the growth of NPs. This overall reaction generates the effective $\Delta\mu$, the relative value of which may be reasonably related to the concentration of Ta_2O_5 given the assumptions made above.

The results of the HRTEM characterization and multislice image simulations provided further evidence that the concentration of Ta_2O_5 controls the kinetics of the NP synthesis. Figure 3.6a demonstrates that the surface of KTO is terminated by B-Ta_2O_5, a tantalum oxide phase rather than a potassium tantalate phase, which has been observed in other KTO surface studies. [**77**, **78**] This further suggests that the tantalum species in solution was a major factor in controlling $\Delta\mu$ during the reaction.

In Chapter 2, we showed that the terrace nucleation rate could be modeled as a simple Arrhenius equation, as shown below.

$$N_R = f_0 \exp \frac{\Delta E}{k_B T} \qquad \text{(2.5 revisited)}$$

A geometric model for terrace nucleation was used to determine the energetic quantities contained in the activation energy (ΔE). Here we will use a similar approach by modeling the terraces as 2D flat nuclei such that the activation energy is dependent on the step edge energy (γ_e) of the terrace, i.e.:

$$\Delta E = \frac{-\pi(N_E\gamma_e)^2}{N_S\Delta\mu^2} \tag{3.3}$$

where N_E is the number of atoms per unit length of a terrace and N_S is the number of atoms per unit area of a terrace. Notably, ΔE is inversely proportional to the driving force ($\Delta\mu$). In contrast, recall that the rate of terrace growth (G_R) is linearly dependent on $\Delta\mu$:

$$G_R = C\Delta\mu \tag{2.6 revisited}$$

In order to more directly compare the rates of terrace nucleation and terrace growth, the process of terrace annihilation is defined when a terrace grows across a facet and reaches the edges, annihilating itself. The rate of annihilation (A_R) is proportional to the terrace growth rate:

$$A_R = \frac{1}{A}G_R \tag{3.4}$$

where A is the size of the specific nanoparticle face.

N_R and A_R were simulated for the KTO hydrothermal system with a reaction temperature of 150 °C and nanoparticle facet size of 200 nm. Figure 3.7 shows these N_R (solid) and A_R (dashed) plotted against $\Delta\mu$ using estimated step edge energies of 0.4 and 0.2 eV/atom, respectively, to demonstrate the rate dependence on both material properties and synthesis conditions. These energies were estimated using known values

in literature for similar materials. Additional estimations used in these simulations can be found in Section 3.3.3.1. N_R and A_R intersect at a value $\Delta\mu_{\text{critical}}$ where the dominating growth process changes, and $\Delta\mu_{\text{critical}}$ generally tends to be on the same order as γ_e. Notably, $\Delta\mu$ is on a negative scale where a large supersaturation or high driving force corresponds to a large negative value and small supersaturation or low driving force corresponds to a less negative value. The terracing and smoothing regimes are indicated on either side of $\Delta\mu_{\text{critical}}$ by yellow and blue shaded regions. When $\Delta\mu < \Delta\mu_{\text{critical}}$, $N_R > A_R$ and more terraces will be nucleated than annihilated, resulting in the appearance of rough, terraced surfaces. When $\Delta\mu > \Delta\mu_{\text{critical}}$, $N_R < A_R$ and more terraces will be annihilated than nucleated, resulting in a smooth appearance. As discussed earlier, $\Delta\mu$ became less negative as the synthesis of KTO progressed, which meant that it moved from left to right in the plot of Figure 3.7a—moving from the terracing regime to the smoothing regime, as observed in Figure 3.3. While the exact value of $\Delta\mu$ cannot be calculated for this particular synthesis, the most important relationship is where $\Delta\mu$ is relative to $\Delta\mu_{\text{critical}}$, thereby determining which growth mechanisms dominates.

The transition between the two growth regimes is also dependent on the NP size because the annihilation rate increases with decreasing NP facet area, as well as the reaction temperature. Figure 3.7b and d show $\Delta\mu_{\text{critical}}$ calculated for a series of reaction temperatures and NP sizes when γ_e is 0.4 and 0.2 eV/atom, respectively. $\Delta\mu_{\text{critical}}$ becomes more negative with decreasing temperature and NP size, widening the $\Delta\mu$ range where the smoothing regime will dominate. In contrast, with increasing temperature and NP sizes, $\Delta\mu_{\text{critical}}$ increases, which increases the $\Delta\mu$ range where the terracing regime will dominate.

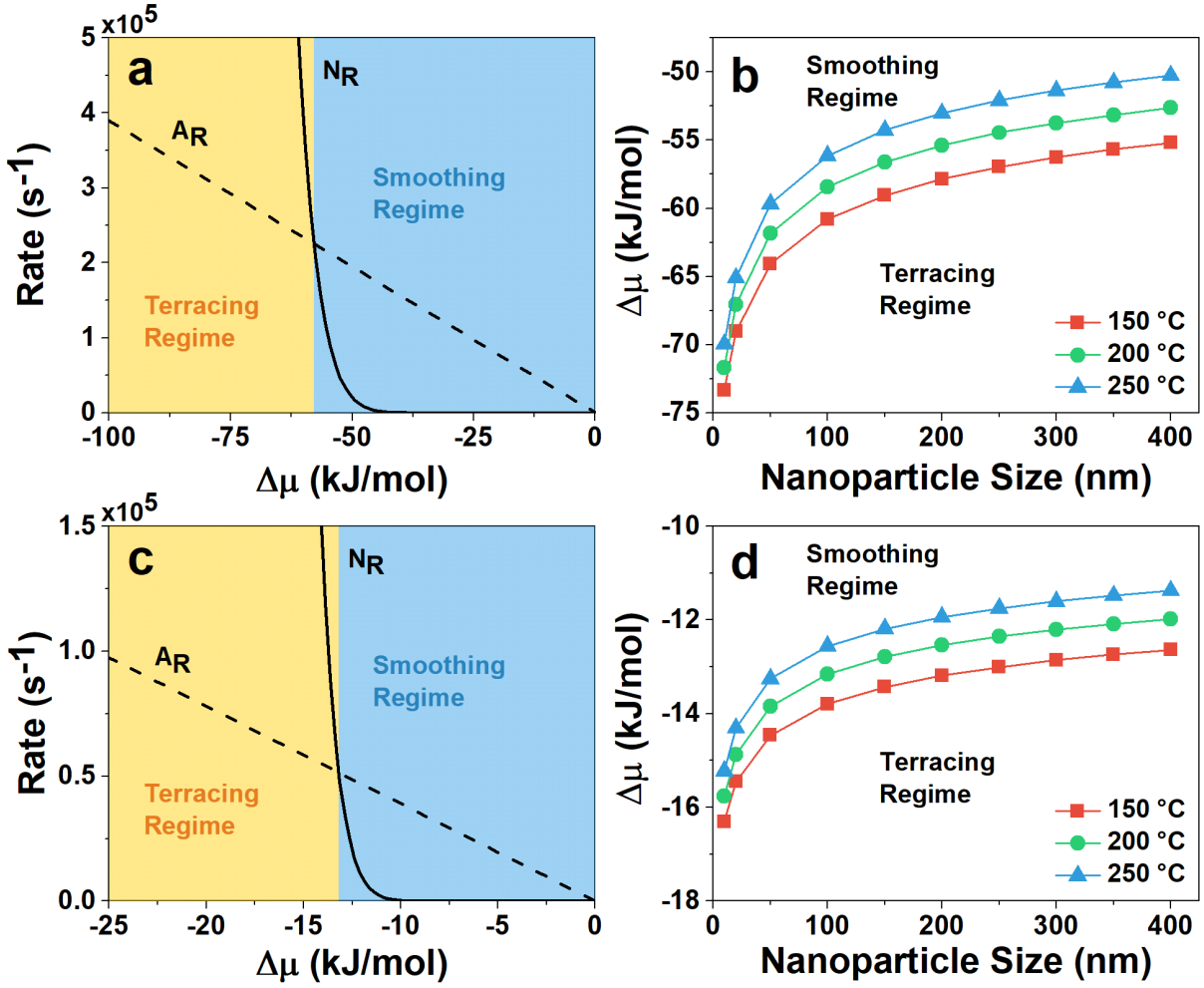

Figure 3.7. Terrace nucleation rate (solid) and annihilation rate (dashed) simulated as a function of $\Delta\mu$ for a reaction temperature of 150 °C and nanoparticle size of 200 nm using estimated γ_e of (a) 0.4 eV/atom and (c) 0.2 eV/atom. N_R and A_R intersect at $\Delta\mu_{\text{critical}}$, which is where the dominant growth regime switches between terracing and smoothing. Corresponding plots of $\Delta\mu_{\text{critical}}$ as a function of nanoparticle size for different synthesis temperatures γ_e of (b) 0.4 eV/atom and (d) 0.2 eV/atom. [**1**]

3.3.3.1. Estimations for model simulation. Several additional estimates based upon classical growth models and literature values were necessary to generate the plots shown in Figure 3.7 from Equations 2.5 and 3.4. The unknown variable in Equation 2.5 is

the pre-exponential factor. A reasonable estimate for the frequency factor (f_0) in a phase transformation is the Debye frequency of a lattice, which is about 10^{13} Hz. [**79**] In additon, the frequency factor has been found to be about 10^{11} Hz for gaseous or biomolecular reactions. [**80**] For this solution-based system, a value of 10^{12} Hz was used as an average of those two frequencies.

Similarly, the primary concern for the terrace growth and annihilation functions is the coefficient C. Drawing from thin film growth models, C is also dependent on the diffusion of reagents to the surfaces of the particles, which can be estimated by the frequency factor (f_0) . It may be further assumed that molecules diffusing to the surface will either remain on the surface and diffuse to a terrace or desorb, which can be accounted by an Arrhenius term including activation energies for both surface diffusion (E_{sd}) and desorption (E_{des}). Then, the geometry of the terrace can be accounted for by including N_E and N_S defined earlier. Lastly, a temperature dependence term must be added for the chemical potential term, such that the coefficient C has the final form:

$$C = f_0 \exp\left(\frac{E_{des} - E_{sd}}{kT}\right)\left(\frac{N_E}{N_S}\right)\left(\frac{1}{kT}\right) \tag{3.5}$$

All energy related values were estimated based upon activation and step edge energies of similar materials from literature. [**79**, **81**]

3.4. Discussion

The model presented illustrates a case where the two processes—nucleation and growth of terraces—can dominate at different points during a synthesis owing to changes in $\Delta\mu$. Therefore, by controlling $\Delta\mu$ during a synthesis, various properties of the product can be

tuned, including surface morphology and size distribution. As evidenced by Figures 3.3, 3.6, and 3.7, nanoparticle surfaces can be relatively rough or smooth depending on which growth process is dominating. When the driving force is great (i.e. large negative $\Delta\mu$), terrace nucleation is the prevailing process and NP surfaces will be rough. When the driving force is small (i.e. less negative $\Delta\mu$) the NP surfaces will be smooth instead because terrace growth is dominant. Either surface morphology can be advantageous depending on the needs of an application. For example, NPs with rougher surfaces can be beneficial for applications where high surface area is needed, as in catalysis. [**28**] Smooth, well-controlled surfaces and shapes are also important for identifying surface and shape-dependent properties. [**30**]

In addition, the change in slope shown in Figure 3.2b and c can be explained by applying the proposed growth model. The two different linear fits implied that there were two growth regimes with different kinetics during the synthesis of the nanoparticles, and that the regime changed when the dominant growth mechanism also changed. In this case, this occurred at 1.25 hr, and the rate change may be correlated to moving from the terracing regime to the smoothing regime. Based upon the proposed growth model, terrace nucleation was the dominant mechanism between 1 and 1.25 hr, and terrace growth dominated after 1.25 hr.

Beyond the surface morphology, the size distribution of NPs may also be affected by these growth processes. Typically, a monodisperse product can be achieved by increasing the NP nucleation rate at the beginning of the synthesis so that most of the nucleated particles grow at the same rate for the same length of time. However, Figure 3.4b shows that the size distribution of the NPs here broadens with time. Furthermore, between 1.5

and 2 hr, there is an increasing population of NPs below 100 nm in size. The broadening size distribution can be attributed to the different nucleation and growth rates in the two regimes described. As nucleated NPs form at later time steps, they will remain small and smooth in appearance because the terrace growth process is dominating over the terrace nucleation process. Terrace nucleation is growth normal to NP surfaces, which will increase NP size, whereas terrace growth is growth parallel to NP surfaces, which will instead smooth the surfaces. Therefore, to achieve monodisperse NPs, it is not only important to nucleate most of the NPs at the same time but also to isolate the regime where terrace growth dominates from the NP nucleation time period.

3.5. Conclusions

A growth model describing on the kinetics of terrace nucleation and growth regimes on NP surfaces based upon conventional growth theory was proposed based on experimental observations of hydrothermally synthesized KTO NPs. In this synthesis, the NPs first undergo a regime of high terrace nucleation rate, followed by a regime of high terrace growth rate. The terrace growth dominant regime coincides with a regime where heterogeneous nucleation also dominates, resulting in smooth, faceted NPs. The balance of terrace nucleation and growth rates can control many characteristics of the products, including the relative roughness or smoothness of the surfaces, how facted the NPs are, and the size distribution. The rates of the growth processes are dependent on the chemical potential change of the synthesis environment. By tuning the chemical potential difference through different variable, size and shape controlled syntheses of NPs may be achieved. The proposed model may be used to better explain the observed behavior in other cases

of hydrothermally synthesized perovskite oxide NPs. We discuss these in more detail in Chapter 7. It may also be used to inform nanoparticle synthesis design to produce smooth, well-faceted, and shape-controlled NPs, as shown in Chapter 6.

CHAPTER 4

Chemisorption-Driven Roughening of Hydrothermally Grown Potassium Tantalate Niobate ($KTa_{1-x}Nb_xO_3$) Nanoparticles

4.1. Introduction

In the previous chapter, the nanoparticle growth processes in terms of terrace nucleation and terrace growth were experimentally observed during the hydrothermal synthesis of KTO NPs. It was demonstrated that the competition between the rates of these two processes directly affected the morphology of the nanoparticle surfaces, and this kinetic competition led to two different growth regimes. The terracing regime is designated when terrace nucleation dominates and is characterized by the growth of rough surfaces, while the smoothing regime occurs when terrace growth dominates, resulting in flat NP surfaces. The terrace nucleation rate (N_R) and terrace growth rate (G_R) are affected by many variables, including the overall driving force of the reaction, chemical potentials of each component in the system, and other thermodynamic quantities. Therefore, it is important to understand these relationships so that these variables may be tuned for specific shapes, as will be demonstrated in Chapter 6. [**5**]

The growth behavior of KTO nanoparticles is an example of how the properties of the solution (Region I) and the surface (Region III) can be directly related in a synthesis as described in Chapter 1. This chapter takes another step in understanding the relationship between material properties, synthesis environment conditions, and growth

behavior by examining the consequences of interactions between species in solution and the growing surface. The role of chemisorption in enhancing the formation rate of growth terraces is explored through the study of hydrothermally synthesized KTO, KNO, and KTN particles. KTO and KNO are perovskite oxides that share many similarities, including their hydrothermal synthesis "recipes." They can also form the solid solution potassium tantalate niobate (KTN), which has itself been studied for its compositionally tunable dielectric, ferroelectric, and electro-optic properties. [**61**, **82**–**86**]

A series of nanoparticles were synthesized in the $KTa_{1-x}Nb_xO_3$ (x = 0–1) family of materials, and it was observed that their particle surfaces possess different compositions and structures that can significantly change the kinetics of crystal growth processes. Two different composition-dependent growth modes were identified: Nb-rich surface experienced chemisorption-driven roughened growth, whereas Ta-rich surfaces grew smooth, flat surfaces via step-flow growth. Electron microscopy characterization, DFT calculations, and mathematical growth models were used to illuminate the role of surface properties and chemisorption on the NP growth morphology.

The work presented in this chapter was done in collaboration with Jianguo Wen, who provided assistance with HRTEM, and Ryan Paull, who helped perform the thermogravimetric analysis coupled with gas chromatography-mass spectroscopy.

4.2. Methods

Hydrothermal synthesis was used to synthesize KNO, KTO, and KTN NPs. Following Kumada et al. [**40**] to form KNO NPs, 0.0121 mol Nb_2O_5 and 0.363 mol KOH were added to a 45 mL Teflon-lined autoclave with 26 mL deionized water and heated to 200 °C

for 12 hr. The KTO NPs were synthesized following Goh et al. [**38**, **39**] and Chapter 3, where 0.0025 mol Ta_2O_5 and 25 mL KOH were heated in an autoclave to 150 °C for 4 hr. KTN NPs were formed using two methods to produce samples KTN-1 and KTN-2. The KTN-1 sample was synthesized by modifying the KTO synthesis; a 1:1 ratio of Ta_2O_5 and Nb_2O_5 (0.0025 mol total) and 25 mL 15 M KOH were heated in an autoclave to 200 °C for 12 hr. KTN-2 NPs were synthesized by first dissolving 0.00125 mol Nb_2O_5 in 8 ML of 4 M KOH by heating them in a Teflon-lined autoclave at 200 °C for 16 hr. The resulting clear solution was combined with 0.00125 mol Ta_2O_5 and 18 mL of 20 M KOH to form an overall 15 M KOH solution, which was subsequently heated to 200 °C for 24 hr in an autoclave. In all cases, after cooling to room temperature, the products were washed and centrifuged with deionized water several times before being dried overnight at 80 °C.

Powder XRD was performed on a Rigaku Ultima diffractometer with a Cu K_α source. SE imaging and EDS were performed on a Hitachi HD-2300 STEM operated at 200 kV, and HRTEM was performed using the ACAT at Argonne National Laboratory. HRTEM images were simulated with the MacTempasX software package. [**47**]

DFT calculations were performed using the WIEN2k package, an all-electron augmented plane wave plus local orbitals package code. [**55**, **56**] Energies of the constructed surface slabs were calculated with the modified Perdew-Burke-Ernzerhof generalized gradient approximation functional (PBEsol). [**54**] To confirm that the PBEsol functional was appropriate for calculating the energies of these materials, the enthalpy of formation for niobium oxide was calculated and compared to the literature. R_{mt} were set to 1.79, 1.71, 1.25, and 0.5 bohr for Ta, Nb, O, and H, respectively. The cutoff parameter $R_{mt}K_{max}$ was set to 2.5 and 6.25 for structures with and without hydrogen, respectively, to keep K_{max}

consistent between calculations with different smallest R_{mt}. The k-point mesh density was also consistent between bulk and surface calculations. For the P phase calculation, a k-point mesh of 10 × 10 × 10 was used for the bulk and 2 × 6 × 1 for the surface. For the B phase calculations, a k-point mesh of 7 × 6 × 7 was used for the bulk and 4 × 3 × 1 for the surface. E_{surf} was calculated according to the equation:

$$E_{surf} = \frac{E_{slab} - n_{bulk}E_{bulk} - n_{H_2O}E_{H_2O}}{2\ Area} \tag{4.1}$$

where E_{slab} is the total energy of the slab, E_{bulk} is the energy of the bulk M_2O_5 (M = Ta or Nb), n_{bulk} is the number of bulk unit cells, E_{H_2O} is the energy of a single water molecule, n_{H_2O} is the number of water molecules, and $Area$ is the area of the surface slab. E_{H_2O} was calculated by isolating a single water molecule in a 10 Å cell to avoid interactions and performing the calculation with 1 k-point. Surface energies were converged within 0.01 J/m^2 against $R_{mt}K_{max}$, k-point mesh density, slab size, and vacuum. Adsorption energy per water molecule (E_{ads}) was calculated using the equation:

$$E_{ads} = \frac{E_{wet} - E_{dry} - n_{H_2O}E_{H_2O}}{n_{H_2O}} \tag{4.2}$$

where E_{wet} is E_{slab} when n_{H_2O} >0, and E_{dry} is E_{slab} when $n_{H_2O} = 0$.

Thermogravimetric analysis coupled with gas chromatography-mass spectrometry was performed on a Netzsch Jupieter F3 STA. The samples were heated from room temperature to 900 °C at a rate of 10 °C/min in nitrogen atmosphere.

4.3. Results and Discussion

In this section, we will begin by presenting the results of material characterization of the several NP samples synthesized. The compositional, structural, and chemical conclusions reached through characterization were used in the formulation of structure models of the NP surface phases. Then, the energetic effects determined from calculations performed on these models were used to summarize the growth behavior of the studied materials through kinetically defined growth regimes.

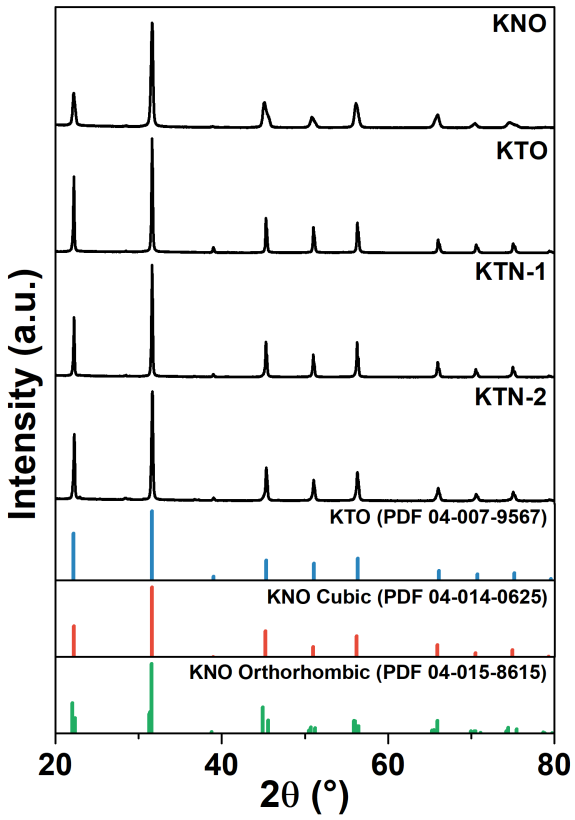

Figure 4.1. Powder XRD patterns of the KNO, KTO, KTN-1, KTN-2 samples. The KNO sample was matched to both cubic and orthorhombic phases KNO phases, while the KTO, KTN-1, and KTN-2 samples were matched to the cubic perovskite phases. [**2**]

XRD characterization of the samples confirmed that the perovskite phases were produced during hydrothermal synthesis, as shown in Figure 4.1. The KNO sample matched to both cubic and orthorhombic KNO phases (PDF 04-014-0625 and 04-015-8615), while the KTO sample matched the cubic KTO (PDF 04-007-9567) phase. Both KTN-1 and KTN-2 matched well to the cubic KTO and KNO phases.

Although the samples produced were similar in phase, the morphology and composition of the NPs showed several significant differences. SE images of all of the samples are provided in Figure 4.2. The average sizes of the KNO, KTO, KTN-1, and KTN-2 NPs were about 400, 200, 350, and 300 nm, respectively. While the KTO NPs had sharp corners and smooth facets, the KNO NPs had rounded corners and significantly rougher facets. The two KTN samples differed significantly as well. Figure 4.2 shows that the KTN-1 surfaces resembled the rough KNO NP facets, whereas the KTN-2 sample shared the smooth, flat facets of the KTO NPs.

EDS maps obtained for the two KTN samples to characterize the distribution of Ta and Nb throughout the samples showed even more differences and are provided in the last column of Figure 4.2. Both samples were compositionally heterogeneous and had composition gradients between Nb (yellow) and Ta (blue) in opposite directions. KTN-1 had a Ta-rich bulk and Nb-rich surface, while KTN-2 had a Nb-rich bulk and Ta-rich surface. The opposite composition profiles indicate a difference in reaction kinetics between the two synthesis approaches, where the element composing the interior corresponded to the faster reacting compound. This is illustrated in the schematic provided in Figure 4.3.

The relative reaction rate can be simply related to the relative chemical potentials of the aqueous Ta or Nb species throughout the reaction, which are in turn related to the

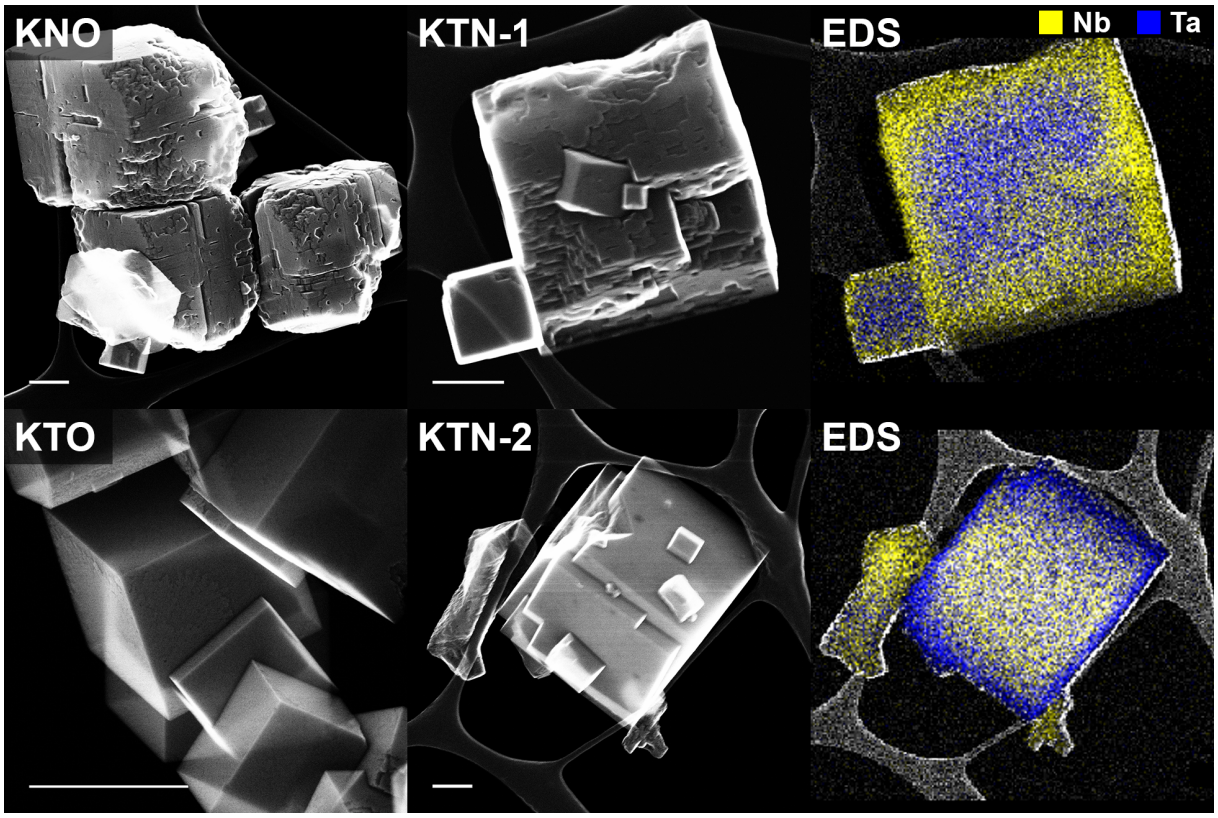

Figure 4.2. SE images (scale bars = 200 nm) of KNO, KTO, KTN-1, and KTN-2 NPs with average sizes of 400, 200, 350, and 300 nm, respectively. All four samples were cuboidal in shape. The KNO and KTN-1 NPs had rough surface morphologies, while the KTO and KTN-2 samples had smooth and fllat surfaces. EDS maps of KTN-1 and KTN-2 samples showed different composition gradients between Nb (yellow) and Ta (blue). The KTN-1 NPs had a Ta-rich bulk and Nb-rich surface, whereas the KTN-2 NPs had a Nb-rich bulk and Ta-rich surface. [**2**]

concentration of each species in solution. During the KTN-1 synthesis, the tantalum oxide became a more reactive species compared to niobium oxide in the KOH solution, thus the Ta species more readily reacted with KOH and became the first to be depleted, leaving the Nb species to react second and form a Nb-rich surface at the end. In contrast, the chemical potential of Nb in solution was deliberately increased for the KTN-2 synthesis by pre-dissolving Nb_2O_5 powder in a less alkaline solution before the final reaction. The

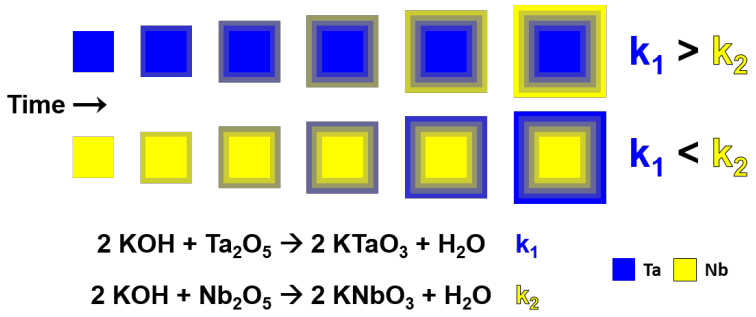

Figure 4.3. Schematic demonstrating how different reaction rates can cause heterogeneous composition gradients in nanoparticles. k_i represents the reaction rate for the KTO ($i = 1$) or KNO ($i = 2$) chemical reaction.

increased $\Delta\mu_{\mathrm{Nb}}$ caused it to react first, leading to Ta enrichment of the final surface after Nb was depleted from solution. It is probable that the reaction between Nb_2O_5 and KOH to form KNO involves the formation of an intermediate species stable in basic solutions, such as the Lindqvist ion ($Nb_6O_{19}^{8-}$). [**39**, **87**, **88**] During the Nb_2O_5 powder pre-dissolving procedure for the KTN-2 synthesis, the Lindqvist ion was most likely formed in solution, reducing the total number of reactions required to form the final perovskite phase. In contrast, when the same pre-dissolving procedure was performed with Ta_2O_5 powder, the Ta_2O_5 remained solid, indicating that its aqueous form is less solution stable than that of Nb_2O_5, contributing to its higher reaction rate to forming the perovskite phase.

Notably, the surface composition and morphology of each KTN sample matched the composition and morphology of the pure KNO and KTO samples: the Nb-rich surfaces (KNO and KTN-1) were rough, and the Ta-rich surfaces (KTO and KTN-2) were smooth. Terraced and smooth surface morphologies were previously explored in Chapter 3 using a step-flow growth model for KTO NPs, where two kinetically distinct growth regimes were identified at the early and late stages of growth. A similar approach was used here to identify the origins of the rough surfaces imaged on the KNO and KTN-1 samples.

Instead of a chemical potential dependent and time-correlated growth regime shift between terracing and smoothing growth behavior, a link between the surface composition and growth behavior is most likely.

Figure 4.4 shows HRTEM profile images of the surfaces of KTO, KNO, and KTN-1. The KTO image is reproduced from Chapter 3 and includes the multislice simulation of the surface B-Ta_2O_5 phase inset. In comparison to KTO, the surface oxides in both KNO and KTN-1 were clearly different. To identify the structure and phase of their surfaces, multislice HRTEM image simulations were first used to determine possible surface phases by matching the image contrast of the surfaces shown in Figure 4.4. In addition to the corresponding B-Nb_2O_5 phase, other potassium niobate, niobium (v) oxide, and niobium (V) hydroxide phases were simulated to match the Nb-rich surfaces. The phases that best matched were P-Nb_2O_5 and R-Nb_2O_5, which are two crystallographically similar medium temperature-stable Nb_2O_5 phases. [**89**–**92**]

Then, surface energy calculations were performed with DFT using these possible matches to determine the most stable surface phase. Model surface slabs were constructed following Pauling's rules adapted for oxide surfaces [**93**] and according to the zone axis that best matched the HRTEM image contrast based on multislice simulations. The surfaces were truncated along the exposed facets indicated in Figure 4.4 by the dotted yellow lines. The best match and most stable surface phase was identified as P-Nb_2O_5 because the R phase only relaxed into high energy, unreasonable structures. Multislice image simulations of P-Nb_2O_5 are inset in Figure 4.4 for both KNO and KTN-1. For completeness, surface slabs of B-Ta_2O_5 and the analogous B-Nb_2O_5, which did not match the experimental observations, were also constructed and relaxed for comparison.

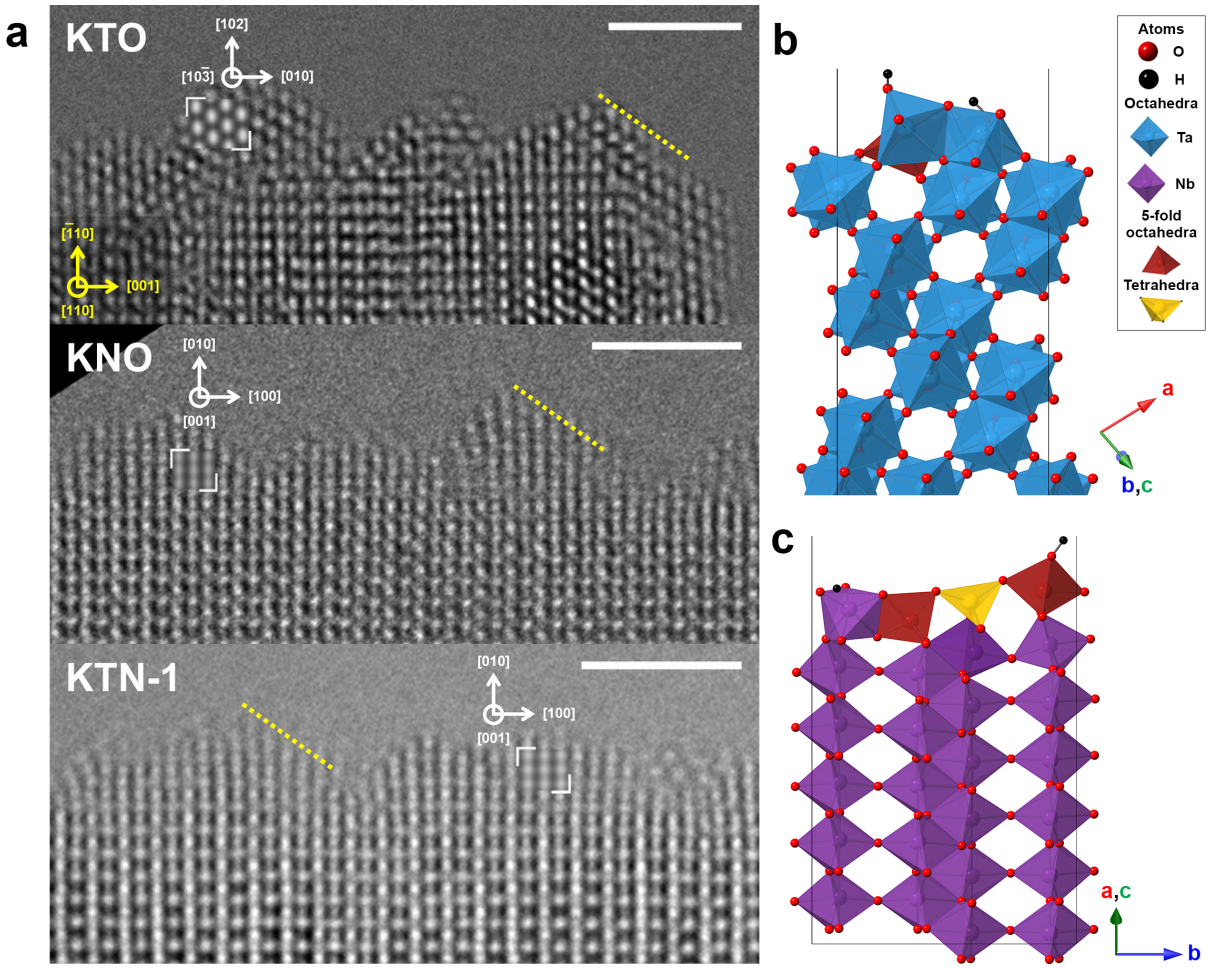

Figure 4.4. (a) HRTEM surface profile images of KTO, KTN-1, and KNO NPs oriented on the [110] zone (scale bars = 2 nm). Multislice simulations of B-Ta_2O_5 and P-Nb_2O_5 surface phases are inset into images (white brackets). (b) B-Ta_2O_5 and (c) P-Nb_2O_5 structures with surface terminations corresponding to the yellow dotted line in (a). Red atoms are oxygen; black atoms are hydrogen; blue octahedra are Ta octahedra; purple octahedra are Nb octahedra; yellow polyhedra are tetrahedra; dark red polyhedra are 5-fold coordinated polyhedra. [**2**]

The nanoparticles were all synthesized under highly alkaline aqueous conditions, which can cause hydration of the surfaces. In order to account for all possible surface conditions,

thermogravimetric analysis coupled with gas chromatography-mass spectrocopy (TGA-GC-MS) was used to analyze the surface adsorption chemistry of the KTO, KTN-1, and KNO samples. The results are plotted against temperature in Figure 4.5. The top row shows the mass loss percentage across all three samples during the heating sequence, and the shaded regions plotted in the bottom row correspond to the GC-MS data identifying signal corresponding to water (blue) and carbon dioxide (red). The KTO sample experienced the most mass loss (0.22 %). In contrast, the KNO and KTN samples only underwent a 0.05 % and 0.08 % change, respectively.

The GC-MS results show that most of the mass loss may be attributed to adsorbed water and carbon dioxide species in all three cases. Water loss occurred primarily between the temperatures of 30-600 °C, and carbon dioxide loss occurred between 200-550 °C. The

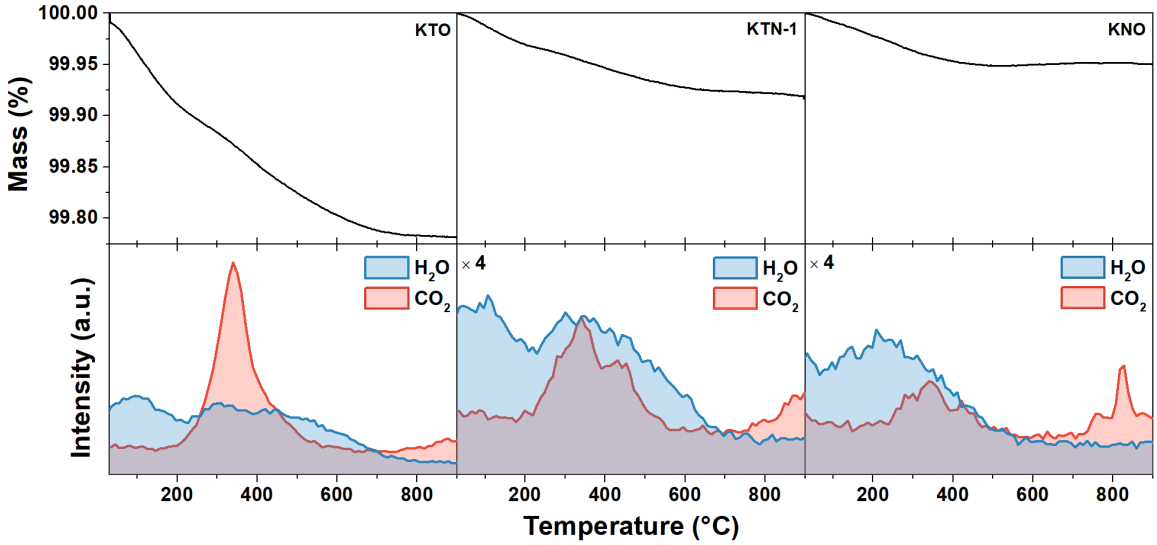

Figure 4.5. TGA-GC-MS analysis of KTO, KTN-1, and KNO particles. The top row shows mass loss across all three samples during the TGA heating sequence from room temperature to 900 °C. The GC-MS results are shown across the bottom row, where the shaded blue region indicates mass loss corresponding to water, and the red shaded region corresponds to carbon dioxide. [**2**]

water loss signal shows two distinct regions; one centered around 100 °C, and the other above 200 °C. These two regions may be attributed to physisorbed and chemisorbed water loss, respectively, because chemisorbed water has higher binding energies than physisorbed water. In the higher temperature region, the ratios of H_2O/CO_2 loss are 0.7, 1.2, and 1.1 for KTO, KTN, and KNO, respectively. Because of the limits established by the synthesis set-up and TGA-GC-MS instrument, it is difficult to prevent immediate adsorption of ex-situ species upon exposure to air and therefore also a challenge to quantify the initial populations of adsorbed species on all the sample surfaces. However, the temperature dependent desorption of the overall species suggested that the Nb-rich surfaces of KTN-1 and KNO have significant water chemisorption.

Surface slabs for P-Nb_2O_5, B-Nb_2O_5, and B-Ta_2O_5 were constructed under several different conditions: dry and wet (with both dissociated and undissociated water bonding configurations). The lowest surface energies for both dry and wet calculations on the three types of surfaces are provided in Table 4.1 as well as the adsorption energies for water molecules on the surfaces. The dry P-Nb_2O_5 surface had the lowest surface energy overall. In all cases, chemisorbed water reduced surface energy, but it was particularly favorable for the P-Nb_2O_5 structure, where the surface energy decreased by about 0.5 J/m^2 compared to 0.3 J/m^2.

The large stabilizing effect water chemisorption had on the P-Nb_2O_5 surface energy played a role in the terracing behavior of the Nb-rich surfaces during growth. We can recall the geometric model introduced in Chapter 1 to elaborate on why surface energy is an important quantity to consider when studying the kinetics of growth processes. In this model a terrace was constructed as a 3D hemisphere such that the change in energy

Table 4.1. Calculated surface energies for P-Nb_2O_5, B-Nb_2O_5, and B-Ta_2O_5 surfaces under dry and hydrated conditions.* [**2**]

	Surface energy (J/m^2)		
Surface phase	Dry	Wet	Adsorption energy (eV/molecule)
P-Nb_2O_5	0.98	0.49	-2.1
B-Nb_2O_5	1.2	0.93	-0.92
B-Ta_2O_5	1.3	1.0	-1.2

*The adsorption energy per water molecule for the wet surface conditions are included.

for nucleating a terrace (ΔE) is:

$$\Delta E = \frac{2}{3}\pi R^3 \Delta\mu + 2\pi R^2 \gamma \qquad \text{(2.3 revisited)}$$

The nucleation activation energy at the critical nucleus size is therefore:

$$\Delta E = \frac{8\pi\gamma^3}{3\Delta\mu^2} \qquad \text{(2.4 revisited)}$$

This energy quantity can be used to calculate the the terrace nucleation rate according to the following equation:

$$N_R = f_0 \exp \frac{\Delta E}{k_B T} \qquad \text{(2.5 revisited)}$$

Based upon this analysis, the effect of E_{surf} on N_R can be clearly delinated. An increase in E_{surf} causes an increase to the required ΔE for terrace nucleation, thereby decreasing the rate of nucleation. A smaller surface energy has the opposite effect and causes the rate N_R to increase.

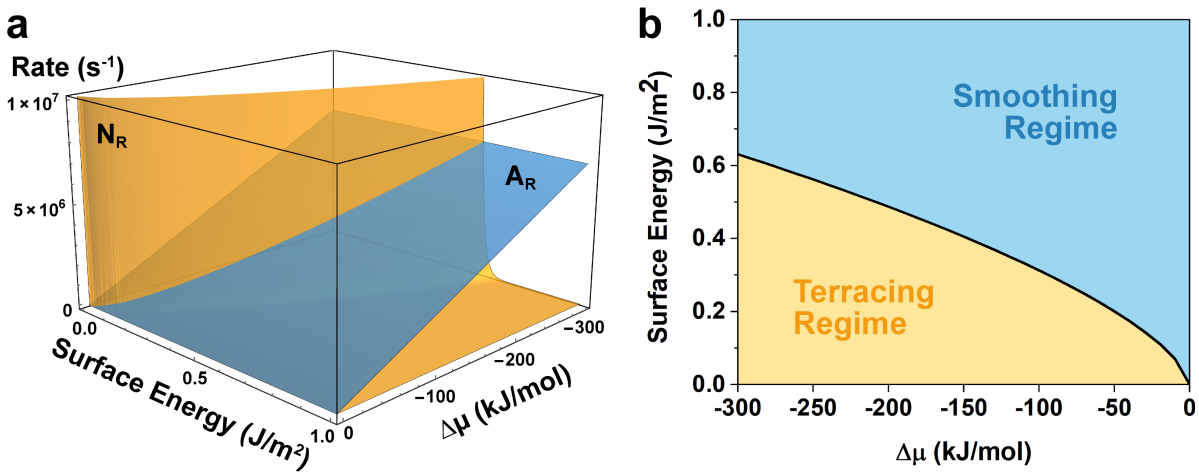

Figure 4.6. (a) Rates of terrace nucleation (yellow) and terrace annihilation (blue) plotted as functions of both surface energy and chemical potential. (b) Plot illustrating the dependence of the terracing (yellow) and smoothing (blue) growth regimes on the $\Delta\mu$ of the system and the surface energy of the nanoparticle. The terracing regime is defined where the terrace annihilation rate dominates at low surface energy and high chemical potential driving force. In contrast, the smoothing regime is defined for where the surface energy is high and driving force low, so terrace annihilation is the dominant growth process. [**2**]

The DFT calculations showed that the P-Nb_2O_5 surface phase had a lower surface energy than the Ta-rich surface phase (B-Ta_2O_5), and that this energy was further reduced by water chemisorption. Therefore, the lower surface energy increased the rate of terrace nucleation, resulting in the observed rough surface morphology. This is mathematically demonstrated in Figure 4.6a, where the terrace nucleation rate and terrace annihilation rate (A_R) are plotted as functions of $\Delta\mu$ and surface energy. (For more information about A_R, please refer to Chapter 3.) The terracing and smoothing regimes are defined in Figure 4.6b where the rate of either terrace nucleation or terrace annihilation dominate, respectively. The surface energy and $\Delta\mu$ are competing factors in a nanoparticle growth environment that control which growth behavior the NPs will exhibit.

The results presented show that not only do the surface phase and composition play a role in the growth of NPs but also how chemisorption and surface energy can affect the growth morphology of NPs. The role of hydroxyl groups on the synthesis and properties of KNO and KTO NPs have been studied previously; [**38**–**40**, **62**] however, the effect of hydroxyl groups on the surface has not been as extensively explored. In the case explored in this chapter, the chemisorption of water had little effect on the Ta-rich surfaces but had a significant role in decreasing the surface energy of the Nb-rich surfaces. These surfaces are experimental examples of how reduced surface energies can push the growth behavior into the terracing regime, resulting in chemisorption-driven surface roughening.

4.4. Conclusions

In this chapter, we presented an energetic and kinetic argument using the combined results of HRTEM images, multislice simulations, and DFT calculations to explain the morphological differences between hydrothermally synthesized KNO, KTO, and KTN NPs. The surface morphology was correlated with composition such that Nb-rich surfaces had terraced and rough surfaces whereas Ta-rich surfaces had smooth facets. We have shown that the Nb-rich surfaces of KNO and KTN-1 were terminated with a lower surface energy phase (P-Nb_2O_5) rather than the analogous niobium phase (B-Nb_2O_5) to that which terminates the KTO surface (B-Ta_2O_5). DFT calculations used to compare the surface energies of the two surface phases additionally demonstrated the surface stabilizing effect of water chemisorption on the P-Nb_2O_5 terminated surfaces.

Classical crystal growth models were used to rationalize the effects of these energetic quantities on the kinetics of growth. Mathematical models of the terrace nucleation

growth process demonstrated that lowering the surface energy decreases the activation energy for terrace nucleation, therefore increasing the rate of terrace nucleation and promoting the growth of a rougher surface morphology, as observed on the KNO and KTN-1 samples. These results are a demonstration of how different surface properties, including composition, phase, and chemistry, play significant roles in the synthesis and growth of nanoparticles.

CHAPTER 5

Complex Fluorine Chemical Potential Effects on the Shape and Compositional Heterogeneity of $KTa_{1-x}Nb_xO_3$ Nanoparticles

5.1. Introduction

One type of shape that can form under kinetic conditions is the kinetic Wulff shape, and it is determined by the growth rates of different crystallographic surfaces rather than their surface energies. [**33**] Unlike the thermodynamic Wulff shape, [**33**] which is the lowest energy shape a crystal will form under equilibrium conditions and only varies with surface energy and volume, many different kinetic Wulff shapes can take form for the same material in kinetically controlled systems. As explored in previous chapters, changes to the solution, surface effects, and other factors are capable of influencing the rates of different growth mechanisms. Another source of kinetic enhancement or abatement is the presence of defects in the bulk, which is the last unexplored important region for solution-based nanoparticle growth described in Chapter 1. Defects such as stacking faults and twin boundaries can enhance growth in particular directions, and this phenomenon has been observed in nanoparticles of many different material systems. [**14**, **94**–**98**]

In this chapter, we investigate this type of growth behavior by introducing potassium fluoride (KF) into the hydrothermal synthesis of KTN and KTO particles. KF was added to the aqueous hydrothermal solution for several reasons. It can act as another mineralizer and change the relative solution stabilities of the reagents during reaction, and it can also

act as a driving force behind the formation of bulk planar defects in the product. The supersaturation ($\Delta\mu$) of the system is sensitive to the extent and stability of precursor solubilization as well, so this influence on their relative reaction rates extends to the composition of the products grown.

The more complex results caused by the addition of KF were modeled using thermodynamic formation energy calculations performed with density functional theory to account for the increase in $\Delta\mu$ as well as the potential incorporation of KF into the material. These calculations confirmed that the experimental conditions were sufficient for forming Ruddlesden-Popper-like planar bulk defects in the particles. These defects promoted the formation of a defect enhanced kinetic Wulff shape by breaking the cubic symmetry of the perovskite structure and accelerating growth according to the geometry of the defect, resulting in anisotropic rectangular flakes.

The work presented in this chapter was done in collaboration with Jianguo Wen, who performed HRTEM on the samples.

5.2. Methods

All of the NP samples were grown following the hydrothermal synthesis described in previous chapters adapted from Goh et al., [**38**] where 0.0025 mol M_2O_5 (M = Ta and/or Nb), 25 mL 15 M KOH and different amounts of KF were added to a 125 mL Teflon-lined autoclave, heated to 200 °C for 1–12 hr. The molar ratio KF/KOH was varied between 0.15 and 0.35. The solution was stirred well for at least 30 min before hydrothermal treatment to ensure all of the precursors were well mixed.

Powder XRD was performed on a Rigaku Ultima diffractometer and Smartlab 3 kW Gen2 both operated at 40 kV and 44 mA, and the diffraction patterns were used to fingerprint the phases yielded in each synthesis. Electron microscopy was performed using a Hitatchi HD-2300 STEM, FEI Talos F200X TEM/STEM, and the ACAT. The MacTempasX software package was used to simulate HRTEM images with the multislice method. [**46**, **47**, **66**]

X-ray photoelectron spectroscopy (XPS) was performed on an ESCALAB 250Xi with an Al K_α source, and spectra were acquired with a spot size of 500 mum averaged over 5–20 scans.

Density functional theory calculations were performed with WIEN2k [**55**, **56**] with the PBEsol functional. [**54**] The R_{mt} were set to 2.26, 1.8, 1.72, 1.56, and 1.63 for K, Ta, Nb, O, and F, respectively, and the $R_{mt}K_{max}$ was set to 7. k-point meshes of 7 × 7 × 7 and 9 × 9 ×9 were used for the perovskite and KF structures, respectively. For the Ruddlesden-Popper defect structures, the k-point mesh was set to 8 × 8 × 8 ($n = 1$ and 2) and 7 × 7 × 1 ($n = 3$).

5.3. Results

A series of KTN NPs were synthesized with increasing concentrations of KF, and different effects were identified at low and high KF/KOH ratios. The effects changed properties ranging between the composition, morphology, and microstructure of the particles. In this section, the effects at low KF concentrations will be presented first to show the influence of KF on the reaction kinetics to forming the products. Then, the high KF concentration effects will be explored through additional experiments with and theoretical

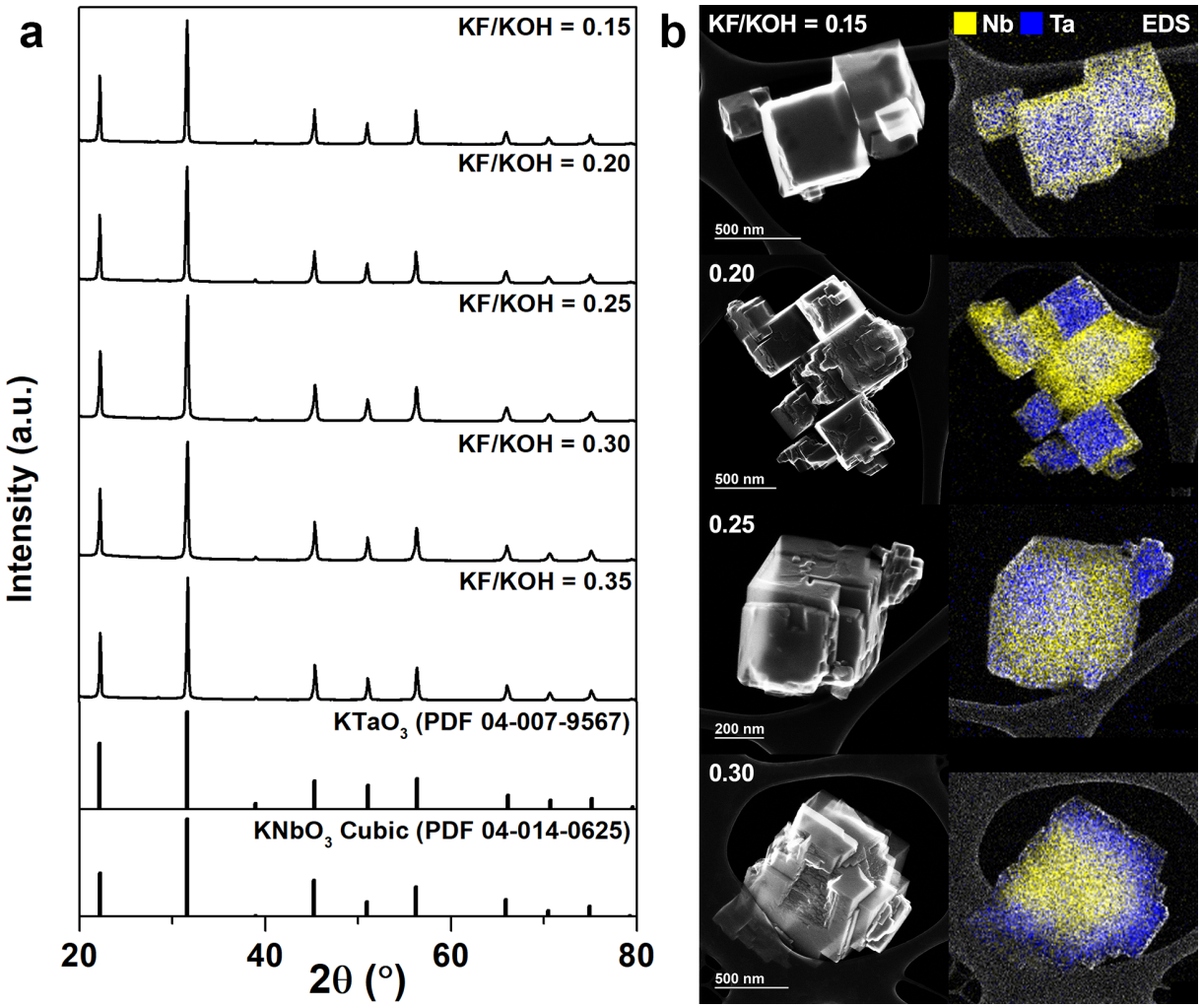

Figure 5.1. (a) Powder XRD patterns of the KTN particles synthesized with KF/KOH = 0.15–0.35. All samples matched well to the perovskite phases of KTO (PDF 04-007-9567) and KNO (PDF 04-014-0625). (b) SE images of nanocuboidal KTN particles synthesized with KF/KOH = 0.15–0.30. Corresponding maps show different distributions of niobium (yellow) and tantalum (blue) throughout the particle as KF/KOH increased. [**3**]

calculations of KTO synthesized with KF to determine how fluoride ions interact with the precursors during growth.

XRD patterns shown in Figure 5.1a confirm the formation of the perovskite phase in each synthesis. SE images of the samples in Figure 5.1b show that the particles

were mostly cuboidal in shape, and corresponding EDS maps show the distributions of niobium (yellow) and tantalum (blue) were not homogeneous across all the samples. When KF/KOH < 0.25, the particles had a tantalum-rich interior and niobium-rich surface. Higher concentrations of KF caused the composition to invert; the interior became niobium-rich and the surface became tantalum-rich. This resembles the composition trend observed in Chapter 4 when two different approaches were used to synthesize KTN, and this composition inversion confirms that the reaction rate between KOH and the niobium and tantalum oxide precursors to form the product KTN could be affected by a critical concentration of KF.

Significant morphology changes corresponding to increasing KF/KOH were also observed. The nanocuboids in Figure 5.1b were typical of the particles grown when KF/KOH < 0.25. Furthermore, the characteristic smooth and terraced morphologies of the tantalum-rich and niobium-rich surfaces, respectively, matched the composition-dependent growth behavior studied in Chapter 4. The most significant effect of adding KF to the synthesis was observed when KF/KOH > 0.20, where anisotropically shaped particles also formed. In contrast to the nanocuboids, these particles were flat rectangular flakes on the order of several hundred nanometers wide and $\sim$100 nm thick, and EDS maps of these particles did not show any significant composition segregation between niobium and tantalum (Figure 5.2). While the formation of geometrically anisotropic KTN particles would not be unusual for the material because KNO is polymorphic, KTO is an incipient ferroelectric that remains cubic at low temperatures. Anisotropic rod-like KNO particles, commonly of the tetragonal and orthorhombic KNO phases, have been produced with hydrothermal synthesis. [**40**, **99**]

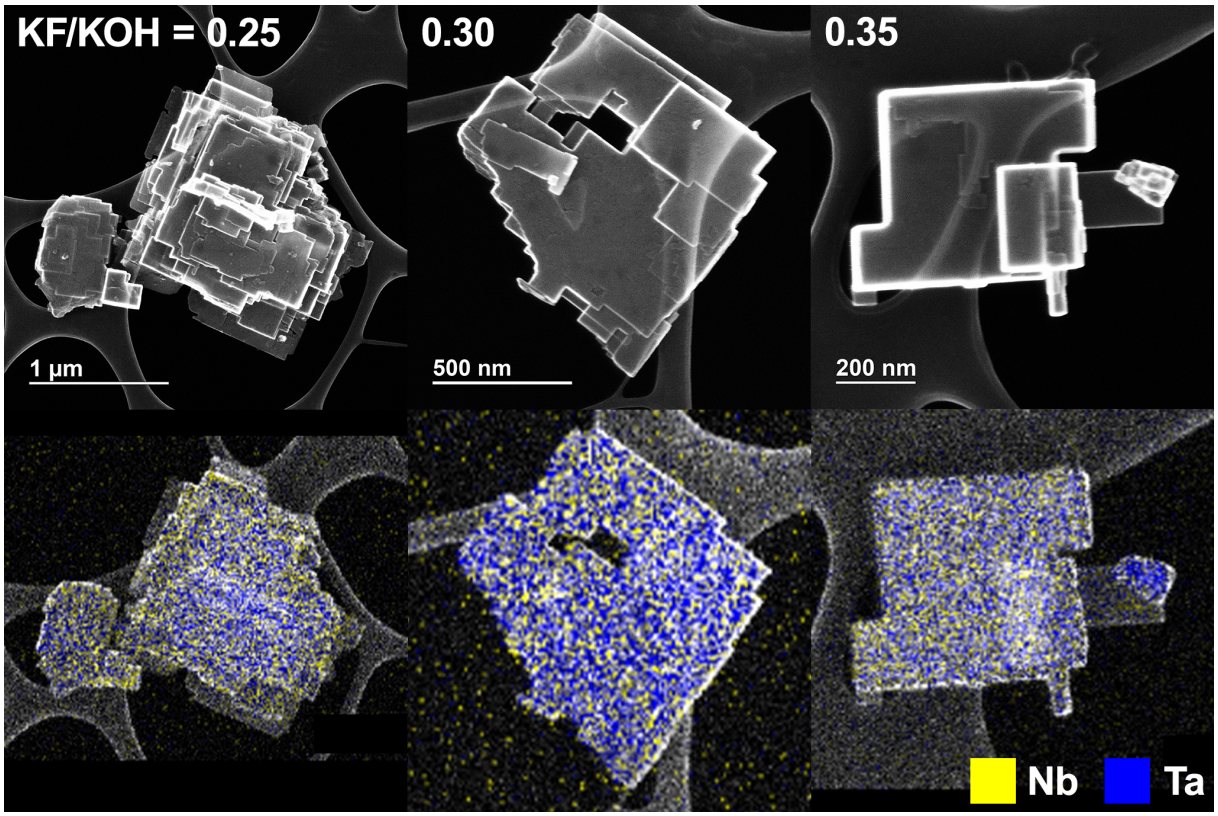

Figure 5.2. (top) SE images of KTN particles synthesized with KF/KOH = 0.25–0.35. Particles exhibit rectangular flake geometries ∼ 100 nm thick. (bottom) Corresponding EDS maps of images above where niobium is yellow and tantalum is blue. [**3**]

This result would be unexpected in KTO as a cubic material and implies a breaking of the cubic symmetry. To investigate further, KTO was synthesized with two KF/KOH ratios (0.20 and 0.30) below and above the concentrations where composition inversion in the nanocuboidal KTN samples occurred. Two different reaction times were used in each case: a shortened time period (1 hr) to capture the nucleation morphology after the nucleation incubation period and a longer time period (2–12 hr) to compare the particle morphologies after growth. It should be noted that 2 hr was selected as a longer time period for the KF/KOH = 0.20 sample because previous studies on KTO particles showed

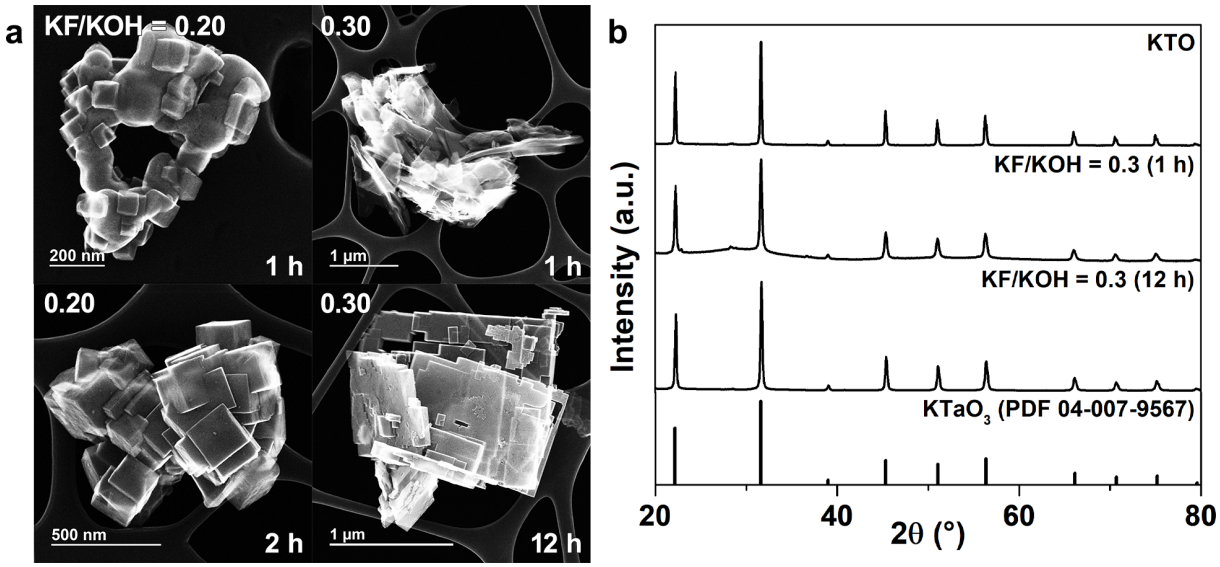

Figure 5.3. (a) SE images of KTO synthesized with different KF/KOH ratios after different reaction times. When KF/KOH = 0.2 (left column), particles were nucleated with cuboidal morphology (1 hr) and subsequently continued to grow into larger nanocuboids (2 hr). When KF/KOH = 0.3 (right column), particles nucleated with irregular flake morphologies (1 hr) and grew into large rectangular flakes (12 hr). (b) XRD patterns of KTO synthesized with KF/KOH = 0 for 4 hr and KF/KOH = 0.30 for 1 and 12 hr. All samples matched the KTO perovskite phase (PDF 04-007-9567). [**3**]

that the hydrothermal synthesis is almost complete after 2 hr (Chapter 3). As shown in Figure 5.3a, the morphologies of the particles after both nucleation and growth differed greatly between the two KF/KOH conditions. When KF/KOH = 0.20, the cuboidal morphology persisted after nucleation (1 hr) and growth (2 hr) as expected. Conversely, when KF/KOH = 0.3, the particles nucleated as irregular flakes (1 hr) that subsequently grew into large rectangular flakes (12 hr). XRD patterns of the two samples grown with KF/KOH = 0.30 and a standard KTO sample synthesized with no KF are compared in Figure 5.3b. They confirm that the cubic perovskite KTO phase (PDF 04-007-9567) was formed in all cases. The broad amorphous peak at 30° in the 1 hr sample XRD pattern

indicated that not all of the tantalum oxide precursor was reacted, suggesting a slowed reaction rate.

Since the structure remains cubic, another mechanism was responsible for the change in morphology. As mentioned in Section 5.1, bulk defects can lead to enhanced growth in certain directions, i.e. defect-enhanced kinetic Wulff shapes. To explore this further, the microstructure of the KTO rectangular flakes were characterized with TEM to identify defects that could cause this growth behavior. Figure 5.4a shows a BF image of a particle oriented on the [113] zone, and the high contrast indicates that the particles were highly strained. Significant strain agrees with the fact that the particles were not grown under conditions close to thermodynamic equilibrium. The HRTEM image in Figure 5.4b shows

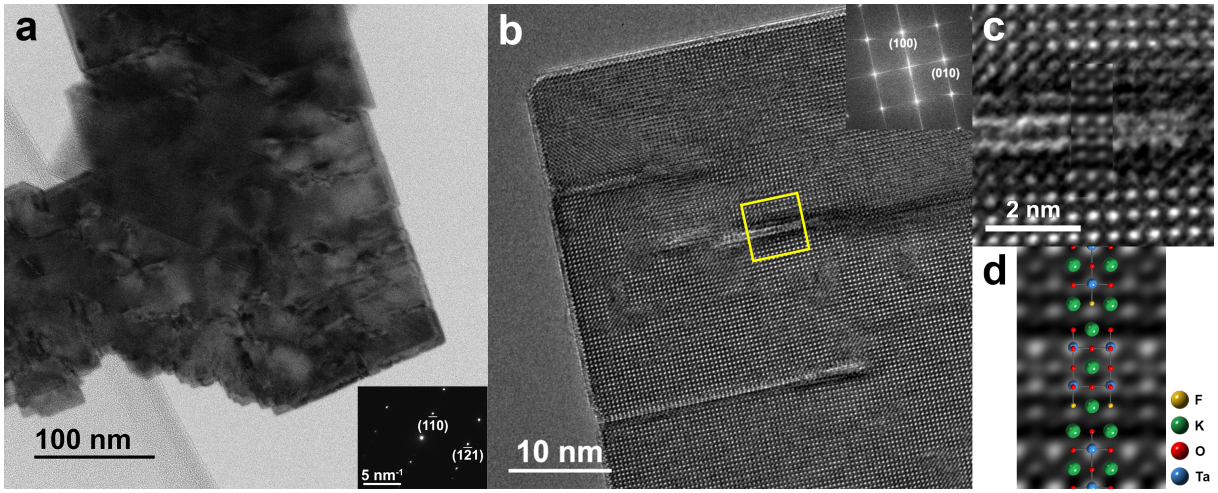

Figure 5.4. (a) BF image of the KTO particle on the [113] zone axis. Particle shows strain contrast arising from planar defects. (b) HRTEM image and corresponding FFT of the KTO particle on the [001] zone axis with several defects. The defect outlined by the yellow box is enlarged in (c), showing contrast matching a RP-like planar defect. A multislice HRTEM image simulation of the defect structure is inset. (d) Image simulation with a RP-like unit cell ($n = 2$) superimposed. Yellow atoms are F, green atoms are K, red atoms are O, and blue atoms are Ta. [**3**]

a particle oriented along the [001] zone. When imaged along this zone, most of the contrast is localized around defects, implying that the defects had planar geometries oriented along the {001} planes. One of the defects, highlighted by a yellow rectangle, is enlarged in Figure 5.4c. This defect shows misalignment of the lattice planes and contrast characteristic of a Ruddlesden-Popper-like shift between perovskite layers. A multislice HRTEM image of a defect Ruddlesden-Popper-like structure is inset into the image in Figure 5.4c and enlarged in Figure 5.4d where the unit cell is superimposed as well.

The Ruddlesden-Popper (RP) phase is a structure with interwoven layers of perovskite-like slabs with the general formula $A_{n+1}B_nX_{3n+1}$. Anion substitution for oxygen with fluorine is common in oxides, [**100**–**102**] and RP-like layer defects have been experimentally observed in ABO_3 perovskite oxides. [**103**–**106**] XPS was used to confirm the incorporation of fluorine into the oxide. The spectra of three samples (KTO-KF, KTN-KF-Nb_{surf}, and KTN-KF-Ta_{surf}) synthesized with KF were compared against three control samples with the same bulk and surface compositions (KTO-KF, KTN-Nb_{surf}, and KTN-Ta_{surf}). The KTO-KF, KTN-KF-Nb_{surf}, and KTN-KF-Ta_{surf} samples were synthesized with KF/KOH ratios of 0.2, 0.05, and 0.25, respectively. F 1s spectra for the samples synthesized with KF (black line) are plotted against their respective control samples (grey fill) in Figure 5.5. The background has been subtracted in each spectrum, and the spectra were all normalized to the B-site (Ta and Nb) peak integrated intensity for comparison. Higher KF/KOH ratios corresponded to higher peak intensities in the F 1s spectra. The spectra were quantified to determine the minimum and maximum F incorporation of the

samples, and the control samples were also quantified for a baseline F signal. The quantification results (Table 5.1) show that some F is incorporated into the synthesized material and that the amount scales with the concentration of KF used during synthesis.

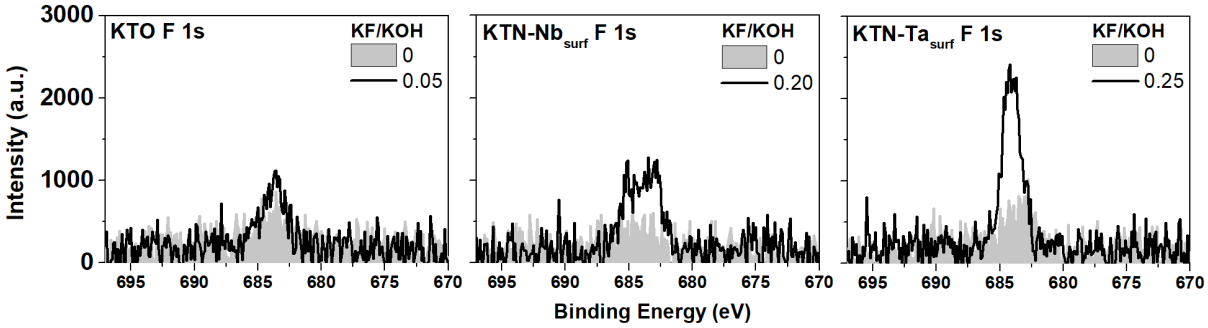

Figure 5.5. F 1s XPS spectra of KTO, KTN-Nb$_{surf}$, and KTN-Ta$_{surf}$. The spectra of the samples synthesized with KF are plotted with a black line, and the control; samples are plotted with grey fill. [**3**]

Table 5.1. XPS quantification results. [**3**]

Sample	KTO-Nb$_{surf}$		KTO	KTN-Ta$_{surf}$	
KF/KOH / Element	0	0.05	0.2	0	0.25
K	19.6	21.1	20.4	20.6	21.0
Ta	3.4	4.1	13.3	7.9	6.8
Nb	14.2	11.1	–	7.4	9.2
O	54.0	54.6	58.3	56.9	57.3
F	**0.4**	**0.3**	**0.6**	**0.2**	**0.8**
C	8.4	8.8	7.4	7.1	5.0

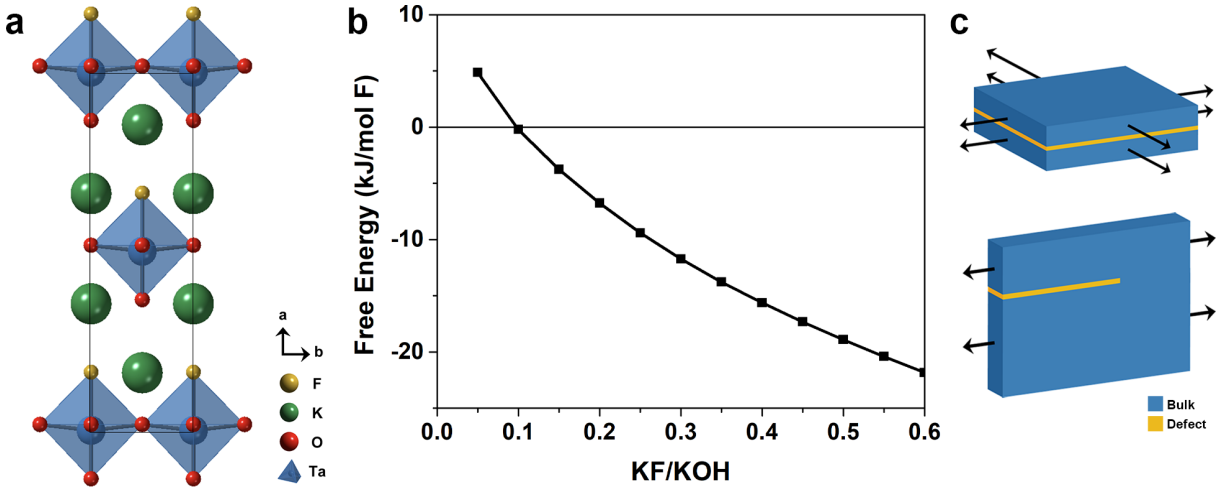

Figure 5.6. (a) RP-like $K_{n+1}Ta_nO_{3n}F$ ($n = 1$) unit cell used for DFT calculations. Yellow atoms are F, green atoms are K, red atoms are O, and blue octahedra are Ta. (b) $\Delta G_{\text{total}}(n = 1\text{–}3)$ normalized per mol F calculated for different KF/KOH. When normalized, $\Delta G_{\text{total}}(n = 1\text{–}3)$ all fall on the same line where the free energy is negative when KF/KOH > 0.10. (c) Schematics of accelerated growth directions in the presence of planar defects (yellow). [**3**]

DFT calculations were used in combination with experimental thermodynamic quantities to calculate the formation energy of an RP-like $K_{n+1}Ta_nO_{3n}F$ ($n = 1$–3) defect phase and assess its feasibility under the experimental synthesis conditions. The relaxed crystal structure of the lowest energy RP-like unit cell for $n = 1$ is shown in Figure 5.6a with (KF:KO) RP-like rock salt interwoven layers sandwiched between perovskite slabs. The following reaction equation was considered to compare the relative formation energy of $K_{n+1}Ta_nO_{3n}F$ versus that of the KTO:

$$n\text{KTaO}_3 + \text{KF} \rightleftharpoons \text{K}_{n+1}\text{Ta}_n\text{O}_{3n}\text{F} \tag{5.1}$$

The total free energy change (ΔG_{total}) was calculated as:

$$\Delta G_{\text{total}} = \Delta G_{\text{reaction}} - \Delta \mu_{\text{KF}} \tag{5.2}$$

where $\Delta G_{\text{reaction}}$ is normalized per mol F to compare the relative formation energies for $n = 1$–3:

$$\Delta G_{\text{reaction}} = \frac{1}{5n+2}\left(\Delta G_{\text{K}_{n+1}\text{Ta}_n\text{O}_{3n}\text{F}} - n\Delta G_{\text{KTaO}_3} - \Delta G_{\text{KF}}\right) \tag{5.3}$$

where $\Delta G_{\text{K}_{n+1}\text{Ta}_n\text{O}_{3n}\text{F}}$ is the Gibbs free energy of the RP-like defect material, ΔG_{KTO} is the Gibbs free energy of the bulk KTO, and ΔG_{KF} is the Gibbs free energy of KF. $\Delta \mu_{\text{KF}}$ is defined as:

$$\Delta \mu_{\text{KF}} = 2RT \ln\left(m\gamma\left(m\right)\right) \tag{5.4}$$

where R is the gas constant, T is the temperature, m is the molality of KF in the aqueous solution, and $\gamma(m)$ is the mean ionic activity coefficient for KF, which varies with the concentration. [**107**] Equation 5.3 was calculated with DFT, and Equation 5.4 was calculated using literature tables. [**108**, **109**] The total free energy change of the reaction is plotted in Figure 5.6b at different KF/KOH molar ratios, and demonstrates that when KF/KOH > 0.10, $\text{K}_{n+1}\text{Ta}_n\text{O}_{3n}\text{F}$ may form. Enhanced growth due to these defects, such as the examples drawn in Figure 5.6c, is the source of the symmetry breaking and anisotropic growth.

5.4. Discussion

In comparison to the change in shape observed at high KF/KOH ratios, the cause of the more subtle composition effects at lower KF/KOH ratios is more clearly isolated

to solution effects. The difference in rates of perovskite formation from the chemical reactions between KOH and Nb_2O_5 versus KOH and Ta_2O_5 were studied in Chapter 4. It was shown that Nb_2O_5 reacted more slowly compared to Ta_2O_5; however, Nb_2O_5 could react first if it was dissolved in a basic KOH solution before synthesis. Moreover, the same dissolution procedure could not be replicated with Ta_2O_5. The inverted Ta-Nb composition gradient effect of the pre-synthesis dissolution procedure was mirrored here by the addition of high concentrations of KF (Figure 5.1), implying that KF, or more specifically the fluoride, similarly affected the dissolution of the oxides in solution. The solubility of niobium oxides and relative insolubility of tantalum oxides have been studied in the literature, commonly using the Lindqvist ion ($M_6O_{19}^{8-}$, M = metal) and its different types of oxygen sites (i.e. bridging and terminal) as models for explaining the metal oxide dissolution behavior. [**87**, **110**–**113**] Protonation is an important step toward oxide dissolution; the more basic bridging oxygen site in $Nb_6O_{19}^{8-}$ increases its proton affinity, while the more basic oxygen site in $Ta_6O_{19}^{8-}$ is a terminal site, which is a less stable protonation site. [**110**]

Substitution of oxygen atoms with fluorine can change these properties. A study of tantalum fluoride complexes showed that most of these complexes are composed of bridging oxygen atoms and terminal fluorine atoms. [**114**] The terminal oxygen sites were determinant in the solubility of tantalum oxide, so if the terminal oxygen is substituted with fluorine, which has a higher proton affinity than oxygen, then the stability of the protonation site can increase. Increased protonation stability increases the solubility of the oxide and thereby increases the stability of the dissolved species in solution. A more stable species in solution is less energetically favored to react, which can explain the observations

of composition in the KTN particles synthesized in this study. Increasing concentrations of fluoride ions in solution increases the stability of the tantalum species in solution and decreases its reactivity, therefore also decreasing its reaction rate. The reaction rate was slowed enough at high enough KF concentrations such that the composition distribution of niobium and tantalum invert because the rate of reaction of the niobium species was faster.

The formation mechanism of the KTN and KTO rectangular flakes is related to the changes in growth kinetics driven by the chemical potential of KF in solution. DFT and thermodynamic calculations demonstrated that when KF/KOH > 0.10, an RP-like oxide structurally similar to a planar defect could be formed through the incorporation of fluorine into the particles. If a planar defect forms in a crystal, it can kinetically enhance the growth of a particle adjacent to the defect. The driving force of formation is increased by higher KF concentrations, and experimentally the rectangular flakes were produced when KF/KOH > 0.20. Kinetically enhanced growth at twins and stacking faults has been characterized in the literature in many nanoparticle materials, and in some cases resulted in a variety of plate-like particles. [**14**, **94**–**98**, **115**] Growth is enhanced at those sites because of more favorable local coordination of atoms along the plane of planar defects.

The TEM images in Figure 5.4 showed the structural characteristics of the planar defects. In general, the RP-like defects formed aligned to the {001} faces of the particles and accelerated growth along the plane of the defect. This directional kinetic enhancement resulted in the rectangular flakes imaged in this study. In addition, the varying defect sizes and contrast shown in Figure 5.4 indicated that the defects were relatively nonuniform

and often not simple single plane defects. Variations in the excess fluorine incorporated in the material can affect the size and structure of the detects. For example, the defect highlighted and simulated in Figure 5.4c structurally matched an RP-like defect with $n = 2$, but the formation of the RP-like $K_{n+1}Ta_nO_{3n}F$ oxide defect with $n = 1$ or 3 (or even $n > 3$) is also equally energetically likely based upon the formation energies shown in Figure 5.6. It is also important to note that in addition to the rectangular flakes, nanocuboids were grown in all samples even in solutions with high KF/KOH. The variation in kinetic Wulff shapes suggests that these hydrothermal syntheses had mixed growth control between different kinetic conditions, and that continuing variations in $\Delta\mu_{KF}$ as the reaction progressed contributed to the variety of particle shapes and nonuniform defects formed.

5.5. Conclusions

In modeling nanoparticle synthesis, it is critical to understand the role of different experimental conditions on the kinetics of reactions and growth to understand and accurately predict outcomes. KF played several roles in the synthesis and growth of KTN and KTO particles in this chapter. In the solution, fluoride ions increased the solution stability of tantalum species and decreased its rate of reaction to forming the perovskite product. Because the Ta species reacted slower than the Nb species, this resulted in a composition gradient inversion in the KTN particles produced when KF/KOH > 0.20. As demonstrated experimentally and modeled thermodynamically, KF was also incorporated into the particles as RP-like planar defects. These planar defects accelerated anisotropic

growth and resulted in the formation of defect enhanced kinetic Wulff shaped particles characterized by their large, flat rectangular flake geometries.

CHAPTER 6

Controlled Two-Step Formation of Faceted Lanthanide Scandate ($LnScO_3$) Nanoparticles

6.1. Introduction

In this dissertation, we have analyzed and discussed nanoparticle growth processes, regimes, and their kinetics primarily through several case studies on the KTO, KNO, and KTN hydrothermal synthesis systems. We move on from the KTN materials in this chapter to demonstrate how these concepts can be applied to a different material system and synthesis method to improve shape and size control of the particles produced. The new materials of focus are the lanthanide scandates ($LnScO_3$) (Ln = La, Nd, Sm, and Gd), which are oxides that are garnering interesting in many fields. For example, they have been studied as dielectrics, [**116**, **117**] flexoelectrics, [**118**] and substrates. [**119**] The wide range of lattice parameters these materials can adopt by varying the lanthanide cation residing in the A-site makes them particularly appealing as substrate materials. [**119**] These materials are orthorhombic perovskites with space group *Pbnm*, and we will be describing them with the pseudo-cubic unit cell defined by the $\langle 110 \rangle$ and $\langle 001 \rangle$ directions of the orthorhombic unit cell.

This chapter describes the "hydro-sauna" synthesis method in which a humid environment is used to synthesize $LnScO_3$ particles in a water vapor-assisted sol-gel process. [**5**]

The original method was developed in an autoclave and was able to successfully synthesize crystalline $GdScO_3$ particles at temperatures as low as 300 °C. [**120**] However, the sealed environment limited the quantity of product that could be produced in a reaction, and the method was unable to yield well-faceted particles and instead grew irregularly shaped particles. The lack of shape-control made this system an appropriate candidate for testing whether the terracing and smoothing crystal growth regimes can be enhanced at different times during a synthesis to encourage the formation of smooth facets.

Both drawbacks of the original hydro-sauna synthesis are remedied here by switching to a tube furnace reaction system and using a two-step heating sequence. In this chapter, we describe how to identify the dominant growth processes based upon the reaction conditions used in a series of heating experiments. After a thermodynamic and chemical analysis of these results, a two-step heating sequence was developed to optimize the appropriate growth process in each segment. The first step in the heating sequence provides the appropriate thermodynamic conditions to nucleate the desired oxide phase, and the second step encourages step-flow growth to smooth the particle surfaces and form well-faceted particles.

The work presented in this chapter was accomplished in collaboration with Ryan Paull, who performed the syntheses and XRD, and Zachary Mansley, who performed the microscopy. [**5**]

6.2. Methods

The synthesis of $LnScO_3$ particles was accomplished through the decomposition of a mixed cation hydroxide gel in a humid environment. The gel was made by first preparing

a rare-earth nitrate precursor by dissolving 4 mmol Ln_2O_5 and Sc_2O_3 in 20 mL 15.8 N nitric acid. The nitrate precursor was heated at 80 °C until all of the liquid evaporated, then it was dissolved in 20 mL deionized water. The mixed cation hydroxide gel was precipitated by adding the precursor dropwise into 50 mL 10 M NaOH solution. The gel was subsequently cleaned by repeated rinsing and centrifuging with deionized water. The gel was moved to an alumina boat placed in a tube furnace. A humid environment was created in the tube furnace by flowing argon gas through a bubbler filled with deionized water placed upstream.

Two heating sequences were used to study the growth behavior of the particles when subjected to different thermal environments. The first was a one-step heat treatment where the gel was reacted at a temperature between 200 °C and 450 °C for 2 days. Based upon the results of these heat treatments, two different temperatures were selected for the second heating sequence to optimize nucleation and growth. In the two-step heating sequence, the gel was first reacted at 450 °C for 2 days, then the temperature was reduced to 300 °C for 1 day.

Powder XRD was used to identify the phase(s) yielded after synthesis and performed on a Rigaku Ultima diffractometer equipped with a Cu K_α source operated at 40 kV and 44 mA. The morphology of the producs were characterized by SE imaging performed on a Hitachi HD-2300 STEM operated at 200 kV. The crystallographic features of the particles were characterized with HRTEM performed on a JEOL ARM300F GrandARM S/TEM operated at 300 kV.

6.3. Results

The results of two sets of experiments are presented in this section. The first set of experiments show the thermodynamic conditions of the synthesis system and the effect they have on the phase of the products as well as the kinetics of different growth processes. The second set of experiments utilize the results of the first experiments to develop an optimized synthetic approach to producing particles with improved size and shape control.

6.3.1. One-Step Reaction

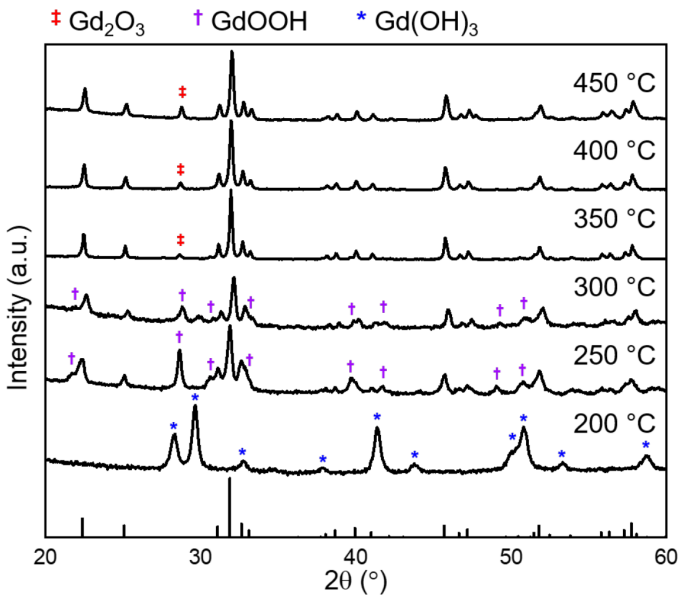

Figure 6.1. XRD patterns of products yielded from performing the $GdScO_3$ synthesis at different reaction temperatures 200–450 °C. The calculated pattern for perovskite $GdScO_3$ is plotted on the bottom, and the secondary phases are Gd_2O_3 (red double dagger‡), GdOOH (purple dagger†), and $Gd(OH)_3$ (blue asterisk*). At 200 °C, only $Gd(OH)_3$ was produced. Between 250–300 °C, $GdScO_3$ and GdOOH were yielded. For temperatures 350 °C and above, the primary product was $GdScO_3$ and the secondary project was a small amount of Gd_2O_3. [**5**]

The first set of experiments were performed using the $GdScO_3$ synthesis to characterize the dominant growth mechanisms at different reaction temperatures. Powder XRD patterns of the product after reacting at a temperature between 200 °C and 450 °C for 2 days are shown in Figure 6.1. There were three characteristic groups of products corresponding to the reaction temperature. At low temperatures (200 °C), the only product was $Gd(OH)_3$. A combination of $GdScO_3$ and GdOOH were formed at intermediate temperatures between 250 °C and 300 °C. At higher temperatures (350–450 °C), the product was composed of primarily $GdScO_3$ with a secondary phase of a small amount of Gd_2O_3. SE images of the higher temperature products are shown in Figure 6.2. The particles grown at 350 °C tended to have more well-defined facets and larger sizes in comparison to the particles grown at 450 °C. Small particulates of $GdScO_3$ were also present in several of the samples.

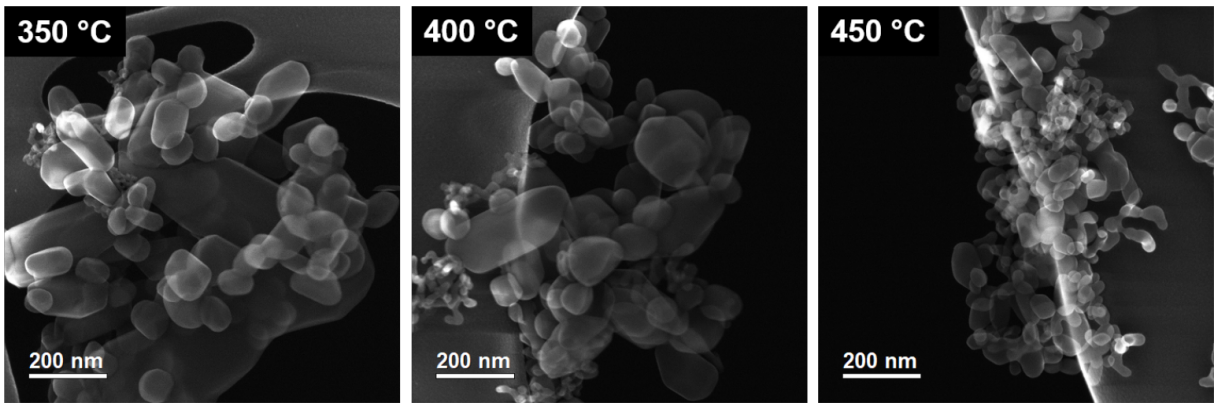

Figure 6.2. SE images of $GdScO_3$ synthesized at 350, 400, and 450 °C. The particles grown at 350 °C had a larger average size and well-defined facets compared to the particles grown at higher temperatures. Small particulates of $GdScO_3$ were present in some samples. [**5**]

6.3.2. Two-Step Reaction

Based upon the results from the one-step set of experiments, the reaction temperatures 450 °C and 300 °C were selected for the two-step heating sequence experiments. The four $LnScO_3$ (Ln = La, Nd, Sm, and Gd) oxides were all synthesized using this two-step heating sequence, and XRD patterns of the products are shown in Figure 6.3. The XRD patterns confirm that the primary phase in all four syntheses was $LnScO_3$, and there were trace amounts of secondary phases ($Ln(OH)_3$ and Ln_2O_3).

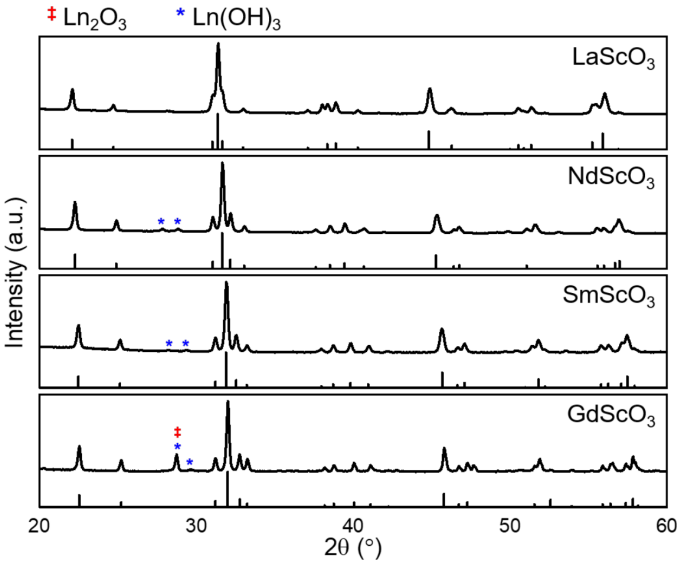

Figure 6.3. XRD patterns of $LnScO_3$ (Ln = La, Nd, Sm, and Gd) samples grown via the two-step heat treatment (450 °C for 2 days, then 300 °C for 1 day). The calculated patterns for each perovskite phase are shown on the bottom of each plot. The perovskite phase was the primary product in each case, and there were trace amounts of Ln_2O_3 (red double dagger‡) and/or $Ln(OH)_3$ (blue asterisk*) in the $NdScO_3$, $SmScO_3$, and $GdScO_3$ samples. [**5**]

Figure 6.4 shows SE images of the four oxide samples synthesized with the two-step reaction. The particles exhibit more well-defined and larger facets than the particles grown with a one-step heat treatment (Figure 6.2). The shapes of the particles were more

closely examined with HRTEM in Figure 6.5, where a $NdScO_3$ particle is imaged on the [001] pseudo-cubic zone axis. The whole particle is shown in Figure 6.5a, and the bottom right corner is enlarged in Figure 6.5b. The corresponding FFT of the whole particle shows that the particle surfaces primarily terminated with the {100}- and {110}-type pseudo-cubic surfaces (Figure 6.5c).

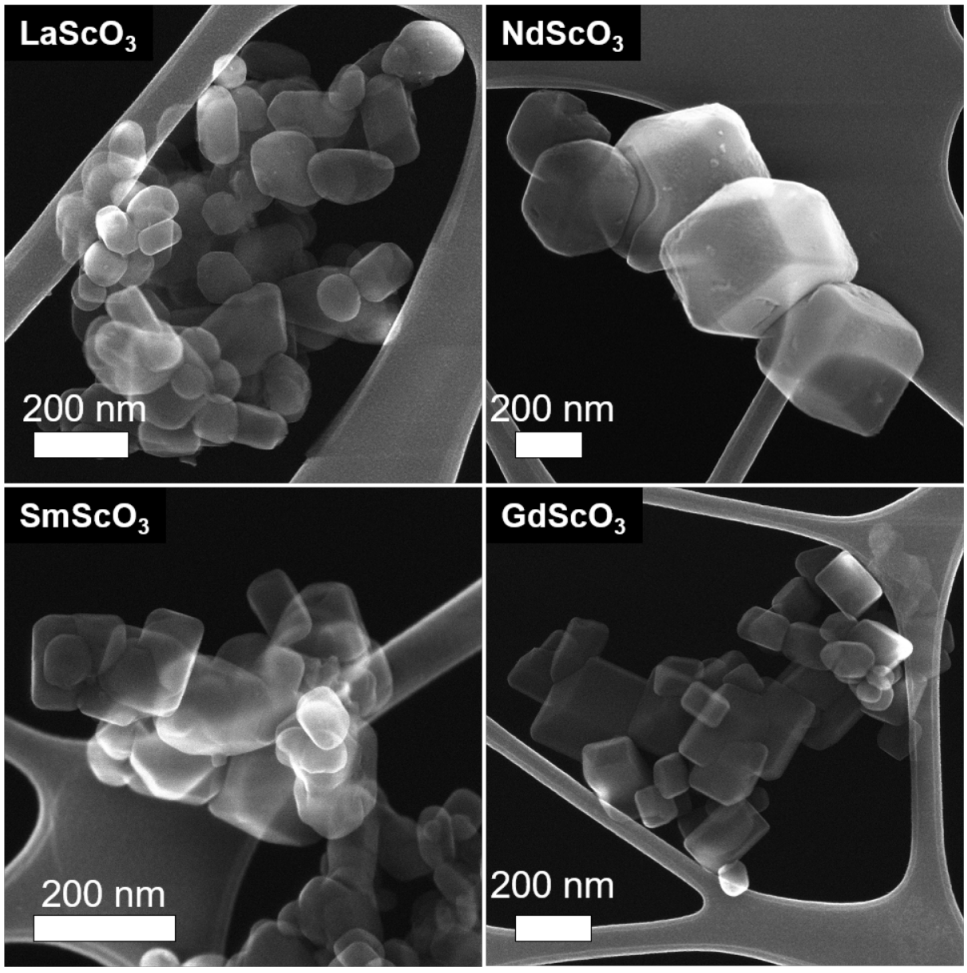

Figure 6.4. SE images of $LnScO_3$ (Ln = La, Nd, Sm, Gd) particles synthesized with the two-step heating sequence (450 °C for 2 days, then 300 °C for 1 day). The particles have well-defined facets and smooth surfaces. [**5**]

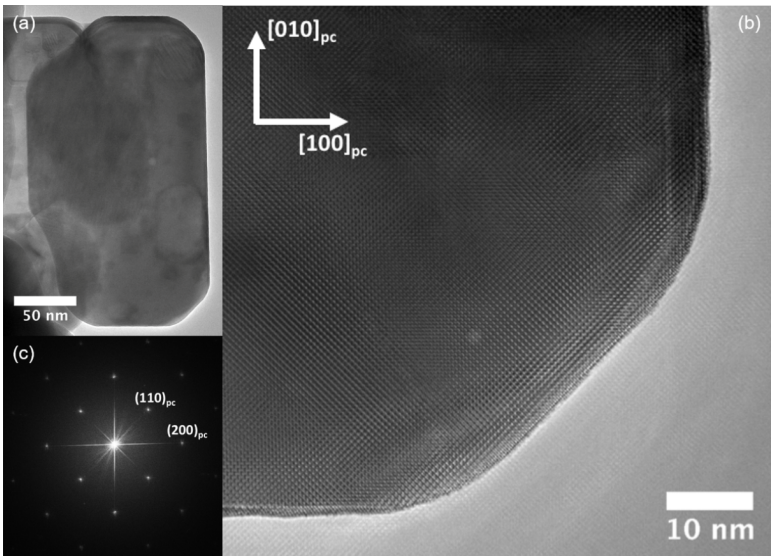

Figure 6.5. (a) HRTEM image of a $NdScO_3$ particle grown with the two-step heat sequence. (b) HRTEM image of the bottom right corner of the particle imaged in (a). (c) FFT of the entire $NdScO_3$ particle showing the surfaces were terminated with {100}- and {110}-type pseudo-cubic surfaces. [**5**]

6.4. Discussion

Water plays several roles in this hydro-sauna system. It was previously hypothesized in the initial development of the hydro-sauna method that the transformation of the mixed cation hydroxide gel into crystalline oxide was a vapor-assisted reaction. [**120**] Under dry conditions, there was limited mass transport and the gel matrix collapses under capillary forces from evaporating liquid during reaction. In contrast, humid conditions help preserve the gel matrix and assist in the diffusion of reactants through the gel such that the chemical reaction to form the perovskite product could proceed.

The second role of water is its control over the phase of the products produced through the competition between several dehydration and hydration chemical reactions. The two

competing chemical reactions are:

$$\mathrm{LnSc(OH)_6} \cdot x\ \mathrm{H_2O} \rightleftharpoons \mathrm{LnScO_3} + (x+3)\ \mathrm{H_2O} \tag{6.1}$$

$$\mathrm{LnSc(OH)_6} \cdot x\ \mathrm{H_2O} \rightleftharpoons \mathrm{Ln(OH)_3} + \mathrm{ScOOH} + (x+1)\ \mathrm{H_2O} \tag{6.2}$$

Equation 6.1 is responsible for forming the desired product ($\mathrm{LnScO_3}$), while Equation 6.2 yields undesired products, such as hydroxides, oxyhydroxides, or binary oxides. An equivalent way to represent the competition between these two reactions is:

$$\mathrm{Ln(OH)_3} + \mathrm{ScOOH} \rightleftharpoons \mathrm{LnScO_3} + \mathrm{H_2O} \tag{6.3}$$

The sign of the Gibbs free energy change of this reaction ($\Delta G_{\mathrm{reaction}}$) determines whether the forward or reverse reaction will proceed, and it is sensitive to the amount of water present in the system. When $\Delta G_{\mathrm{reaction}} < 0$, the forward reaction will proceed to yield the desired products ($\mathrm{LnScO_3}$ and water). When $\Delta G_{\mathrm{reaction}} > 0$, the undesired products (e.g. hydroxides, oxyhydroxides, and binary oxides) will form instead.

A simple analysis of this chemical reaction with Le Chatelier's principle clarifies the role of water and temperature in this system. When the concentration of water is increased in the system, the reverse reaction will be favored (i.e. $\Delta G_{\mathrm{reaction}}$ increases) to produce the undesired products. However, water is a necessary component of the hydrosauna environment, so another parameter must be changed to favor the forward reaction. Temperature can alternatively influence the thermodynamic relationship of water to the system. A higher temperature increases the vapor pressure of water, thus decreasing its chemical potential as a result of the greater entropic contribution of the water vapor.

Table 6.1. One-step $GdScO_3$ reaction temperature, products, and sign and estimated relative magnitude of $\Delta G_{\text{reaction}}$.

Temperature (°C)	Products	$\Delta G_{\text{reaction}}$
200	$Gd(OH)_3$	> 0
250–300	$GdScO_3$, GdOOH	< 0
350–450	$GdScO_3$, Gd_2O_3	$\ll 0$

The sign and relative magnitude of $\Delta G_{\text{reaction}}$ could be estimated for different reaction temperatures based on the products of the one-step single temperature experiments identified by XRD in Figure 6.1. These results are summarized in Table 6.1. At 200 °C, $\Delta G_{\text{reaction}}$ was positive and only produced the hydroxide. As temperature increased, $\Delta G_{\text{reaction}}$ became increasingly negative and produced the desired perovskite oxide. It should be noted that the secondary product phase is also dependent on temperature; GdOOH was formed at intermediate temperatures, and Gd_2O_3 was formed at the highest temperatures used. This was attributed to more significant dehydration of the secondary phase at higher temperatures because of the increased entropy of vapor phase water. It also indicates that the dehydration process from $Gd(OH)_3$ to GdOOH may be a necessary step for subsequent reaction to $GdScO_3$. This supports the hypothesis that the formation of LnOOH was a necessary step for the hydrothermal synthesis of $LnMnO_3$. [**121**] However, the formation of LnOOH was not observed in the syntheses of the other three perovskite oxides ($LaScO_3$, $NdScO_3$, and $SmScO_3$), where the only secondary phase identified was $Ln(OH)_3$. It is possible that LnOOH could rehydrate into $Ln(OH)_3$ upon cooling to room temperature, but further study is necessary.

Temperature also played a role in determining the shape and size of particles grown. The three relevant growth processes are: (1) particle nucleation from the gel, (2) terrace nucleation, and (3) terrace growth. The terrace nucleation and growth processes were explained and explored in more depth in Chapters 1 and 3. [**1**] All three processes can occur simultaneously, so it is the mechanism with the highest rate that will dominate and determine the final shape and size. The preferred growth processes at different temperatures can be inferred from the magnitude of the driving force $\Delta G_{\text{reaction}}$. The driving force is highest ($\Delta G_{\text{reaction}} \ll 0$) at high temperatures, and this results in high rates of both particle nucleation and terrace nucleation. With these dominant growth mechanisms, the particles produced tend to have small sizes and irregular shapes with less well-defined facets. A high rate of particle nucleation also increases the size monodispersity of the particles because most of them are nucleated at nearly the same time. This corresponds with the size, size distribution, and morphology of particles imaged at 450 °C in Figure 6.2. At lower temperatures the driving force decreases slightly ($\Delta G_{\text{reaction}} < 0$), so the rate of nucleation decreases such that the dominant growth process is terrace growth. When the rate of terrace growth is highest, the system enters the smoothing regime where particles can be formed with well-defined and smooth facets. Hence, the particles imaged of those grown at lower temperatures in Figure 6.2 have substantially more well-defined surface facets than those at higher temperatures. Another consequence of the decreased rate of nucleation is an increase in the size polydispersity of the particles because particles nucleated earlier during the reaction will have more time to grow than particles nucleated later, as illustrated by the small particulates present in the images.

The two-step heat sequence was designed to enhance the rates of different growth mechanisms at different time intervals during the synthesis to produce smaller and well-faceted particles. The first step in the sequence used a high temperature with a large driving force ($\Delta G_{\text{reaction}} \ll 0$) to nucleate many small particles of the $GdScO_3$ phase. The second step lowers the reaction temperature to decrease the driving force ($\Delta G_{\text{reaction}} < 0$) and nucleation rate, allowing terrace growth to take over as the dominant growth process and promote smoothing of the particle surfaces to produce well-defined facets and shapes. The temperatures 450 °C and 300 °C were selected for each step, respectively, based upon the one-step heat treatment results and observations. Images of the $LnScO_3$ particles synthesized with this two-step approach (Figure 6.4) confirmed that these conditions were successful in produce particles with smaller sizes and more facet control. The $GdScO_3$ particles in particular had more pronounced facets and cuboidal shapes in comparison to the irregular shapes and size polydispersity of $GdScO_3$ particles produced from the one-step approach (Figure 6.2). Additionally, the small particulates imaged in the one-step samples do not appear in the two-step samples, confirming that the nucleation rate was sufficiently suppressed in the second step. Increasing the temperature of the first heating step may further decrease the average size and improve monodispersity of the products.

$NdScO_3$, $SmScO_3$, and $GdScO_3$ all grew cuboidal shaped particles with the two-step heat treatment, and HRTEM characterization identified that they were primarily terminated with {100}-type pseudocubic surfaces and secondarily with additional {110}-type pseudocubic facets (Figure 6.5). In contrast, the $LaScO_3$ particles were less well-faceted and formed irregular polyhedrons. This suggests that the temperature range for the smoothing regime may be lower than experimentally tested. Reducing the temperature

of the second step and optimizing the time interval of each step may yield particles with improved shape control.

6.5. Conclusion

A two-step process for synthesizing $LnScO_3$ particles with improved size and shape control was developed. The temperatures used for each step in the heating sequence was determined based upon studying the effects of the reaction temperature on the rates of different growth processes and the phases of products produced. First a high temperature heat treatment was used to nucleate particles of the desired perovskite phase, then the temperature was lowered to reduce the rate of nucleation and allow the terrace growth process to grow smooth, flat facets. This approach was successful in growing well-faceted $LnScO_3$, most of which were cuboidal in shape.

CHAPTER 7

Is Oxide Hydrothermal Growth Crystal Growth?

7.1. Introduction

Among the numerous nanoparticle synthesis methods, hydrothermal synthesis remains a popular choice for many reasons. It has many practical advantages: hydrothermal synthesis can be performed under relatively mild conditions (∼100-300 °C), can produce highly crystalline products in a single step, and has decent shape and size control over the nanoparticle products. Reasonable control over the size and shape is especially important for using nanoparticles in different applications, where size or shape dependent properties can significantly affect the functional properties of nanoscale materials. [**14**, **30**] Therefore, hydrothermal synthesis has been successfully employed to produce many different simple and complex oxides, semiconductors, and other classes of materials in a variety of shapes and sizes, demonstrating its versatility and popularity among the nanoparticle research community. [**31**, **34**, **35**, **122**] Because of its prevalence, hydrothermal synthesis and recent developments of the method have been the subject of many reviews over the years. [**32**, **34**, **35**, **122**] Those reviews provide detailed information about the hydrothermal synthesis method, including important components and operating considerations, as well as accomplishments in producing many material classes and different results, and as such these topics will not be discussed herein.

While many hydrothermal "recipes" have been published, there has been less attention on the details of the growth processes. For example, what factors lead to desirable (e.g. faceted) versus undesirable (e.g. nonuniform) shapes? How does the synthesis environment affect the morphology or chemistry of the nanoparticle products? Details of growth processes are well-known for crystal growth at the macroscopic scale. Models such as the influential step flow growth theory developed by Burton, Cabrera, and Frank (BCF theory) described growth mechanisms at the surfaces of crystals and related growth rates to molecular processes. [**123**, **124**] Many of the early crystal growth models focused on growth from vapors, but the challenges of modeling crystal growth in solutions have also been the subject of studies, such as the early work conducted by Berg [**125**] and Bircumshaw. [**126**] These studies highlighted the importance of interactions between solute molecules in solution with the growing surface and kinetics of transport mechanisms in solution.

There are strong similarities between the factors that control macroscopic growth and that of nanoparticles. For instance, the thermodynamic Wulff construction is a quintessential model used to determine the equilibrium shape of crystals; however, this equilibrium shape is by definition only valid for crystals grown under thermodynamic equilibrium. [**33**] In many cases, including in many nanoparticle syntheses, growth is controlled by kinetics instead of thermodynamics, and indeed Wulff's original paper was based on conclusions from kinetic growth experiments. In those cases, the kinetic Wulff construction, which determines a crystal shape based upon growth velocities, is valid. Both the thermodynamic and kinetic Wulff constructions have been used to describe the shapes of nanoparticles grown using many different methods. [**12**, **13**, **94**, **115**]

To what extent is hydrothermal growth a manifestation of crystal growth models such as BCF and/or thermodynamic or kinetic Wulff theories? This is a question that has not been addressed in detail in existing papers or reviews, which primarily focus on reporting synthesis procedures or methods for growth. The goal of this Chapter is to discuss nanoparticle crystallization and growth during hydrothermal synthesis in the context of established macroscopic methods. In order to more clearly identify and differentiate these thermodynamic and kinetic effects on growth, this review will be organized as follows. We will begin with an overview of crystal growth theory defined for the more specific hydrothermal synthesis case. Under hydrothermal conditions, the system is closed, contained in a solution-based environment, and all inputs (e.g. reagents concentrations, temperature, time) are well-defined. Then, as important thermodynamic and kinetic considerations are defined, several relevant examples will be pulled from literature as illustrations of each concept.

7.2. Hydrothermal Crystal Growth Process

Hydrothermal synthesis has been reviewed in depth before, so only relevant details will be discussed briefly here. Typical hydrothermal synthesis procedures involve a reaction that occurs in water in a sealed vessel (autoclave) above the boiling point of water (100 °C), where it reaches an autogenous pressure. Water serves as both a solvent and transportation medium for the precursors, mineralizers, and other additives used in a synthesis. As a solvent, water hydrates or complexes precursors to form more reactive compounds for the chemical reaction. Mineralizers aid in the dissolution of precursors, and the choice of mineralizer, often basic or acidic compounds that alter the pH of the solution, significantly

impact the phase, sizes, and morphology of nanoparticles produced. Pourbaix diagrams, or Eh-pH diagrams, which map the thermodynamic equilibrium phases relative to its redox potential and pH, have been used to calculate stability diagrams guide the type and amount of mineralizer to use in a synthesis. [**127**–**129**] Many other additives have been used to great effect in hydrothermal syntheses, including organic compounds that act as surfactants and nonaqueous solutions that have many results (i.e. solvothermal synthesis). [**34**, **122**]

One of the major challenges in any growth, including hydrothermal growth is distinguishing between thermodynamic and different types of kinetic control; which one or ones are active plays a major role in determining the shapes of the products of hydrothermal syntheses. The detailed growth depends upon a number of different variables, both thermodynamic parameters and the kinetic rates. In this section, we will describe the basic processes of crystal growth beginning with initial homogeneous cluster nucleation to growth processes, such as terrace nucleation and growth on surfaces. The intent is not to provide a full review, rather to set the context for analyzing hydrothermal growth.

7.2.1. Initial Nucleation and Growth

Following mixing of the relevant solutions, solids will start to form. Depending upon the exact system there may be very small nuclei composed of four to ten atoms, or there may be an amorphous gel where nuclei are formed only when the temperature and therefore pressure are increased. [**130**] In some cases such as those containing surface active agents the nucleation probably occurs in the confined regions bounded by the lipid bilayers, see for instance Figure 7.1. [**6**, **7**, **29**, **131**] The driving force behind nucleation is supersaturation

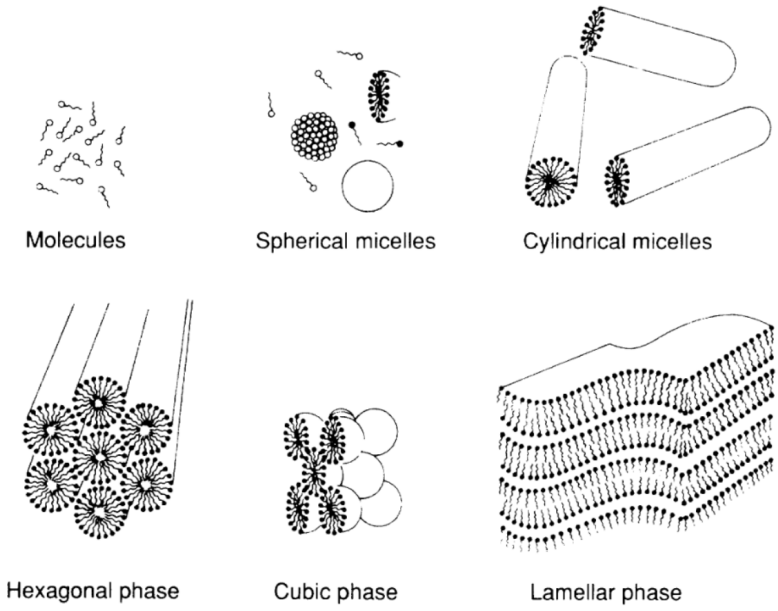

Figure 7.1. Surface active agents (surfactants) are typically amphiphilic molecules, meaning one end is hydrophobic and the other end is hydrophilic. This diagram shows different aggregation states of surfactants that can form depending on the concentration of the compound in solution, ranging from being arranged as micelles to lipid layers. The different geometries and surfactant chemistry limit nucleation to certain regions. Image reproduced from [**6**] based on [**7**].

of the solution defined via the chemical potential difference between the solution and thermodynamic equilibrium solution, i.e.:

$$\Delta\mu = \mu_{sat} - \mu_{eq} \tag{7.1}$$

where $\Delta\mu$ is the chemical potential difference between the chemical potential of the supersaturated solution (μ_{sat}), and the chemical potential of the equilibrium solution (μ_{eq}). Supersaturation also serves as a driving force for growth processes. A larger chemical potential difference increases the rates of both nucleation and growth processes. The rate of nucleation (N) depends on the probability of thermodynamic fluctuations with enough

energy for nucleating a new phase, i.e.:

$$N = f_0 \exp \frac{\Delta E}{k_B T} \tag{7.2}$$

where f_0 is a pre-exponent factor dependent on several factors such as the frequency of collisions between molecules and clusters and the density of molecules in solution and ΔE is the total energy change for nucleating the new phase. In order to determine the energy required for nucleation, the nuclei can be modeled as spheres, which minimize surface energy. In this case, the total free energy change of nucleation (ΔE) is:

$$\Delta E = \frac{4}{3}\pi R^3 \Delta G_V + 4\pi R^2 \gamma \tag{7.3}$$

where R is the radius of the nucleus, ΔG_V is the specific volume change in free energy of forming the new phase, and γ is the surface energy. Compared to the supersaturated solution, the nucleated phase is more stable, so the volume free energy change is negative. In contrast, the surface energy term is positive. The difference in the third and second order dependence indicates that there is a maximum in the free energy change dependence with nucleus radius size. Nuclei with radii larger than a critical radius (R^*) are more likely to survive and continue growing into larger crystals. Clusters smaller than this critical radius will dissociate back into the solution. R^* can be calculated from by determining the maximum in Equation 7.3:

$$\Delta E(R = R^*) = \frac{16\pi\gamma^3}{3\Delta G_V} \tag{7.4}$$

In many systems only a single type of nucleus forms, and it is typically single crystalline. However, this does not have to be the case. For example, it is common for face-centered cubic materials to have the co-existence of many different shapes in the very early stages of growth where clusters contain only a hundred or so atoms. [**14**,**115**,**132**] In some oxides there can also be more than one phase nucleated, such as in the case of titanium dioxide where both rutile and anatase can nucleate simultaneously. [**133**] As analyzed extensively in the energy-landscape works by Berry et al. [**8**, **134**] and others [**135**, **136**], one often has a complex potential energy landscape with relatively small energy barriers. There can be significant conversion between different types of nuclei. (There can also be effects due to particle coalescence, see for instance [**29**, **30**].)

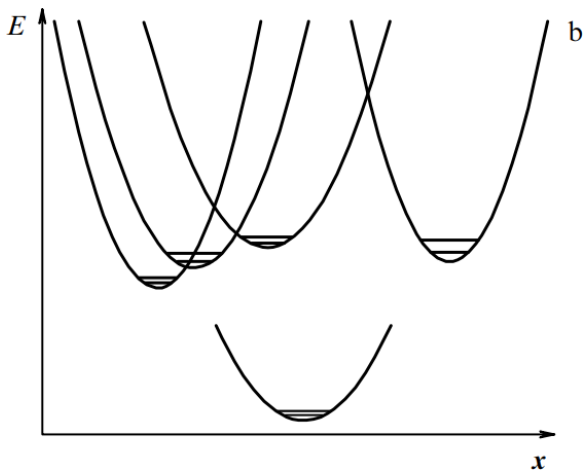

Figure 7.2. Potential energy surfaces for a 13-atom metal cluster. The potential energy wells represent several different clusters with configurational excitation. The surfaces of the wells are close in energy and at times intersectm suggesting interconversion and/or coexistence between each state. Image reproduced from [**8**].

Because the initial nuclei are very small, atoms can frequently move across the surface relatively rapidly so the outermost surfaces will tend to be in local equilibrium. The energy

barriers between different shapes and internal structure are also small. The addition of more atoms from the solution to a cluster reduces both the probability of interconversion of nuclei and rate of atom transport across a surface. As the size increases the particles will become more locked in to a given phase, although there can still be slower transitions. An example of this is shown in Figure 7.3, where the phase transformation from cubic-rich $BaTiO_3$ particles to tetragonal-rich $BaTiO_3$ particles is observed through the continuously changing lattice parameter measured from XRD patterns. [**9**] Polymorphic transformation has also been incorporated into some crystallization models, in particular for non-equilibrium metastable phases, as shown in Figure 7.4. [**10**, **36**, **137**] Once the particles are "frozen," the processes that determine further growth end up controlling the shape, which is the primary focus of this chapter and described in the next section.

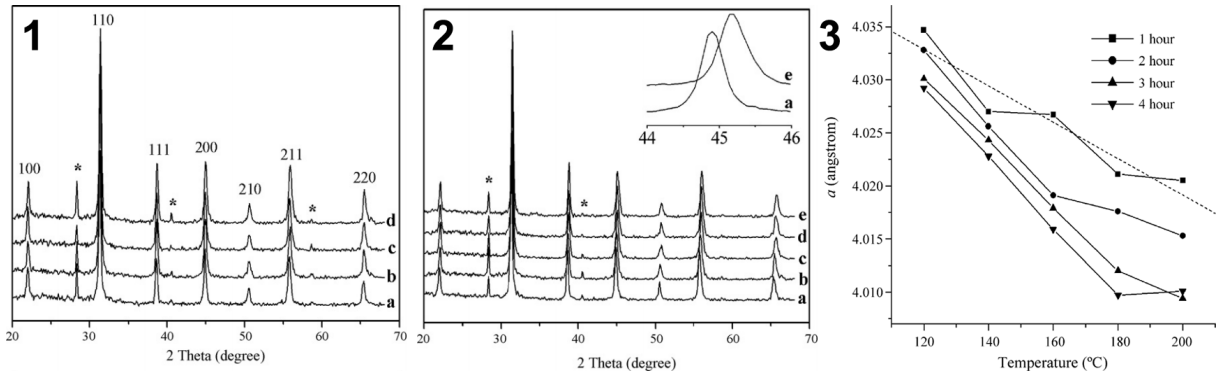

Figure 7.3. XRD patterns of $BaTiO_3$ samples hydrothermally synthesized at (1): 140 °C for (a) 1 hr, (b) 2 hr, (c) 3 hr, and (d) 4 hr. (2): 4 hr and (a) 120 °C, (b) 140 °C, (c) 160 °C, (d) 180 °C, and (e) 200 °C. (3): Value of lattice constant a of $BaTiO_3$ particles calculated from XRD patterns using a cubic symmetry. Images reproduced from [**9**].

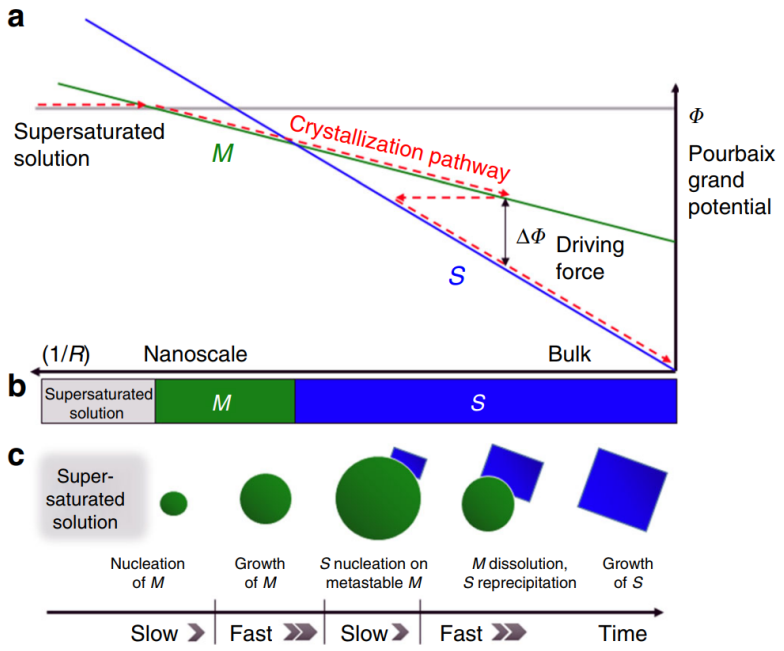

Figure 7.4. Schematic of crystallization pathway for MnO_2. (a) Free energy of supersaturated solution, metstable phase with low surface energy (M), and low energy stable phase (S) as a function of surface area-to-volume ratio ($1/R$). (b) Phase diagram created from the projection of the lowest free energy phases in (a). (c) Multistage crystallization pathway showing phase transformations between polymorphs. Image reproduced from [**10**].

7.2.2. Shape Determining Growth

Unfortunately there is no one-size fits all model for determining how particles will grow and what shape will take form. Different growth modes can occur depending on the thermodynamic and kinetic contributions of all components in the synthesis system, including the total chemical potential of the solution, the chemical potential variation of solution components over time, or chemical processes like selective chemisorption of surfactants on particle surfaces. It is easiest to look at several limits to the growth modes based upon their physical characteristics and how environmental contributions influence their behavior:

(1) **Thermodynamic control**: At equilibrium, minimization of total surface energy takes precedence, and particle shape is determined by the thermodynamic Wulff construction.

(2) **Flat-surface step-flow growth**: A kinetic-type growth mode where the rate-limiting step is growth via steps or terraces on the surface of an existing nucleus. Under this limit, the probability of growing an existing step on a particle surface is significantly greater than that of nucleating a new terrace.

(3) **Rough-surface growth**: A kinetic-type growth mode similar to (2) but the probability of nucleating a new terrace is comparable to or larger than growth of an existing terrace.

(4) **Diffusion-controlled growth**: A type of kinetic growth where rate-limiting process is flux of molecules to the surface of a growing nucleus.

Throughout this chapter, we will describe each of these growth modes in more detail. Relevant examples from literature will be presented to demonstrate both the physical properties of each growth mode and the mechanisms behind each type of thermodynamic or kinetic control.

7.3. Thermodynamic Control: Equilibrium and Thermodynamic Wulff Shape

A system is in thermodynamic equilibrium when the chemical potential is constant everywhere. In crystal growth, equilibrium is reached when there is enough time and energy for chemical and physical processes to occur so that both equilibrium stable phases and shapes can form. Based upon theories developed by Gibbs [**138**, **139**] and Wulff [**33**] as well as important proofs by Herring [**140**] and others [**141**] it was determined that the

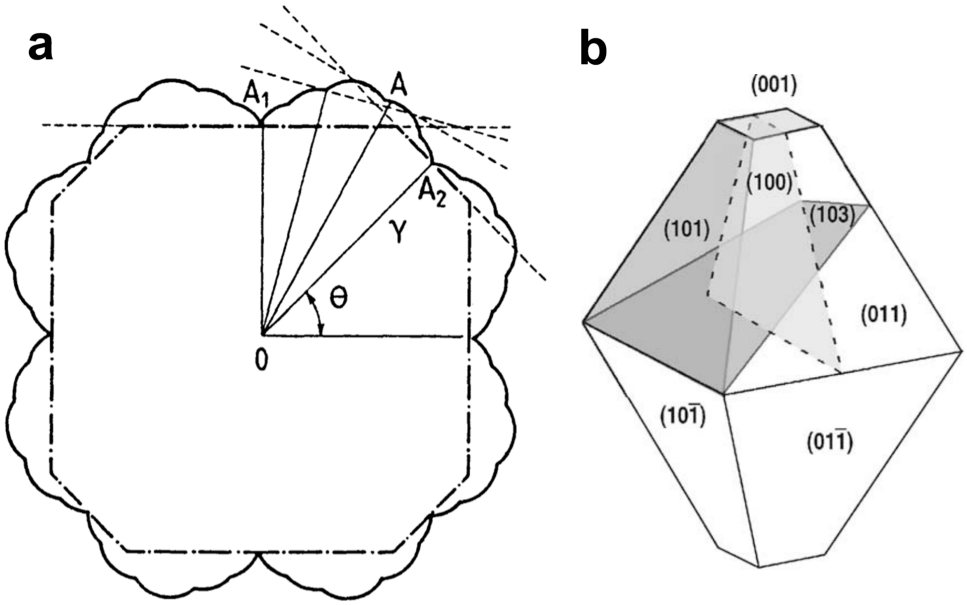

Figure 7.5. (left) Illustration of a gamma plot for the thermodynamic Wulff construction. Image reproduced from [**11**]. (right) Wulff shape for anatase TiO_2 calculated with surface energies determined by density functional theory. Image reproduced from [**12**].

lowest energy shape of a crystal minimizes its surface energies. The Wulff construction is a mathematical method used to determine this equilibrium shape. [**33**] It is defined mathematically for a crystal with constant volume as:

$$S = x : x \cdot \hat{n} \leq \lambda\gamma(\hat{n}) \tag{7.5}$$

where S is the set of points defining the shape, x are points within $\hat{n} \leq \lambda\gamma(\hat{n})$, $\hat{n}$ is a unit vector for crystallographic face (hkl), λ is a Lagrange multiplier for the fixed volume condition, and $\gamma(\hat{n})$ is the surface free energy of the facet defined by $\hat{n}$. The simplest way of demonstrating this is via a polar plot of surface energy as a function of crystallographic orientation, as shown in Figure 7.5a. In this plot, lines are drawn from the origin to each

γ point, and where these lines intersect with $\hat{n}$ another line perpendicular to $\hat{n}$ is drawn. The inner envelope of these perpendicular lines represents the equilibrium Wulff shape.

If surface energies are unknown for a material, they can be calculated using density functional theory, as was done to calculate the Wulff shape of anatase TiO_2 in Figure 7.5b. [**12**] Experimentally, a post-synthesis anneal is often needed to form the equilibrium shape because the high temperature provides more energy and time necessary for bulk and surface diffusion processes to occur and reduce the total energy of the crystal. This method has been employed to study the thermodynamic shapes of materials, such as $SrTiO_3$. [**13**]

While many cases exist for equilibrium Wulff shapes, there are two complicating factors. One is that the kinetic shapes can be confused with thermodynamic ones, which we will describe later. The other is the strong effect of surface active species, such as chemisorbants, which can not only change the surface energy but also enhance or limit the rate of growth of certain facets, as will be discussed in the kinetic growth modes. Many experimentally grown crystals are not defect-free, and therefore extensions of the thermodynamic Wulff construction have been developed to incorporate the effect of twin boundaries and planar defects. [**94**]

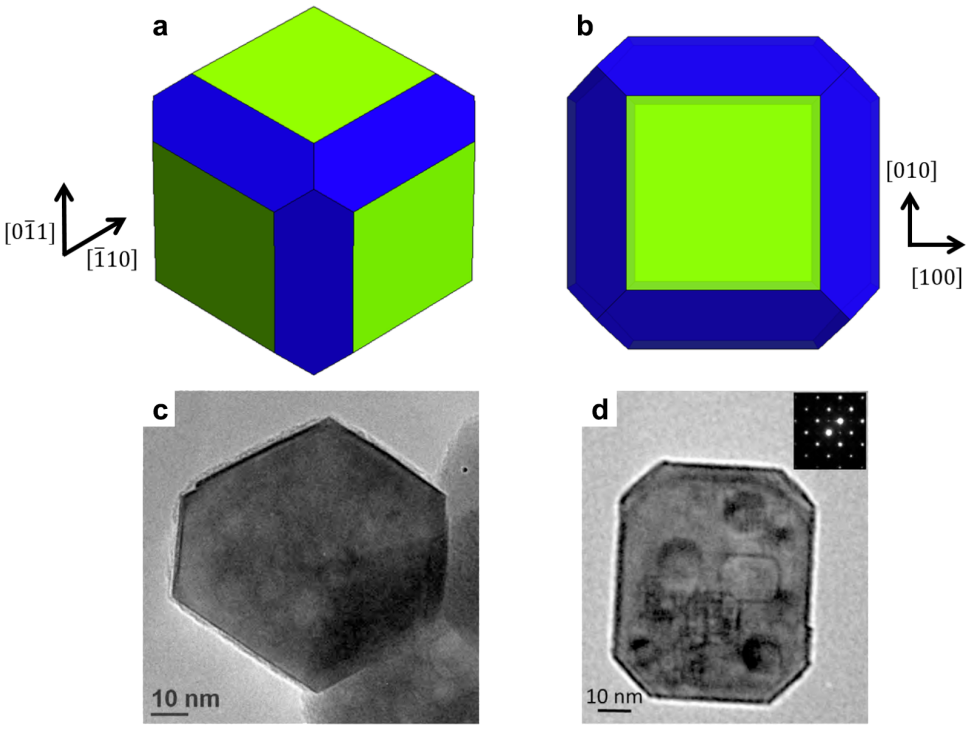

Figure 7.6. Projections of $SrTiO_3$ Wulff shape along (a) [111] and (b) [001] zone axes. {100}-type facets are green, and {110} facets are blue. Experimental TEM images of annealed $SrTiO_3$ nanocuboids demonstrating Wulff shape imaged on (c) [111] and (d) [001] zone axes. Image reproduced from [**13**].

7.4. Flat-Surface Step-Flow Growth: Kinetic Wulff Shape

In many cases particles have flat surfaces, but these are due to step flow growth and what is called the kinetic-Wulff shape. To understand these, we first need to consider growth on an existing terrace. A schematic of the terrace nucleation and growth processes is provided in Figure 7.7 reproduced from Chapter 2. In this schematic, the red block represents a solute in solution diffusing to the surface of a nucleated crystal with an existing growth terrace. Terrace nucleation is the process where the solute reacts to form a new terrace on top of the terrace or surface, and terrace growth happens when the solute reacts to grow an existing terrace laterally across the crystal surface.

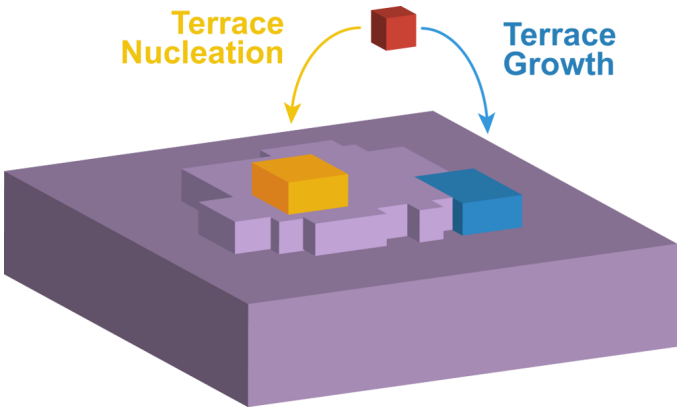

Figure 7.7. A schematic of terrace nucleation (yellow) and growth processes (blue). The purple block represents the surface of a nucleated particle with a growth terrace, and the red block represents a solute species in solution. Image from Chapter 2.

If we model the growth terrace as a 3D hemisphere, we can derive the free energy cost and rate of terrace nucleation mathematically. The total work or free energy change for nucleation of a 3D hemispherical terrace nucleus is:

$$\Delta E = \frac{2}{3}\pi R^3 \Delta\mu + 2\pi R^2 \gamma \qquad \text{(2.3 revisited)}$$

where R is the radius of the terrace nucleus, $\Delta\mu$ is the chemical potential change of forming the nucleated material, and γ is the surface energy. Similar to the homogeneous nucleation case, there is also a critical radius (R^*) for terraces nucleated at the surfaces of particles. The critical nucleation energy evaluated at R^* is:

$$\Delta E(R = R^*) = \frac{8\pi\gamma^3}{3\Delta\mu^2} \qquad \text{(2.4 revisited)}$$

Then, the terrace nucleation rate can be written as:

$$N_R = f_0 \exp \frac{\Delta E}{k_B T} \qquad \text{(2.5 revisited)}$$

where f_0 is a pre-exponential factor that is dependent on the diffusion of molecules and solutes in solution and other factors. Based upon Equations 2.4 and 2.5, the terrace nucleation rate is notably dependent on both the surface energy and chemical potential change.

Terrace growth does not involve a nucleation type process and correspondingly has a lower free energy cost. It is still influenced by the supersaturation, or chemical potential, of the solution environment. The rate of terrace growth (G_R) can be defined as:

$$G_R = C\Delta\mu \qquad (7.6)$$

where C is a coefficient that includes diffusivity and other environmental terms. In order to compare it more directly against the terrace nucleation rate, the process of terrace annihilation can be used instead as the occurrence when a terrace grows to the edge of a surface and annihilates itself. This process is particle size-dependent and can be defined

as:

$$A_R = \frac{1}{Area} G_R \qquad \text{(3.4 revisited)}$$

Classic step-flow growth is the growth mode where the rate of terrace nucleation is slow, and it is often an interface-controlled growth. When the rate of terrace nucleation is slow, then the process of terrace growth is more likely. As discussed in Chapter 3, terrace growth and eventual annihilation at the edge of a particle results in the growth of particles with smooth facets. This type of shape is determined by what is called the kinetic Wulff construction, which is formed by the envelope of the slowest growing facets, i.e.:

$$S = x : x \cdot \hat{n} \leq \lambda(t) v(\hat{n}) \qquad (2.2)$$

where v is the growth velocity dependent on time t for each facet defined by $\hat{n}$. Figure 7.8 demonstrates this schematically in a 2D example with two surfaces with different growth rates. [**14**] The kinetic Wulff construction is mathematically similar in construction to the thermodynamic analogue described in Equation 7.5; however, growth velocities replace the role of surface energies. Likewise, if the polar plot shown in Figure 7.5 of surface energy is replaced with a polar plot of growth velocities, the plot becomes a diagram of the kinetic Wulff construction.

In some instances, the kinetic Wulff shape of a grown particle may resemble its thermodynamic Wulff shape, but these occurrences are only coincidental and do not indicate that equilibrium conditions were met. While thermodynamic quantities such as surface energies can be used to calculate the equilibrium shapes of particles, growth velocities are more variable, making it a challenge to predict kinetic shapes. A popular method

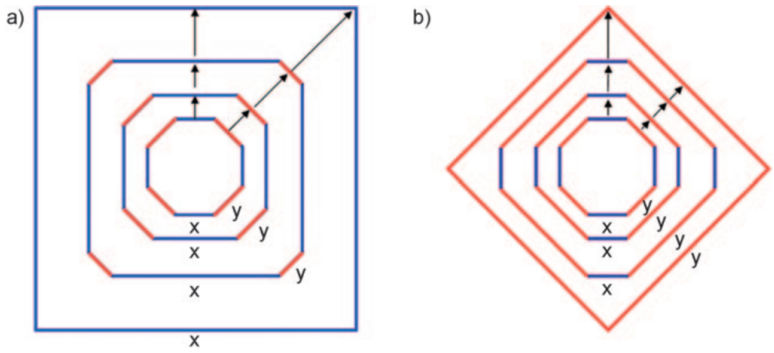

Figure 7.8. Schematic of a 2D crystal with two surfaces x and y with different growth rates. (a) When the growth rate normal to y is faster than that of x, the y surfaces eventually disappear leaving an x-type surface terminated crystal. (b) The opposite case where the growth rate normal to x is faster than that of y. Image reproduced from [**14**].

to control the growth velocities of a crystal surface is to use surfactant molecules that selectively adhere to specific surfaces. By adsorbing onto the surfaces of specific planes, they lower the energy of that plane and also slow its growth be preventing the deposition of precursor ions or molecules onto the surface. For example, the rate of growth normal to the {001} surface in anatase TiO_2 was slowed by using fluoride ions as a surfactant. As shown in Figure 7.9, increasing the concentration of surfactant transformed the kinetic Wulff shape of anatase grown from truncated octahedron to sheets with preferential {001}-type facets. [**15**]

Surfactant molecules can do more than only affect the surface of a particle. Some may double as mineralizers in solution and affect the solubility of the precursors. In the case of α-Fe_2O_3, the mineralizer NaF was successfully used as both a mineralizer to vary the chemical potential of the precursor in solution and transform the kinetic Wulff shape of particles grown. The transformation of kinetic Wulff shape from dodecahedral-type to octadecahedra is shown in SEM images in Figure 7.10. [**16**]

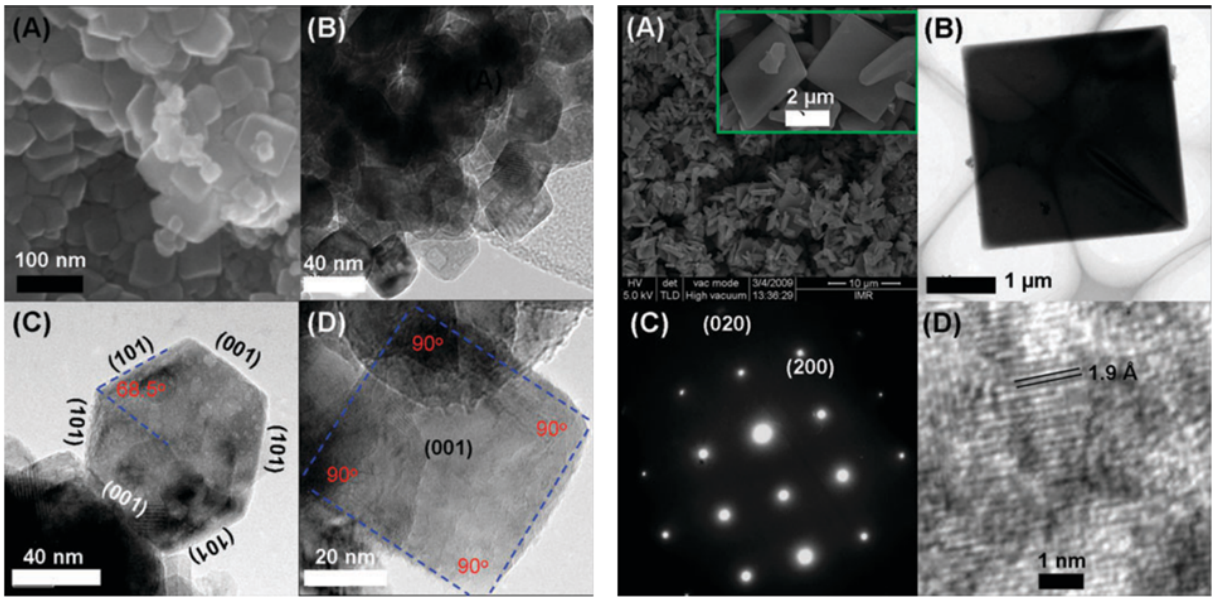

Figure 7.9. (left): Low magnification (a) SEM and (b) TEM images of anatase TiO_2 particles with truncated octahedron shape. (c) Profile-view and (d) top-view of truncated octahedron shows terminating {101} and {001}-type surfaces.

(right): (a) SEM and (b) TEM images of anatase TiO_2 nanosheets with a large percentage of {001}-type facets. (c) Electron diffraction pattern of [001] zone and (d) HRTEM image of nanosheet.

Both images are reproduced from [**15**].

One more approach to changing the rate of growth of different facets is through defects. Planar defects such as twin boundaries and planar defects have been known to accelerate the growth rate along the geometry of the defect because of preferential coordination. [**14**, **94**–**98**, **115**] This type of preferential growth often times produces flat or plate-like particles as a result. For instance, Figure 7.11 shows how two octahedral crystals sharing a (111) twin boundary are elongated by this type of growth phenomenon. [**17**]

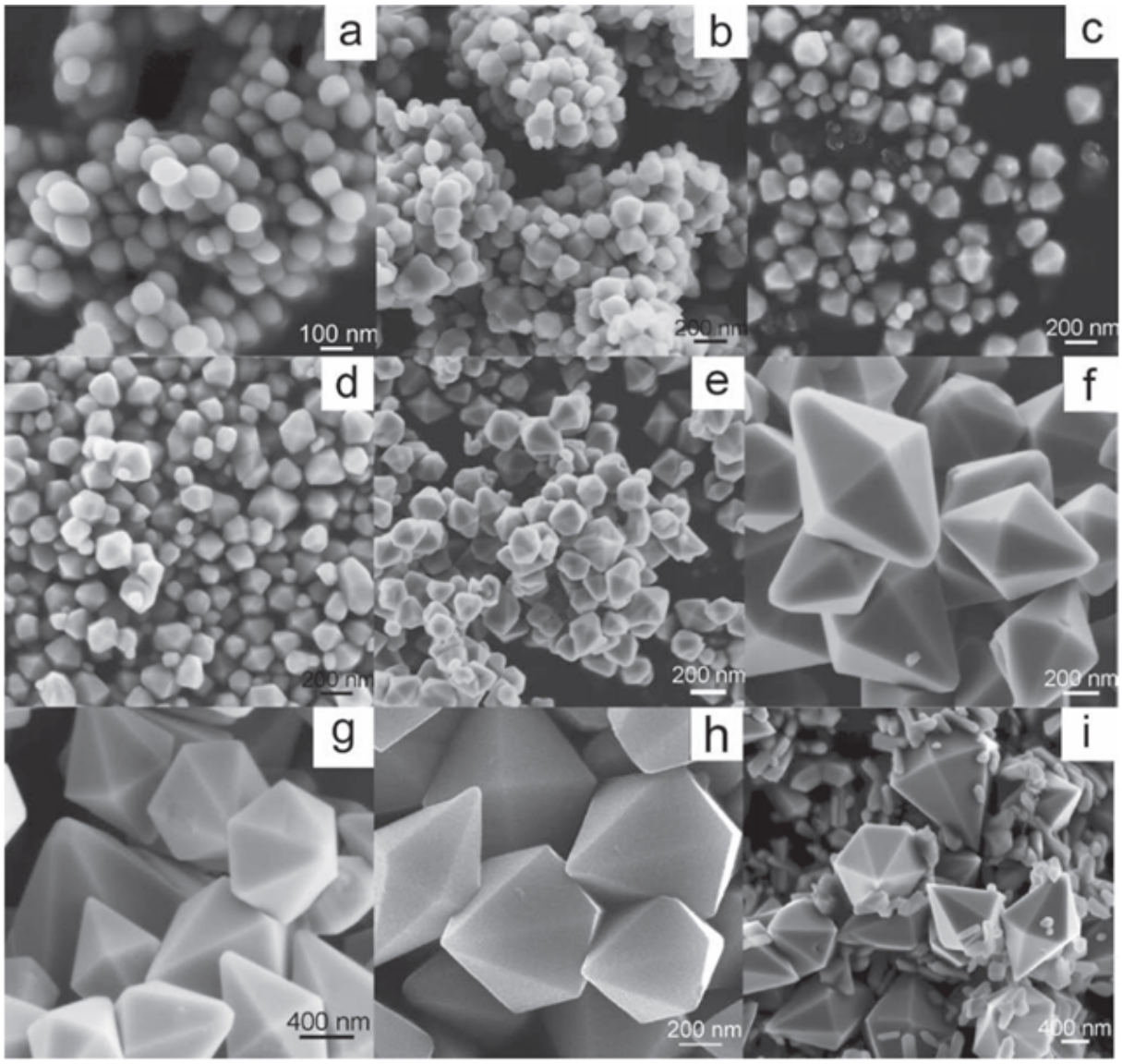

Figure 7.10. SEM images of α-Fe_2O_3 synthesized with (a) 0, (b) 6, (c) 12, (d) 15, (e) 18, (f) 24, (g) 26.5, (h) 25.5, and (i) 28 mM NaF concentrations. At low concentrations, the particles are quasi-spherical. With increasing concentrations, the kinetic Wulff shape transforms from dodecahedron then octadecahedron. Image reproduced from [**16**].

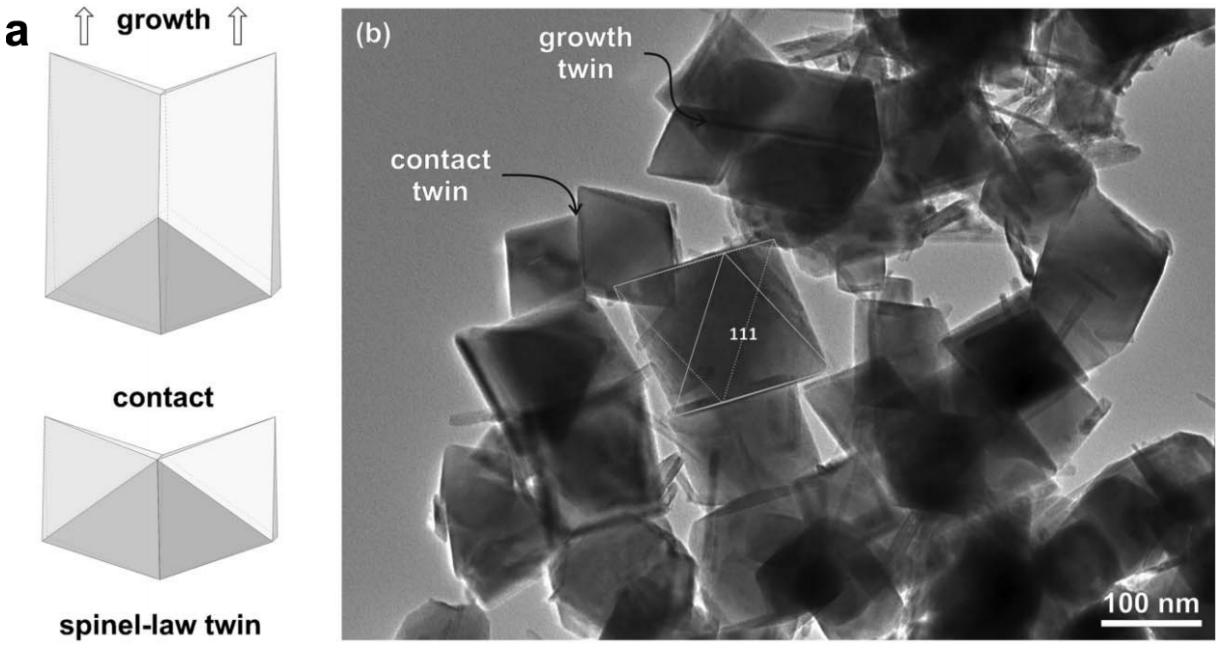

Figure 7.11. (a) Illustration of (111) twin boundary between two crystals and accelerated growth direction that elongates the particle. (b) TEM images of (111)-type twinned particles of hydrothermally synthesized magnetite. Image reproduced from [**17**].

7.5. Rough-Surface Growth: Terracing Regime

The rough-surface growth mode relies on the same terrace nucleation and terrace growth processes described for step-flow growth. However, in this case the rate of terrace nucleation (N_R) is similar to or greater than the rate of terrace growth, or more specifically terrace annihilation rate (A_R). The effects of this were described in depth in Chapter 3 and are summarized here briefly. If $N_R > A_R$, then there are more terraces forming on particle surfaces than terraces reaching the edge of a facet. With this type of growth behavior, particles will be unable to form smooth, flat facets as in the flat-surface growth mode, alternatively called the smoothing regime. Instead, the particles have surfaces populated with many growth terraces and take on a rough appearance, which is why this growth mode may also be called the terracing regime. Rough surface growth is often responsible for the growth of irregularly shaped particles.

The consequences of the competition between the rates of terrace nucleation and terrace annihilation are most clearly seen in the hydrothermal synthesis of KTO particles imaged in Figure 7.12. [**1**] In this synthesis, the rates of both growth processes continually varied as the chemical potential of the system decreased. As an exponential function, N_R is more sensitive to a change in chemical potential compared to A_R, so N_R also decreased more rapidly as time progressed in this reaction. The series of images illustrate the rough morphology of particles when $N_R \gg A_R$ early on during the reaction. In the middle of the reaction, the terrace density decreases because the terrace nucleation and annihilation rates became more comparable ($N_R > A_R$). At the end of the reaction, $N_R < A_R$, causing the growth mode to switch to the flat-surface, smoothing regime.

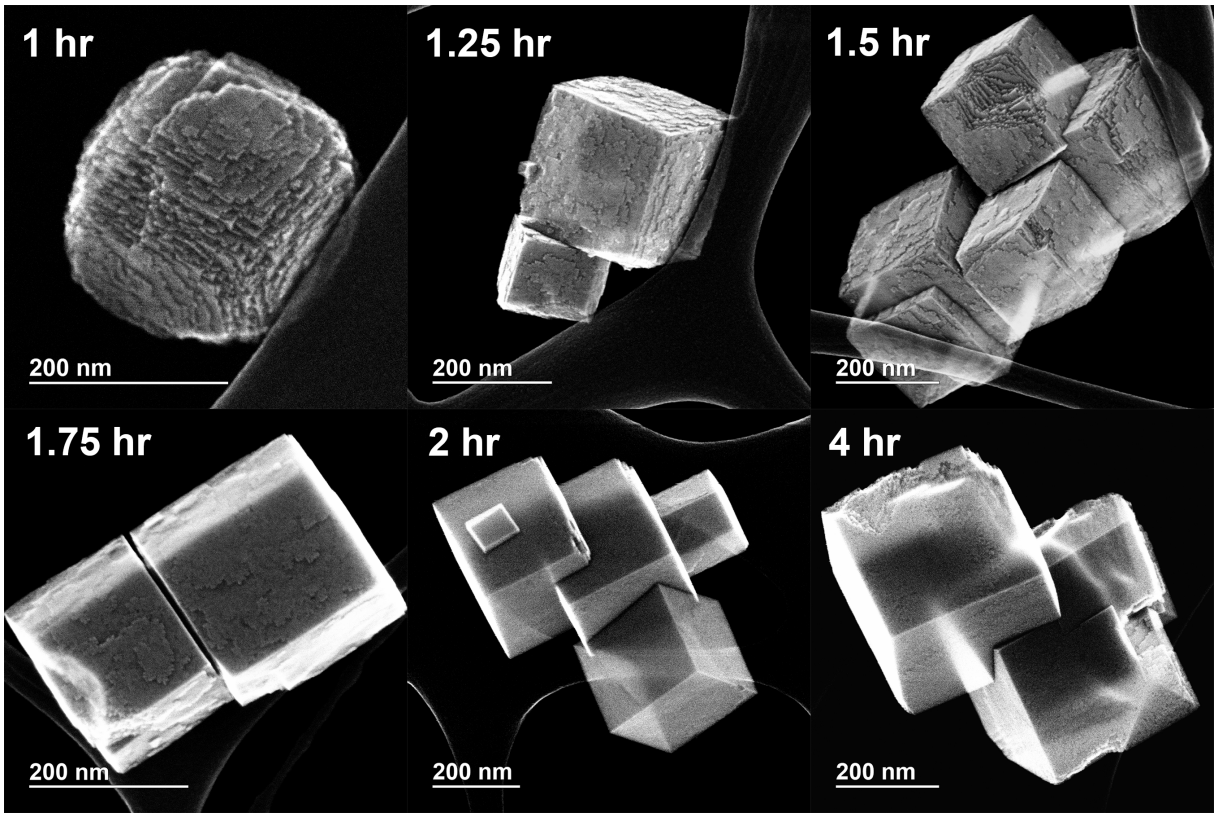

Figure 7.12. SE images of hydrothermally synthesized KTO NPs with changing surface morphology as the reaction progressed from 1 to 4 hr. Image reproduced from [**1**].

This type of rough surface growth mode has also been observed by Hou et al. [**18**] and Wang et al. [**19**] separately through the hydrothermal synthesis of $LaCrO_3$ with varying concentrations of urea. Figure 7.13 shows SEM images of the shape transformation from flat-surface cuboids to rough surface particles under this growth mode.

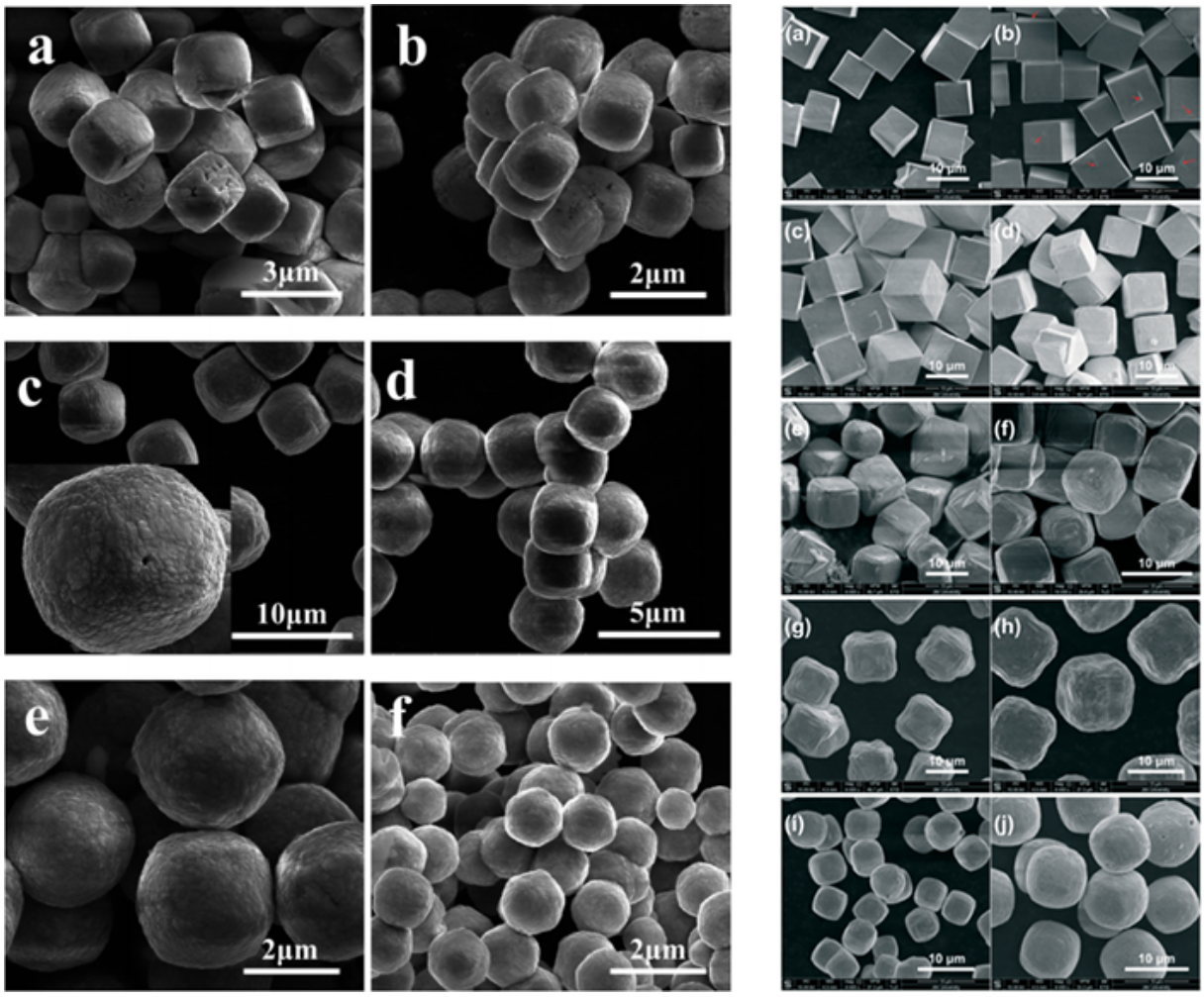

Figure 7.13. SEM images of $LaCrO_3$.

(left): $LaCrO_3$ studied by Hou et al. grown with different urea amounts: (a) 1.0 g, (b) 1.2 g, (c) 1.4 g, (d) 1.66 g, (e) 1.8 g, and (f) 2.0 g.

(right): $LaCrO_3$ synthesized by Wang et al with different urea amounts: (a) 0 g, (b) 0.2 g, (c) 0.4 g, (d) 0.6 g, (e) 0.8 g, (f) 1.0 g, (g) 1.2 g, (h) 1.4 g, (i) 1.6 g, and (j) 1.8 g.

Images reproduced from [**18**] and [**19**].

7.6. Diffusion-Controlled Growth: Dendrites

Diffusion-controlled growth is the last category of growth modes. For hydrothermal synthesis, diffusion-controlled growth is somewhat rare because one of the major advantages of hydrothermal conditions is that the temperature and pressure conditions significantly increase the dissolution of all precursors in the solvent. However, there are conditions where dissolution is difficult, and limited dissolution limits the amount of mass that can be transported to growing surfaces. Under these conditions, diffusion-limited growth is favored and has been observed for a few different materials. In such cases, the growth rate in different directions is not dependent on the growth mechanisms as in kinetically formed shapes, but rather local curvature.

The local curvature of a crystal or of features on a crystal surface is significant to the morphology of a crystal because of its effect on the chemical potential. In combination with information about the local curvature and chemical potential derived by the Mullins-Herring equation, [**142**, **143**] the Gibbs-Thomson relation can be used to demonstrate this relationship. For the case of a spherical particle of radius R, the difference in the equilibrium chemical potential and the local chemical potential is:

$$\Delta\mu = \frac{2\Omega\gamma}{R} \tag{7.7}$$

where Ω is the atomic volume. An equivalent relationship for a curved step or terrace of radius R on a growing crystal surface applies if the surface tension is replaced by line tension. This relationship shows that as the curvature of a surface increases, the chemical potential also increases. If the chemical potential is large at sites of high curvature, then those sites are also less stable. Solute species diffusing to the surfaces of growing crystals

will energetically favor sites of lower curvature. Additional effects on particle morphology and corner rounding have been discussed by Alpay et al. [**144**]

A more specific case of diffusion-limited growth is dendritic growth, where a shape instability at the interface can result in the formation of dendrites with characteristic needle-like shapes and branches. The shape instability can be in the form of a perturbation, such as a bump or protuberance, at the interface. Although surface tension typically has a stabilizing effect in these types of protuberances, limited diffusion rates can have a destabilizing effect for sufficiently large perturbations. Solute diffusing to the growth interface will encounter the protuberance first, and under diffusion-limited growth there is a higher probability that solute will react and contribute to the growth of the protuberance rather than diffusing across the bump to the flatter portion of the interface. This results in unstable growth of the protuberance and the formation of dendrites.

Dendritic growth has been observed in the hydrothermal syntheses of both $SrTiO_3$ and $BaTiO_3$. Figures 7.14 and 7.15 shows TEM images of the $SrTiO_3$ and $BaTiO_3$ dendrites, respectively. [**20**,**21**] In both of these cases, the number and size of dendritic protuberances was inversely correlated to the concentration of mineralizer (KOH) used in synthesis. When a lower concentration of KOH was used, the solubility of the oxide precursors were limited, resulting in diffusion-controlled growth.

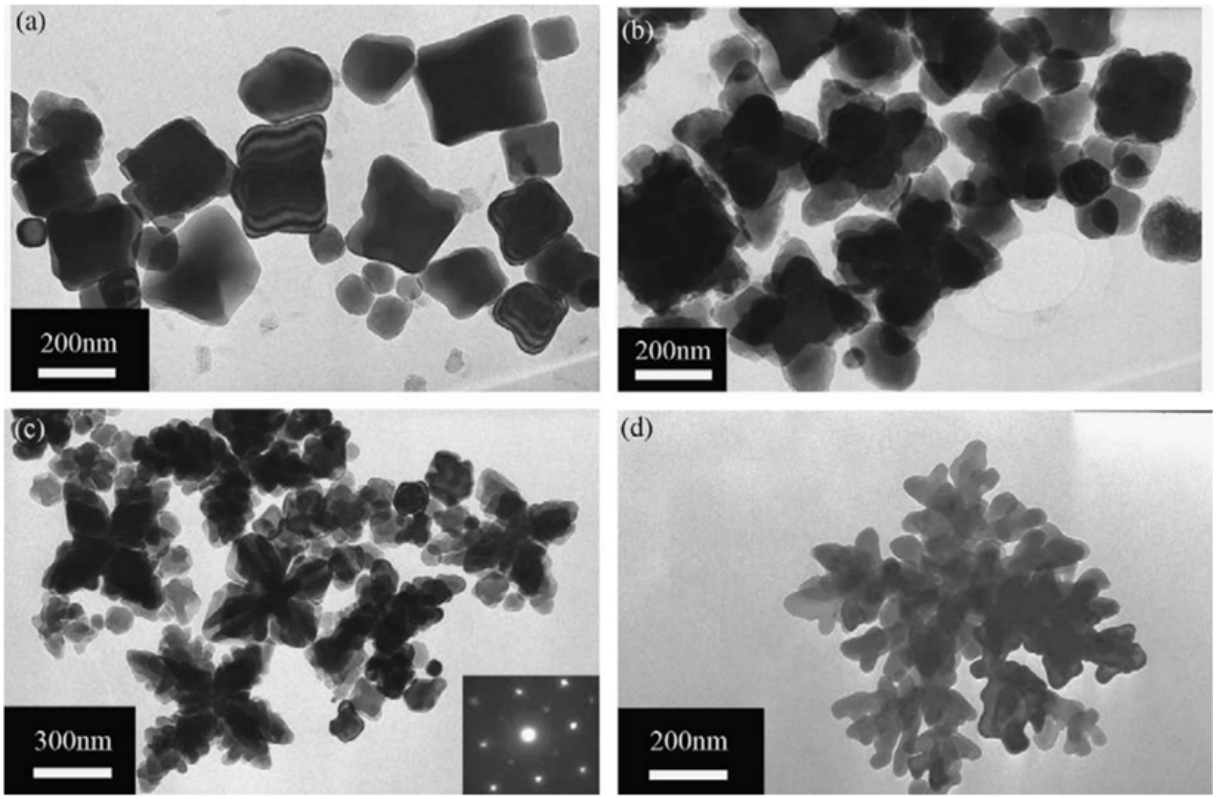

Figure 7.14. TEM images of $SrTiO_3$ dendrites synthesized hydrothermally with different amounts of KOH: (a) 1 M, (b) 0.7 M, (c) 0.3 M, and (d) 0.1 M. Image reproduced from [**20**].

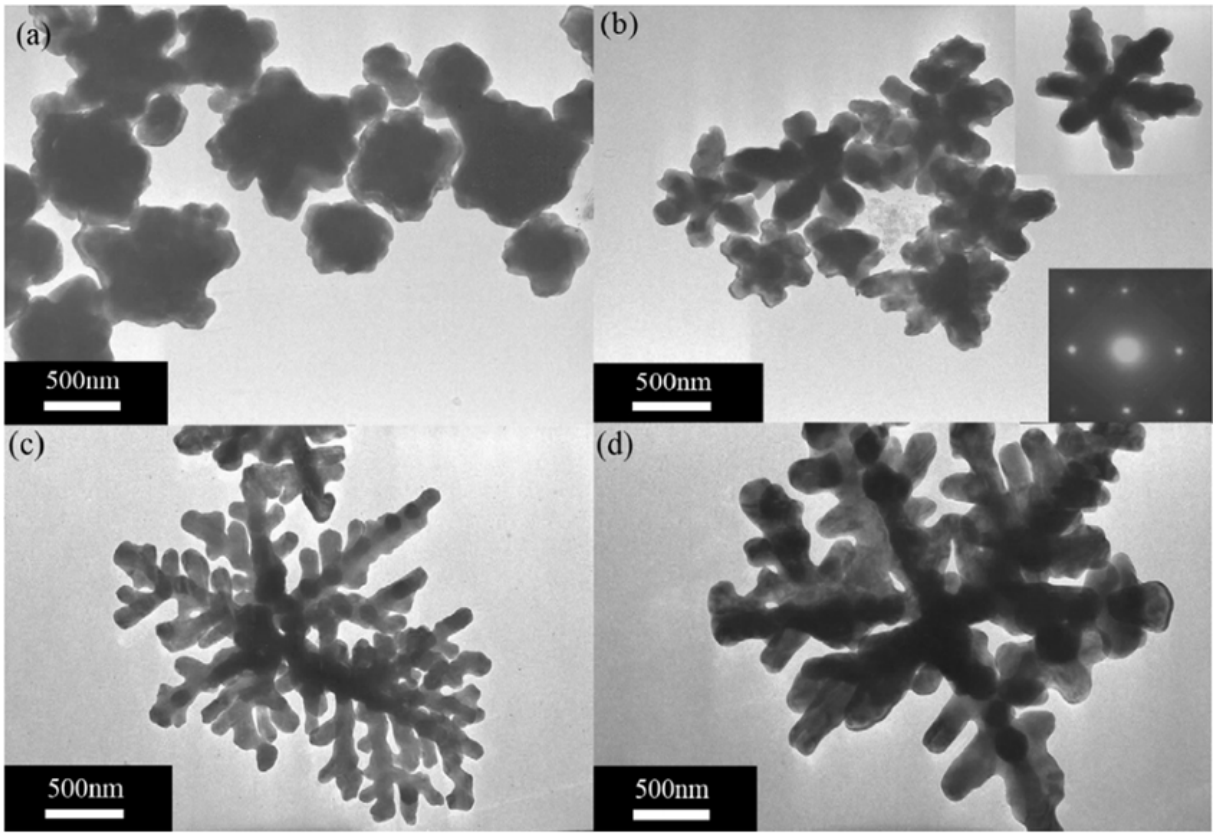

Figure 7.15. TEM images of $BaTiO_3$ dendrites synthesized hydrothermally with different amounts of KOH: (a) 1 M, (b) 0.7 M, (c) 0.3 M, and (d) 0.1 M. Image reproduced from [**21**].

7.7. Conclusion

The crystal growth process under hydrothermal conditions was described from initial nucleation in a solution to step-flow growth on nuclei surfaces. These processes determine many properties of the nanoparticles grown, including the phase(s), size, shape, and surface, and thermodynamic and kinetic contributions control many of these aspects. Four categories of growth modes were defined to explain some of these thermodynamic and kinetic contributions: one thermodynamically controlled and three kinetically controlled. Examples of each type of growth mode were presented to describe how different components in a synthesis can cause each behavior. By understanding why each type of growth occurs, nanoparticle syntheses can be designed to optimize conditions for a preferred growth mode.

The thermodynamically controlled growth mode is the limit of equilibrium, which is rarely observed under thermodynamic conditions, but theoretical calculations or post-synthesis processing have proven to be useful to characterize this type of growth mode. The three kinetically controlled growth modes are the limits of three different rate limiting steps. Under the flat-surface step-flow growth mode, the rate limiting step is the nucleation and growth of terraces on a nucleated particle surface. This type of growth mode is very sensitive to components in the synthesis that modify surface energy, such as surface active molecules in solution. In the rough-surface growth mode, the rates of terrace nucleation and growth are more comparable. For particles growing in these conditions, the properties of both the solution thermodynamics and surface properties have consequences on the morphology of the products. The diffusion-controlled growth mode is limited by the mass transport of solute to crystal surfaces. For a solution-based method

like hydrothermal synthesis, this is primarily controlled by the solubility of the precursors in the solvent aided by the mineralizer.

CHAPTER 8

Future Work

The work discussed in this dissertation presents a fairly comprehensive overview of the growth processes and their kinetics of hydrothermally synthesized KTO, KNO, and KTN particles. The surfaces, composition, microstructure, and chemical behavior were all explored through both experiment and theory. When considering future directions for such a body of work, one important question to ask is whether there is more work to be done on this material system, or if it is an appropriate time to move onto other materials. There are interesting possibilities in both directions. By remaining with the same material system, prior knowledge about the synthesis conditions and material behavior provide a good background upon which to build. On the other hand, exploring a new material system offers entirely new parameters to investigate and different challenges that may be exciting from a scientific perspective. Some ideas and hypotheses for both avenues of future work are outlined below.

8.1. Modifications of $KTa_{1-x}Nb_xO_3$ Synthesis

Moving from Chapter 3, 4, to 5, the complexity and quantifiable number of parameters involved in synthesis gradually increased. We began with a single material system with two precursors and ended with a synthesis involving four components, as well as a variety of compositionally and morphologically tunable properties. Some of the approaches used to study the growth of these materials deserve additional consideration.

For example, in Chapter 5, the utility of KF as a mineralizer for the tantalum oxide precursor was characterized. It was demonstrated that when a sufficient amount of KF was present in solution, it could increase the stability of tantalum oxide in solution and decrease its rate of reaction with KOH to form the perovskite product. A natural extension of this result is to test the properties of KF as the only mineralizer in a synthesis and exclude KOH, which acted as both a precursor and mineralizer in this reaction. The overall chemical reaction between tantalum oxide and KOH is an acid-base reaction where the tantalum oxide is the acid and KOH is the base:

$$Ta_2O_5 + KOH \rightleftharpoons KTaO_3 \tag{8.1}$$

Similar to KOH, KF is also a basic compound when compared to tantalum oxide and could react in a similar fashion. It should be noted that Goh et al. determined that the KOH concentration is important for obtaining the perovskite phase because when the KOH concentration was at or below 7 M, a defect pyrochlore $KTa_2O_5(OH)$ could form as either an intermediate or final product. [**38**] By removing KOH from the reaction, the likelihood of forming this intermediate may be reduced while the likelihood of forming the defect-driven rectangular shaped particles observed in Chapter 5 may be increased. The formation energy calculations to form the RP-like defect phase showed that they could form when the KF/KOH ratio was above 0.10, while experimentally it occurred when KF/KOH $>$ 0.20. The basic environment was not considered when performing these calculations and may be the source of that difference.

Another possible outcome of removing KOH from the synthesis is a change in the surface properties. The surfaces of KTO particles in Chapter 3 were characterized to be

composed of a tantalum oxide phase, and the chemical potential of tantalum oxide in the reaction was responsible for the transformation in step-flow growth. As tantalum oxide is a chemically acidic compound, the tendency to form tantalum oxide surfaces could be influenced by the basic environment through the adsorption of hydroxyl groups to the surface. The stabilizing energetic effect of adsorbing water was already calculated in Chapter 4, so additional calculations considering hydroxyl groups could be performed in consideration of this possibility. Unlike KOH, KF is a weak base in water, so there will be fewer free hydroxide ions, reducing the tendency to form tantalum oxide type surfaces in KTO. This has the potential to entirely change the growth behavior at the particle surfaces.

One last possibility through this approach is a change in the type of kinetic control through which the particles grow. Dendritic growth, a specific type of diffusion-controlled growth, was described in Chapter 7, and examples in hydrothermal synthesis for $SrTiO_3$ and $BaTiO_3$ were presented. In both of these cases, dendritic growth tended to occur because of the low solubility of the precursors in solution that limited the mass transport to growing crystal surfaces. [**20**, **21**] KOH is a very effective mineralizer for the oxide precursors and there is no guarantee that KF is as effective, especially considering its weak properties as a base. Therefore, the solubility of the precursors may be limited to the point of limiting the rate of diffusion in the hydrothermal system. If the effectiveness of KF as a mineralizer is too low, experimenting with different mixtures of KF and KOH (e.g. KF/KOH > 1) may also produce interesting results.

The choice of mineralizer does not have to be limited to KF in future experiments. For example, other compounds in the halide series could also be chosen to determine their

effect on the growth behavior of these materials. In comparison to the fluoride ion, the anions of the other halides have a larger radius. If incorporated into the material in small quantities similar to fluoride, which introduced planar defects, these anions may change the microstructure in different ways. Experiments with acidic compounds that change the chemistry of the solution are also worth further consideration.

Beyond studying growth behavior through modifications of the hydrothermal synthesis, another goal on which to focus is composition. All of the KTN nanocuboids synthesized in this body of work showed significant compositional heterogeneity and segregation between tantalum and niobium to either the interior or surface of the particles. If the composition-dependent properties of these nanoparticles are to be studied in future efforts, it would be easier to work with more chemically homogeneous materials. We demonstrated in Chapters 4 and 5 two ways to change the relative reaction rates of the tantalum and niobium precursors, and these experiments establish a foundation for how to approach the design of a synthesis procedure for chemically homogeneous KTN particles.

8.2. New Material Directions

The idea of moving onto a different material has the potential to be both more exciting and challenging, and there are several options that merit this change. The most straightforward materials to explore next are the sodium tantalates ($NaTaO_3$) and sodium niobates ($NaNbO_3$), which only differ from the materials studied in this dissertation by their A-site. Both of these materials have attracted interest as electro-optic materials, photocatalysts, and piezoelectric materials. [**22**–**24**, **31**, **65**] Furthermore, these materials

have exhibited an interesting range of growth behaviors that have not been well explained in literature.

Song et al. explored the effects of temperature, reaction time, and precursor concentration on the structure and morphology of hydrothermally synthesized $NaNbO_3$ particles. [**22**] The precursors in this reaction were Nb_2O_5 powder and NaOH solution. Figure 8.1 shows the diverse range of morphologies produced when the NaOH concentration

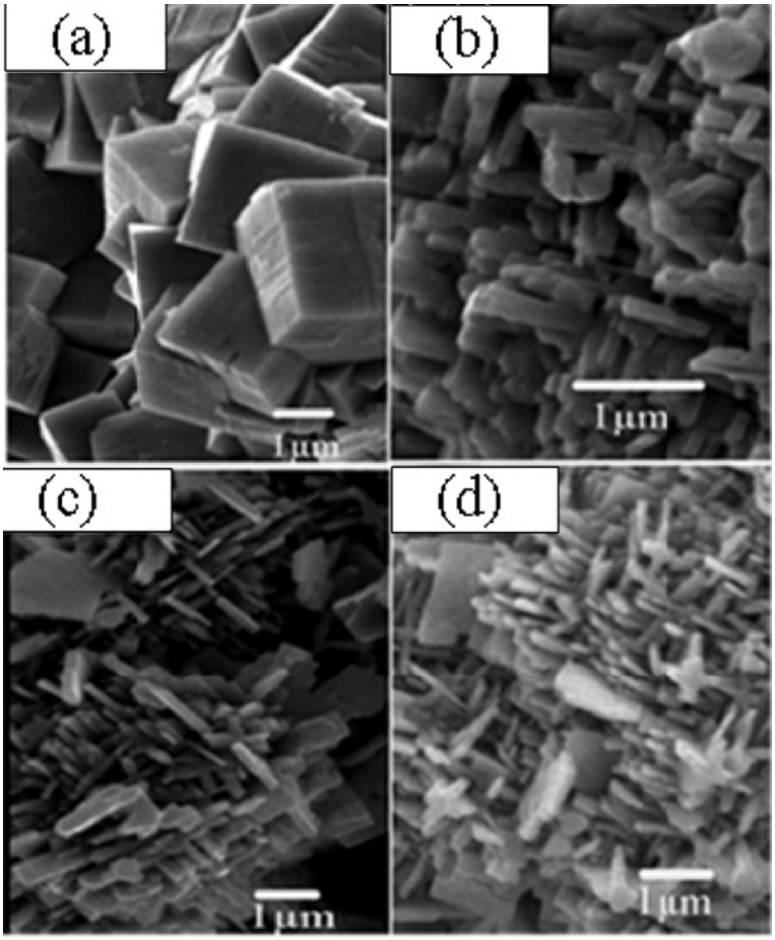

Figure 8.1. SEM images of hydrothermally synthesized $NaNbO_3$. All samples were heated at 180 °C for 8 hr with a 14 M NaOH solution and the following concentrations of Nb_2O_5: (a) 0.2 M, (b) 0.1 M, (c) 0.05 M, and (d) 0.03 M. Reproduced from reference [**22**]

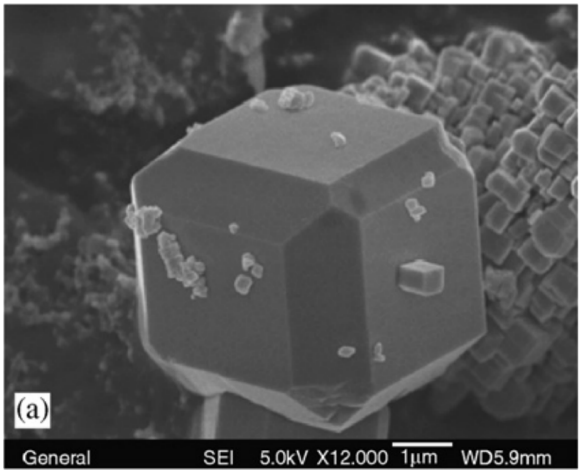

Figure 8.2. SEM image of $NaNbO_3$ synthesized with 14 M NaOH and an undisclosed amount of Nb_2O_5 at 240 °C for 24 hr. Reproduced from [**23**].

was 14 M and the concentration of Nb_2O_5 was varied from 0.02–0.2 M. The shape of the particles produced changed from nanocuboids to nanorods to nanoplates as the quantity of Nb_2O_5 decreased. Additional XRD patterns suggested that the amount of orthorhombic phase produced was somewhat correlated to the amount of Nb_2O_5 used. In another study where hydrothermal treatment was performed at a higher temperature (240 °C), $NaNbO_3$ particles were also produced with primarily nanocuboidal shapes with secondary facets between the square facets, as shown in Figure 8.2. [**23**] Evidently there are numerous types of kinetic Wulff shapes that $NaNbO_3$ can take through hydrothermal synthesis. These shapes may be correlated slightly to the phase grown, but they appear to be more sensitive to changes in thermodynamic quantities such as temperature and chemical potential of the solution, making it a promising material to study for understanding particle growth mechanisms.

$NaTaO_3$ is often doped in order to improve its photocatalytic activity. [**24**, **31**, **145**] It was found that doping with lanthanides could increase the photocatalytic activity

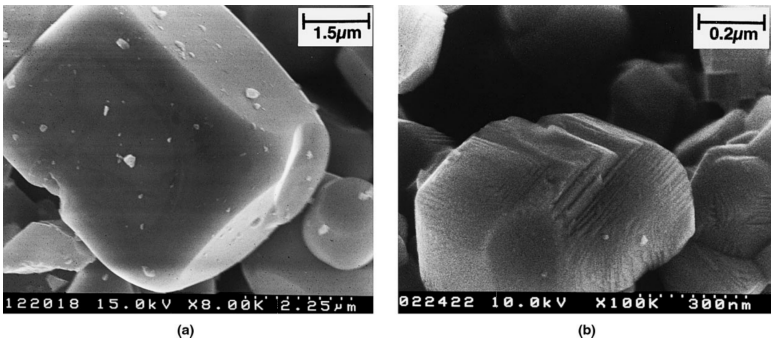

Figure 8.3. SEM images of (a) $NaTaO_3$ and (b) $NaTaO_3$ doped with 1.5 mol% La. Reproduced from [**24**].

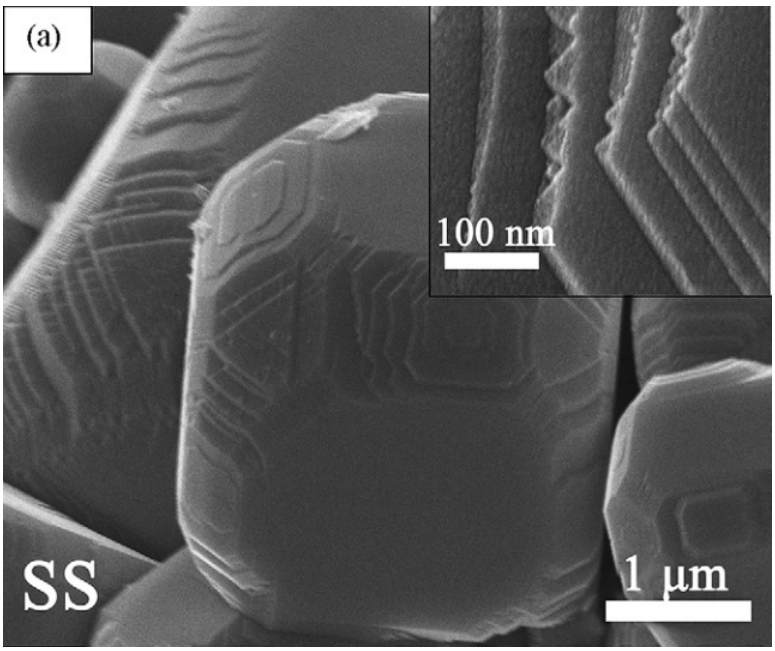

Figure 8.4. SEM image of $NaTaO_3$ synthesized by solid-state synthesis exhibiting characteristic step structure on the surface. Reproduced from [**25**].

of $NaTaO_3$, and that this increase in activity may be linked to a characteristic step structure that forms on the surfaces of the material when doped. [**24**, **145**] SEM images comparing the morphology of $NaTaO_3$ synthesized with and without doping are provided in Figure 8.3. [**24**] The surfaces of $NaTaO_3$ without doping has a cuboidal shape with

flat surfaces. When doped with 1.5 mol% La, the surfaces develop a distinct stepped structure that resembles the surfaces of particles grown in the terracing regime. Although the formation of this step morphology was attributed to doping, similar step features were also observed on un-doped $NaTaO_3$ by repeated calcined after solid-state synthesis as shown in Figure 8.4. [**25**] Lanthanum-doped $NaTaO_3$ has also been synthesized successfully using hydrothermal synthesis, and these particles had flat surfaces. However, as shown in Figure 8.5, there was a mix in the population of Wulff shapes formed, including cuboids, octahedra, and irregularly shaped particles. [**26**] The range in shapes and morphologies observed through all of these synthesis methods and doping levels indicates that this material has interesting growth behavior near the thermodynamic limit, as evidenced by the repeated calcining result, and kinetic limit, as demonstrated by the hydrothermal result.

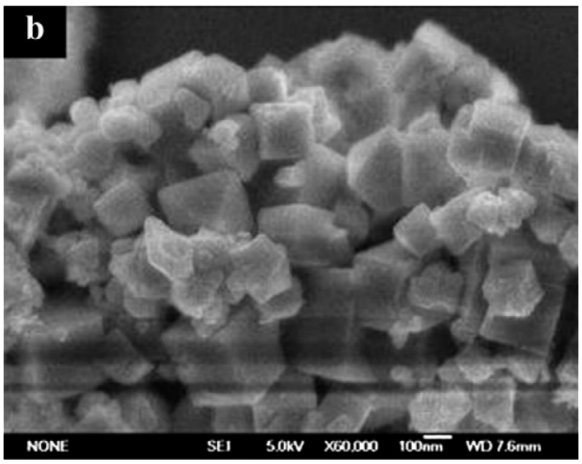

Figure 8.5. SEM image of La-doped $NaTaO_3$ synthesized by hydrothermal synthesis. Reproduced from reference [**26**].

Mixed A- and or B-site materials for the entire potassium sodium tantalate niobate material system have also been studied for their piezoelectric properties. [**27**, **146**, **147**]

Similar to the KTN particles, these materials tend to show inhomogeneous distributions of the A-site cation element correlated to the B-site cation, where the pairings of (K,Nb) and (Na,Ta) were observed through EDS (Figure 8.6). [**27**] The partial separation of niobium and tantalum were also studied in the precipitation of mixed alkali metal niobate ($Na_4K_4Nb_6 \cdot 9\ H_2O$) and tantalate ($Na_3K_5Ta_6O_{19} \cdot 10\ H_2O$) materials from mixed NaOH-KOH solutions. [**148**] The solubility of the potassium tantalate, potassium niobate, sodium tantalate, and sodium niobate were all compared by testing different NaOH:KOH ratios in the solution. Although the perovskites were not tested in this study, the solution behavior corresponding to the different cations can provide further insight into how they may act in a hydrothermal system.

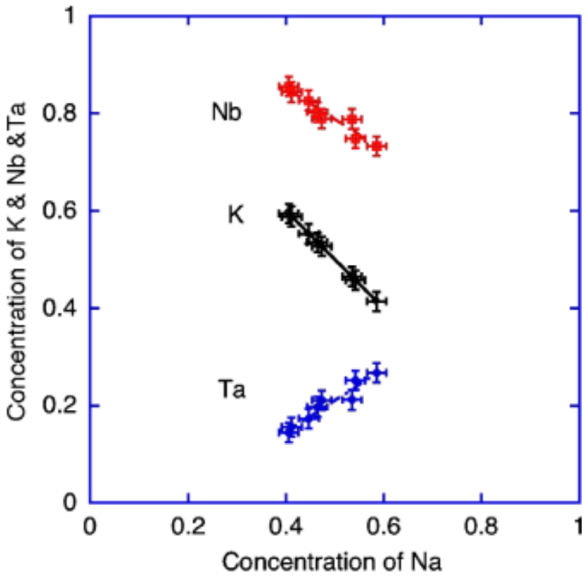

Figure 8.6. Concentrations of K (black), Nb (red), and Ta (blue) calculated from EDS spectra sampled from different parts of a Li- and Ta- modified (K, Na)NbO_3 sample showing positive or negative correlation with the Na concentration. Reproduced from [**27**].

References

[1] T. Ly, J. Wen, and L. D. Marks. Kinetic Growth Regimes of Hydrothermally Synthesized Potassium Tantalate Nanoparticles. *Nano Lett.*, 18(8):5186–5191, 2018.

[2] T. Ly, J. Wen, and L. D. Marks. Chemisorption-Driven Roughening of Hydrothermally Grown $KTa_{1-x}Nb_xO_3$ Nanoparticles. *J. Phys. Chem. C*, 124(14):7988–7993, 2020.

[3] T. Ly, J. Wen, and L. D. Marks. Complex Fluorine Chemical Potential Effects on the Shape and Compositional Heterogeneity of $KTa_{1-x}Nb_xO_3$ Nanoparticles. *J. Phys. Chem. C*, 124(47):26012–26017, 2020.

[4] D. B. Williams and C. B. Carter. *Transmission Electron Microscopy*. Springer, New York, 2009.

[5] R. J. Paull, T. Ly, Z. R. Mansley, K. R. Poeppelmeier, and L. D. Marks. Controlled Two-Step Formation of Faceted Perovskite Rare-Earth Scandate Nanoparticles. *Crystals*, 9(4):218, 2019.

[6] J. M. Yeomans. *Statistical Mechanics of Phase Transitions*. Oxford University Press Inc., New York, 1992.

[7] J. M. Corkhill and J. F. Goodman. The Interaction of Non-Ionic Surface-Active Agents with Water. *Adv. Colloid Interface Sci.*, 2:297–330, 1969.

[8] R. S. Berry and B. M. Smirnov. Phase Transitions in Various Kinds of Clusters. *Phys.-Usp.*, 52(2):137–164, 2009.

[9] C. Chen, Y. Wei, X. Jiao, and D. Chen. Hydrothermal Synthesis of $BaTiO_3$: Crystal Phase and the Ba^{2+} Ions Leaching Behavior in Aqueous Medium. *Mater. Chem. Phys.*, 110(1):186–191, 2008.

[10] B.-R. Chen, W. Sun, D. A. Kitchaev, J. S. Mangum, V. Thampy, L. M. Garten, D. S. Ginley, B. P. Gorman, K. H. Stone, G. Ceder, M. F. Toney, and L. T. Schelhas. Understanding Crystallization Pathways Leading to Manganese Oxide Polymorph Formation. *Nat. Commun.*, 9(1):2553, 2018.

[11] H. Lüth. *Surfaces and Interfaces of Solids*. Springer-Verlag Berlin Heidelberg, New York, 1993.

[12] U. Diebold, N. Ruzycki, G. S. Herman, and A. Selloni. One Step Towards Bridging the Materials Gap: Surface Studies of TiO_2 Anatase. *Catal. Today*, 85:93–100, 2003.

[13] L. Crosby, J. Enterkin, F. Rabuffetti, K. R. Poeppelmeier, and L. D. Marks. Wulff Shape of Strontium Titanate Nanocuboids. *Surf. Sci.*, 632:L22–L25, 2015.

[14] Y. Xia, Y. Xiong, B. Lim, and S. E. Skrabalak. Shape-Controlled Synthesis of Metal Nanocrystals: Simple Chemistry Meets Complex Physics? *Angew. Chem. Int. Ed.*, 48(1):60–103, 2009.

[15] G. Liu, C. Sun, H. G. Yang, S. C. Smith, L. Wang, G. Q. Lu, and H. M. Cheng. Nanosized Anatase TiO_2 Single Crystals for Enhanced Photocatalytic Activity. *Chem. Commun.*, 46(5):755–757, 2010.

[16] B. Lv, Z. Liu, H. Tian, Y. Xu, D. Wu, and Y. Sun. Single-Crystalline Dodecahedral and Octodecahedral α-Fe_2O_3 Particles Synthesized by a Fluoride Anion-Assisted Hydrothermal Method. *Adv. Funct. Mater.*, 20(22):3987–3996, 2010.

[17] A. Rečnik, I. Nyirő-Kósa, I. Dódony, and M. Pósfai. Growth Defects and Epitaxy in Fe_3O_4 and γ-Fe_2O_3 Nanocrystals. *CrystEngComm*, 15(37):7539–7547, 2013.

[18] C. Hou, W. Feng, L. Yuan, K. Huang, and S. Feng. Crystal Facet Control of $LaFeO_3$, $LaCrO_3$, and $La_{0.75}Sr_{0.25}MnO_3$. *CrystEngComm*, 16(14):2874–2877, 2014.

[19] S. Wang, X. Wu, L. Yuan, C. Zhang, and D. Lu. Shape Tuneable Synthesis of Perovskite Structured Rare-Earth Chromites $RECrO_3$ via a Mild Hydrothermal Method. *CrystEngComm*, 19(43):6436–6442, 2017.

[20] Y. Wang, G. Xu, L. Yang, Z. Ren, X. Wei, W. Weng, P. Du, G. Shen, and G. Han. Formation of Single-Crystal $SrTiO_3$ Dendritic Nanostructures via a Simple Hydrothermal Method. *J. Cryst. Growth*, 311(8):2519–2523, 2009.

[21] Y. Wang, G. Xu, L. Yang, Z. Ren, X. Wei, W. Weng, P. Du, G. Shen, and G. Han. Hydrothermal Synthesis of Single-Crystal $BaTiO_3$ Dendrites. *Mater. Lett.*, 63(2):239–241, 2009.

[22] H. Song and W. Ma. Hydrothermal Synthesis of Submicron $NaNbO_3$ Powders. *Ceram. Int.*, 37(3):877–882, 2011.

[23] J. Liu, G. Chen, Z. Li, and Z. Zhang. Hydrothermal Synthesis and Photocatalytic Properties of $ATaO_3$ and $ANbO_3$ (A = Na and K). *Int. J. Hydrogen Energy*, 32(13):2269–2272, 2007.

[24] A. Kudo and H. Kato. Effect of Lanthanide-Doping into $NaTaO_3$ Photocatalysts for Efficient Water Splitting. *Chem. Phys. Lett.*, 331:373–377, 2000.

[25] C. C. Hu and H. Teng. Influence of Structural Features on the Photocatalytic Activity of $NaTaO_3$ Powders from Different Synthesis Methods. *Appl. Catal., A*, 331(1):44–50, 2007.

[26] X. Li and J. Zang. Hydrothermal Synthesis and Characterization of Lanthanum-Doped $NaTaO_3$ with High Photocatalytic Activity. *Catal. Commun.*, 12(14):1380–1383, 2011.

[27] Y. Wang, D. Damjanovic, N. Klein, E. Hollenstein, and N. Setter. Compositional Inhomogeneity in Li- and Ta-Modified (K, Na)NbO_3 Ceramics. *J. Am. Ceram. Soc.*, 90(11):3485–3489, 2007.

[28] A. T. Bell. The Impact of Nanoscience on Heterogeneous Catalysis. *Science*, 299(5613):1688–1691, 2003.

[29] C. Burda, X. Chen, R. Narayanan, and M. A. El-Sayed. Chemistry and Properties of Nanocrystals of Different Shapes. *Chem. Rev.*, 105(4):1025–1102, 2005.

[30] T. D. Nguyen. From Formation Mechanisms to Synthetic Methods Toward Shape-Controlled Oxide Nanoparticles. *Nanoscale*, 5(20):9455–9482, 2013.

[31] E. Grabowska. Selected Perovskite Oxides: Characterization, Preparation and Photocatalytic Properties–A Review. *Appl. Catal., B*, 186:97–126, 2016.

[32] R. I. Walton. Perovskite Oxides Prepared by Hydrothermal and Solvothermal Synthesis: A Review of Crystallisation, Chemistry, and Compositions. *Chem. - Eur. J.*, 26(42):9041–9069, 2020.

[33] G. Wulff. On the Question of Speed of Growth and Dissolution of Crystal Surfaces. *Z. Kristallogr. Mineral.*, 34(5/6):449–530, 1901.

[34] D. R. Modeshia and R. I. Walton. Solvothermal Synthesis of Perovskites and Pyrochlores: Crystallisation of Functional Oxides under Mild Conditions. *Chem. Soc. Rev.*, 39(11):4303–4325, 2010.

[35] A. Rabenau. The Role of Hydrothermal Synthesis in Preparative Chemistry. *Angew. Chem. Int. Ed.*, 24:1026–1040, 1985.

[36] W. Sun, D. A. Kitchaev, D. Kramer, and G. Ceder. Non-Equilibrium Crystallization Pathways of Manganese Oxides in Aqueous Solution. *Nat. Commun.*, 10(1):573, 2019.

[37] R. A. Laudise. Hydrothermal Synthesis of Crystals. *Chem. Eng. News.*, 65(39):30–43, 1987.

[38] G. K. L. Goh, S. M. Haile, C. G. Levi, and F. F. Lange. Hydrothermal Synthesis of Perovskite and Pyrochlore Powders of Potassium Tantalate. *J. Mater. Res.*, 17(12):3168–3176, 2002.

[39] G. K. L. Goh, F. F. Lange, S. M. Haile, and C. G. Levi. Hydrothermal Synthesis of $KNbO_3$ and $NaNbO_3$ Powders. *J. Mater. Res.*, 18(2):338–345, 2003.

[40] N. Kumada, T. Kyoda, Y. Yonesaki, T. Takei, and N. Kinomura. Preparation of $KNbO_3$ by Hydrothermal Reaction. *Mater. Res. Bull.*, 42(10):1856–1862, 2007.

[41] L. D. Marks and D. J. Smith. High Resolution Studies of Small Particles of Gold and Silver. *J. Cryst. Growth*, 54(3):425–432, 1981.

[42] L. D. Marks. Direct Imaging of Carbon-Covered and Clean Gold (110) Surfaces. *Phys. Rev. Lett.*, 51(11):1000–1002, 1983.

[43] L. D. Marks and D. J. Smith. Direct Surface Imaging in Small Metal Particles. *Nature*, 303:316–317, 1983.

[44] Y. Lin, J. Wen, L. Hu, R. M. Kennedy, P. C. Stair, K. R. Poeppelmeier, and L. D. Marks. Synthesis-Dependent Atomic Surface Structures of Oxide Nanoparticles. *Phys. Rev. Lett.*, 111(15):156101, 2013.

[45] L. A. Crosby, R. M. Kennedy, B. Chen, J. Wen, K. R. Poeppelmeier, M. J. Bedzyk, and L. D. Marks. Complex Surface Structure of (110) Terminated Strontium Titanate Nanododecahedra. *Nanoscale*, 8:16606–16611, 2016.

[46] J. M. Cowley and A. F. Moodie. The Scattering of Electrons by Atoms and Crystals. I. A New Theoretical Approach. *Acta Crystallogr.*, 10:609–619, 1957.

[47] *MacTempasX*. Total Resolution, Berkeley, version 2.4.49 edition, 2019.

[48] *MDI Jade*. Materials Data, California, version 5.1.0 edition, 2010.

[49] H. M. Rietveld. A Profile Refinement Method for Nuclear and Magnetic Structures. *J. Appl. Cryst.*, 2:65–71, 1969.

[50] P. Hohenberg and W. Kohn. Inhomogeneous Electron Gas. *Phys. Rev.Phys. Rev.*, 136:B864–B871, 1964.

[51] W. Kohn and L. J. Sham. Self-Consistent Equations Including Exchange and Correlation Effects. *Phys. Rev.*, 140(4A):A1133–A1138, 1965.

[52] J. P. Perdew, K. Burke, and M. Ernzerhof. Generalized Gradient Approximation Made Simple. *Phys. Rev. Lett.*, 77:3865, 1996.

[53] J. P. Perdew, K. Burke, and M. Ernzerhof. Generalized Gradient Approximation Made Simple. *Phys. Rev. Lett.*, 78:1396(E), 1997.

[54] J. P. Perdew, A. Ruzsinszky, G. I. Csonka, O. A. Vydrov, G. E. Scuseria, L. A. Constantin, X. Zhou, and K. Burke. Restoring the Density-Gradient Expansion for Exchange in Solids and Surfaces. *Phys. Rev. Lett.*, 100(13):136406, 2008.

[55] P. Blaha, K. Schwarz, G. K. H. Madsen, D. Kvasnicka, J. Luitz, R. Laskowski, F. Tran, and L. D. Marks. *WIEN2k: An Augmented Plane Wave+Local Orbitals*

Program for Calculating Crystal Properties. Vienna University of Technology, Austria, 2018.

[56] P. Blaha, K. Schwarz, F. Tran, R. Laskowski, G. K. H. Madsen, and L. D. Marks. WIEN2k: An APW+LO Program for Calculating the Properties of Solids . *J. Chem. Phys.*, 152:74101, 2020.

[57] Y. Nishihata, O. Kamishima, H. Maeda, T. Ishii, A. Sawada, and H. Terauchi. EXAFS Study on the Local Structure in Potassium Tantalate. *Phys. B.*, 208-209:311–312, 1995.

[58] Y. He and Y. Zhu. Solvothermal Synthesis of Sodium and Potassium Tantalate Perovskite Nanocubes. *Chem. Lett.*, 33(7):900–901, 2004.

[59] M. Makarova, P. Bykov, J. Drahokoupil, M. Cernansky, Z. Dlabacek, A. Dejneka, L. Jastrabik, and V. Trepakov. Solvothermal Synthesis of Nanocrystalline $KTaO_3$: Effect of Solvent Dielectric Constant. *Mater. Res. Bull.*, 47(7):1768–1773, 2012.

[60] D. Gömpel, M. N. Tahir, M. Panthöfer, E. Mugnaioli, R. Brandscheid, U. Kolb, and W. Tremel. Facile Hydrothermal Synthesis of Crystalline Ta_2O_5 Nanorods, $MTaO_3$ (M = H, Na, K, Rb) Nanoparticles, and Their Photocatalytic Behaviour. *J. Mater. Chem. A*, 2(21):8033–8040, 2014.

[61] Y. Hu, H. Gu, Z. Hu, W. Di, Y. Yuan, J. You, W. Cao, Y. Wang, and H. L. W. Chan. Controllable Hydrothermal Synthesis of $KTa_{1-x}Nb_xO_3$ Nanostructures with Various

Morphologies and Their Growth Mechanisms . *Cryst. Growth Des.*, 8(3):832–837, 2008.

[62] B. K. Yun, Y. S. Koo, J. H. Jung, M. Song, and S. Yoon. Possible Role of Hydroxyl Group on Local Structure and Phase Transition of $KNbO_3$ and $KTaO_3$ Nanocrystals. *Phys. B.*, 405(23):4866–4870, 2010.

[63] H. Hayashi and Y. Hakuta. Hydrothermal Epitaxy of $KTaO_3$ Thin Films under Supercritical Water Conditions. *J. Mater. Sci.*, 43(7):2342–2347, 2007.

[64] S. Glinšek, B. Malič, T. Rojac, C. Filipič, B. Budič, and M. Kosec. $KTaO_3$ Ceramics Prepared by the Mechanochemically Activated Solid-State Synthesis. *J. Am. Ceram. Soc.*, 94(5):1368–1373, 2011.

[65] H. Kato and A. Kudo. New Tantalate Photocatalysts for Water Decomposition into H_2 and O_2. *Chem. Phys. Lett.*, 295(5-6):487–492, 1998.

[66] M. A. O'Keefe and G. W. Bailey. *Proceedings of the 37th Annual Meeting of the Electron Microscopy Society of America, San Antonio, Texas, 1979.* Claitor's Publicating Division, Baton Rouge, 1979.

[67] W. A. Johnson and R. F. Mehl. Reaction Kinetics in Processes of Nucleation and Growth . *Trans. Am. Inst. Min., Metall. Pet. Eng.*, 135:416–442, 1939.

[68] M. Avrami. Kinetics of Phase Change. I General Theory. *J. Chem. Phys.*, 7(12):1103–1112, 1939.

[69] M. Avrami. Kinetics of Phase Change. II Transformation-Time Relations for Random Distribution of Nuclei. *J. Chem. Phys.*, 8(2):212–224, 1940.

[70] A. N. Kolmogorov. On the Statistical Theory of the Crystallization of Metals . *Bull. Acad. Sci URSS*, 3:355–359, 1937.

[71] I. P. Zibrov, V. P. Filonenko, M. Sundberg, and P.-E. Werner. Structures and Phase Transitions of B-Ta_2O_5 and Z-Ta_2O_5: Two High-Pressure Forms of Ta_2O_5. *Acta Crystallogr.*, B56(4):659–665, 2000.

[72] N C Stephenson and R S Roth. Structural Systematics in the Binary System Ta_2O_5-WO_3. V. The Structure of the Low-Temperature Form of Tantalum Oxide L-Ta_2O_5. *Acta Crystallogr.*, B27:1037–1044, 1971.

[73] O. Y. Gorbenko, S. V. Samoilenkov, I. E. Graboy, and A. R. Kaul. Epitaxial Stabilization of Oxides in Thin Films. *Chem. Mater.*, 14:4026–4043, 2002.

[74] A. Roy Chaudhuri, M. Arredondo, A. Hähnel, A. Morelli, M. Becker, M. Alexe, and I. Vrejoiu. Epitaxial Strain Stabilization of a Ferroelectric Phase in $PbZrO_3$ Thin Films. *Phys. Rev. B*, 84(5):54112, 2011.

[75] F. Izumi and H. Kodama. A New Modification of Tantalum(V) Oxide. *J. Less-Common Met.*, 63:305–307, 1979.

[76] Y.-N. Wu, L. Li, and H.-P. Cheng. First-Principles Studies of Ta_2O_5 Polymorphs. *Phys. Rev. B*, 83(14):144105, 2011.

[77] P. Koirala, A. Gulec, and L. D. Marks. Surface Heterogeneity in $KTaO_3$ (001). *Surf. Sci.*, 657:15–19, 2017.

[78] Y. B. Xu, Y. L. Tang, Y. Liu, X. L. Ma, and Y. L. Zhu. Atomically Resolved Precipitates/Matrix Interfaces in $KTaO_3$ Crystals. *Philos. Mag.*, 96(5):486–497, 2016.

[79] A. Pimpinelli and J. Villain. *Physics of Crystal Growth*. Cambridge University Press, Cambridge, 1998.

[80] G. K. Rollefson. Frequency Factors of some Biomolecular Reactions. *J. Phys. Chem.*, 56(8):976–979, 1952.

[81] D. J. Chadi. Stabilities of Single-Layer and Bilayer Steps on Si(001) Surfaces. *Phys. Rev. Lett.*, 59(15):1691–1694, 1987.

[82] U. T. Höchli, H. E. Weibel, and L. A. Boatner. Quantum Limit of Ferroelectric Phase Transitions in $KTa_{1-x}Nb_xO_3$. *Phys. Rev. Lett.*, 39(18):1158–1161, 1977.

[83] D. Rytz and H. J. Scheel. Crystal Growth of $KTa_{1-x}Nb_xO_3$ (0 ¡ x ¡ 0.04) Solid Solutions by a Slow-Cooling Method. *J. Cryst. Growth*, 59:468–484, 1982.

[84] J. Y. Wang, Q. C. Guan, J. Q. Wei, M. Wang, and Y. G. Liu. Growth and Characterization of Cubic $KTa_{1-x}Nb_xO_3$ Crystals. *J. Cryst. Growth*, 116:27–36, 1992.

[85] N. Wei, D.-M. Zhang, X.-Y. Han, F.-X. Yang, Z.-C. Zhong, and K.-Y. Zheng. Synthesis and Mechanism of Ferroelectric Potassium Tantalate Niobate Nanoparticles

by the Solvothermal and Hydrothermal Processes. *J. Am. Ceram. Soc.*, 90(5):1434–1437, 2007.

[86] Z. Keyu, Z. Duanming, Z. Zhicheng, Y. Fengxia, and X. Han. Synthesis and Optical Properties of Tetragonal $KTa_{0.6}Nb_{0.4}O_3$ Nanoparticles. *Appl. Surf. Sci.*, 256(5):1317–1321, 2009.

[87] J.-M. Jehng and I. E. Wachs. The Molecular Structures and Reactivity of Supported Niobidum Oxide Catalysts . *Catal. Today*, 8:37–55, 1990.

[88] M. Nyman, T. M. Alam, F. Bonhomme, M. A. Rodriguez, C. S. Frazer, and M. E Welk. Solid-State Structures and Solution Behavior of Alkali Salts of the $[Nb_6O_{19}]^{8-}$ Lindqvist Ion. *J. Cluster Sci.*, 17(2):197–219, 2006.

[89] V. Plies and R. Gruehn. Zum Thermischen Verhalten von R-Nb_2O_5 und Strukturverwandtem V_3MoO_{10} und $V_5W_3O_{20}$. *J. Less-Common Met.*, 42:77–88, 1975.

[90] W. Petter and F. Laves. Das Bauprinzip der Kristallstruktur von η-Nb_2O_5. *Naturwissenschaften*, 52(22):617, 1965.

[91] C. Valencia-Balvín, S. Pérez-Walton, G. M. Dalpian, and J. M. Osorio-Guillén. First-Principles Equation of State and Phase Stability of Niobium Pentoxide. *Comput. Mater. Sci.*, 81:133–140, 2014.

[92] C. Nico, T. Monteiro, and M. P. F. Graça. Niobium Oxides and Niobates Physical Properties: Review and Prospects. *Prog. Mater. Sci.*, 80:1–37, 2016.

[93] T. K Andersen, D. D. Fong, and L. D. Marks. Pauling's Rules for Oxide Surfaces. *Surf. Sci. Rep.*, 73(5):213–232, 2018.

[94] E. Ringe, R. P. Van Duyne, and L. D. Marks. Kinetic and Thermodynamic Modified Wulff Constructions for Twinned Nanoparticles. *J. Phys. Chem. C*, 117(31):15859–15870, 2013.

[95] A. I. Kirkland, D. A. Jefferson, D. G. Duff, P. P. Edwards, I. Gameson, B. F. G. Johnson, and D. J. Smith. Structural Studies of Trigonal Lamellar Particles of Gold and Silver. *Proc. R. Soc. London, Ser. A*, 440:589–609, 1993.

[96] V. Germain, J. Li, D. Ingert, Z. L. Wang, and M. P. Pileni. Stacking Faults in Formation of Silver Nanodisks. *J. Phys. Chem. B*, 107(34):8717–8720, 2003.

[97] Y. Xiong, A. R. Siekkinen, J. Wang, Y. Yin, M. J. Kim, and Y. Xia. Synthesis of Silver Nanoplates at High Yields by Slowing Down the Polyol Reduction of Silver Nitrate with Polyacrylamide. *J. Mater. Chem.*, 17(25):2600–2602, 2007.

[98] J. Zhang, M. R. Langille, and C. A. Mirkin. Photomediated Synthesis of Silver Triangular Bipyramids and Prisms: The Effect of pH and BSPP. *J. Am. Chem. Soc.*, 132:12502–12510, 2010.

[99] A. Magrez, E. Vasco, J. W. Seo, C. Dieker, N. Setter, and L. Forró. Growth of Single-Crystalline $KNbO_3$ Nanostructures. *J. Phys. Chem. B*, 110:58–61, 2006.

[100] A. Simon and J. Ravez. The Oxyfluoride Ferroelectrics. *Ferroelectrics*, 24(1):305–307, 2011.

[101] H. Kageyama, K. Hayashi, K. Maeda, J. P. Attfield, Z. Hiroi, J. M. Rondinelli, and K. R. Poeppelmeier. Expanding Frontiers in Materials Chemistry and Physics with Multiple Anions. *Nat. Commun.*, 9(1):772, 2018.

[102] J. K. Harada, N. Charles, K. R. Poeppelmeier, and J. M. Rondinelli. Heteroanionic Materials by Design: Progress Toward Targeted Properties. *Adv. Mater.*, 31(19):1805295, 2019.

[103] L.-F. Huang, N. Z. Koocher, M. Gu, and J. M. Rondinelli. Structure Dependent Phase Stability and Thermal Expansion of Ruddlesden–Popper Strontium Titanates. *Chem. Mater.*, 30(20):7100–7110, 2018.

[104] K. R. Udayakumar and A. N. Cormack. Structural Aspects of Phase Equilibria in the Strontium-Titanium-Oxygen System. *J. Am. Ceram. Soc.*, 71(11):C469–C471, 1988.

[105] M. A. McCoy, R. W. Grimes, and W. E. Lee. Phase Stability and Interfacial Structures in the SrO–$SrTiO_3$ System. *Philos. Mag. A*, 75(3):833–846, 1997.

[106] T. Suzuki and M. Fujimoto. First-Principles Structural Stability Study of Nonstoichiometry-Related Planar Defects in $SrTiO_3$ and $BaTiO_3$. *J. Appl. Phys.*, 89(10):5622–5629, 2001.

[107] A. L. Benavides, M. A. Portillo, J. L. F. Abascal, and C. Vega. Estimating the Solubility of 1:1 Electrolyte Aqueous Solutions: the Chemical Potential Difference Rule. *Mol. Phys.*, 115(9-12):1301–1308, 2017.

[108] G. Akerlof and P. Bender. The Density of Aqueous Solutions of Potassium Hydroxide. *J. Am. Chem. Soc.*, 63(4):1085–1088, 1941.

[109] M. El Guendouzi and J. Faridi. Thermodynamic Properties and Solubility of Potassium Fluoride in Aqueous Solutions at Various Temperatures. *J. Fluorine Chem.*, 235:109558, 2020.

[110] T. M. Anderson, M. A. Rodriguez, F. Bonhomme, J. N. Bixler, T. M. Alam, and M. Nyman. An Aqueous Route to $[Ta_6O_{19}]^{8-}$ and Solid-State Studies of isostructural Niobium and Tantalum Oxide Complexes. *Dalton Trans.*, (40):4517–4522, 2007.

[111] G. J.-P Deblonde, A. Chagnes, S. Bélair, and G. Cote. Solubility of Niobium(V) and Tantalum(V) under Mild Alkaline Conditions. *Hydrometallurgy*, 156:99–106, 2015.

[112] E. Balogh, T. M. Anderson, J. R. Rustad, M. Nyman, and W. H. Casey. Rates of Oxygen-Isotope Exchange between Sites in the $[H_xTa_6O_{19}]^{(8-x)-}$(aq) Lindqvist Ion and Aqueous Solutions: Comparisons to $[H_xNb_6O_{19}]^{(8-x)-}$(aq). *Inorg. Chem.*, 46:7032–7039, 2007.

[113] L. B. Fullmer, P. I. Molina, M. R. Antonio, and M. Nyman. Contrasting Ion-Association Behaviour of Ta and Nb Polyoxometalates. *Dalton Trans.*, 43(41):15295–15299, 2014.

[114] E. G. Il'in, A. N. Zozulin, and Y. A. Buslaev. ^{17}O NMR Estimation of Oxygen–Central Ion Bonding in the Products of Hydrolysis of Niobium, Tantalum,

Arsenic, and Antimony Pentafluorides and the Symbatic Behavior of ^{17}O and ^{19}F NMR Chemical Shifts. *Dokl. Phys. Chem.*, 384(1-3):109–112, 2002.

[115] L. D. Marks and L. Peng. Nanoparticle Shape, Thermodynamics and Kinetics. *J. Phys.: Condens. Matter*, 28(5):53001, 2016.

[116] C. Zhao, T. Witters, B. Brijs, H. Bender, O. Richard, M. Caymax, T. Heeg, J. Schubert, V. V. Afanas'ev, A. Stesmans, and D. G. Schlom. Ternary Rare-Earth Metal Oxide High-k Layers on Silicon Oxide. *Appl. Phys. Lett.*, 86(13), 2005.

[117] H. M. Christen, G. E. Jellison, I. Ohkubo, S. Huang, M. E. Reeves, E. Cicerrella, J. L. Freeouf, Y. Jia, and D. G. Schlom. Dielectric and Optical Properties of Epitaxial Rare-Earth Scandate Films and Their Crystallization Behavior. *Appl. Phys. Lett.*, 88(262906):1–4, 2006.

[118] P. Koirala, C. A. Mizzi, and L. D. Marks. Direct Observation of Large Flexoelectric Bending at the Nanoscale in Lanthanide Scandates. *Nano Lett.*, 18(6):3850–3856, 2018.

[119] R. Uecker, B. Velickov, D. Klimm, R. Bertram, M. Bernhagen, M. Rabe, M. Albrecht, R. Fornari, and D. G. Schlom. Properties of Rare-Earth Scandate Single Crystals (Re = Nd–Dy). *J. Cryst. Growth*, 310(10):2649–2658, 2008.

[120] R. J. Paull, Z. R. Mansley, T. Ly, L. D. Marks, and K. R. Poeppelmeier. Synthesis of Gadolinium Scandate from a Hydroxide Hydrogel. *Inorg. Chem.*, 57(7):4104–4108, 2018.

[121] E. S. Stampler, W. C. Sheets, W. Prellier, T. J. Marks, and K. R. Poeppelmeier. Hydrothermal Synthesis of $LnMnO_3$ (Ln = Ho–Lu and Y): Exploiting Amphoterism in Late Rare-Earth Oxides. *J. Mater. Chem.*, 19(25):4375–4381, 2009.

[122] R. I. Walton. Subcritical Solvothermal Synthesis of Condensed Inorganic Materials. *Chem. Soc. Rev.*, 31(4):230–238, 2002.

[123] W. K. Burton, N. Cabrera, and F. C. Frank. The Growth of Crystals and the Equilibrium Structure of Their Surfaces. *Philos. Trans. R. Soc., A*, 243(866):299–358, 1951.

[124] F. C. Frank, R. H. Doremus, B. W. Roberts, and D. Tumbell. *In Growth and Perfection of Crystals*. Wiley, New York, 1958.

[125] W. F. Berg. Crystal Growth from Solutions. *Proc. R. Soc. London, Ser. A*, 164(916):79–95, 1938.

[126] L. L. Bircumshaw and A. C. Riddiford. Transport Control in Heterogenous Reactions. *Q. Rev., Chem. Soc.*, 6(2):157–185, 1952.

[127] M. M. Lencka and R. E. Riman. Thermodynamic Modeling of Hydrothermal Synthesis of Ceramic Powders. *Chem. Mater.*, 5:61–70, 1993.

[128] M. M. Lencka and R. E. Riman. Synthesis of Lead Titanate: Thermodynamic Modeling and Experimental Verification. *J. Am. Ceram. Soc.*, 76(10):2649–2659, 1993.

[129] M. M. Lencka and R. E. Riman. Thermodynamics of the Hydrothermal Synthesis of Calcium Titanate with Reference to Other Alkaline-Earth Titanates. *Chem. Mater.*, 7:18–25, 1995.

[130] G. Canu and V. Buscaglia. Hydrothermal Synthesis of Strontium Titanate: Thermodynamic Considerations, Morphology Control and Crystallisation Mechanisms. *CrystEngComm*, 19(28):3867–3891, 2017.

[131] B. L. Cushing, V. L. Kolesnichenko, and C. J. O'Connor. Recent Advances in the Liquid-Phase Syntheses of Inorganic Nanoparticles. *Chem. Rev.*, 104(9):3893–3946, 2004.

[132] I. Pastoriza-Santos and L. M. Liz-Marzan. Colloidal silver nanoplates. State of the art and future challenges. *J. Mater. Chem.*, 18(15):1724–1737, 2008.

[133] H. Li, X. Shen, Y. Liu, L. Wang, J. Lei, and J. Zhang. Facile Phase Control for Hydrothermal Synthesis of Anatase-Rutile TiO_2 with Enhanced Photocatalytic Activity. *J. Alloys Compd.*, 646:380–386, 2015.

[134] R. S. Berry. Clusters, Melting, Freezing, and Phase Transitions. *J. Chem. Soc. Faraday Trans.*, 86(13):2343–2349, 1990.

[135] D. J. Wales. Surveying a Complex Potential Energy Landscape: Overcoming Broken Ergodicity using Basin-Sampling. *Chem. Phys. Lett.*, 584:1–9, 2013.

[136] D. Schebarchov, F. Baletto, and D. J. Wales. Structure, Thermodynamics, and Rearrangement Mechanisms in Gold Clusters-Insights from the Energy Landscapes Framework. *Nanoscale*, 10(4):2004–2016, 2018.

[137] W. Sun and G. Ceder. Induction Time of a Polymorphic Transformation. *CrystEngComm*, 19(31):4576–4585, 2017.

[138] J. W. Gibbs. *The Collected Works of J. Willard Gibbs*, volume I. Longmans, Green and Co., New York City, 1928.

[139] J. W. Gibbs. *The Collected Works of J. Willard Gibbs*, volume II. Longmans, Green and Co., New York City, 1928.

[140] C. Herring. Some Theorems on the Free Energies of Crystal Surfaces. *Phys. Rev.*, 82(1):87–93, 1951.

[141] M. von Laue. Der Wulffsche Satz fur die Gleichgewichtsform von Kristallen. *Z. Kristallogr.*, 105:124–133, 1943.

[142] W. W. Mullins. Theory of Thermal Grooving. *J. Appl. Phys.*, 28(3):333–339, 1957.

[143] C. Herring. *The Physics of Powder Metallurgy*. McGraw-Hill, New York, 1951.

[144] D. Alpay, L. Peng, and L. D. Marks. Are Nanoparticle Corners Round? *J. Phys. Chem. C*, 119(36):21018–21023, 2015.

[145] H. Kato, K. Asakura, and A. Kudo. Highly Efficient Water Splitting into H_2 and O_2 over Lanthanum-Doped $NaTaO_3$ Photocatalysts with High Crystallinity and Surface Nanostructure. *J. Am. Chem. Soc.*, 125:3082–3089, 2003.

[146] S. Park, M. Peddigari, J. H. Kim, E. Kim, G. T. Hwang, J. W. Kim, C. W. Ahn, J. J. Choi, B. D. Hahn, J. H. Choi, W. H. Yoon, D. S. Park, K. I. Park, C. K. Jeong, J. W. Lee, and Y. Min. Selective Phase Control of Dopant-Free Potassium Sodium Niobate Perovskites in Solution. *Inorg. Chem.*, 59(5):3042–3052, 2020.

[147] P. Jana, V. A. De La Peña O'Shea, C. M. Montero, P. Gálvez, P. Pizarro, J. M. Coronado, and D. P. Serrano. Mixed $NaNb_xTa_{1-x}O_3$ Perovskites as Photocatalysts for H_2 production. *Green Chem.*, 17(3):1735–1743, 2015.

[148] J. H. Kennedy. Sodium-Potassium Niobates and Tantalates. *J. Inorg. Nucl. Chem.*, 20(1-2):53–57, 1961.